ADSORPTION AND REACTIVITY OF HALOGENATED HYDROCARBONS ON METAL AND SEMICONDUCTOR SURFACES.

Thesis submitted in accordance with the requirements of the University of Liverpool for the degree of Doctor of Philosophy

Author:
Chiara Panosetti

Primary Supervisor:
Prof. Werner A. Hofer

Secondary Supervisor:
Dr. George Darling

November 4, 2013

Abstract

We investigated the adsorption and reactivity of substituted hydrocarbons on Si and Cu surfaces using Grimme's vdW–corrected DFT, CI–NEB and STM simulations. Halogenated hydrocarbons on surfaces are systems of particular interest. These molecules adsorb and self–assembly at surfaces and many experimental works show that, if one provides energy to the complex, in the form of heat, light, or electrons dropped with an STM tip, they easily react resulting in single, or patterns of, chemisorbed atoms at specific and controllable sites. For instance, 1–chloropentane forms asymmetric (A) and symmetric (S) pairs on Si(001)–2×1. The rate of thermal reaction of A is greater than S in chlorinating room-temperature silicon. The energy threshold for electron–induced reaction is also different. We have used DFT and NEB tools to explain the features of this system and we simulated STM images in agreement with the experiments. On the other hand, diiodobenzenes physisorbed on Cu(110) can act as molecular calipers. We have computationally modelled the adsorption of 1,3–diiodobenzene (m–DIB) on Cu(110) and simulated STM images for the four most stable configurations using the Tersoff–Hamann approach at different bias voltages. We find that all the adsorption orientations have comparable energy and we discuss the relative probabilities of experimental observation as well as the structural details. We have furthermore compared the electronic ground–state reactivity of 1,3– and 1,4–diiodobenzene in order to show that the different symmetry of the initial adsorbed state greatly affects reactivity. Since the studied systems provide a means to surface functionalization via site–specific imprinting of single atoms, we also propose a model for Cu nanoclusters on Cu(110) supported by one or two chemisorbed S (or Cl) atoms.

Contents

All the molecules
every single one
the atoms
their spin
their charge
their charm
all and every one
in circles
in beauty.

E. N.

Chapter 1

Introduction and Outline

The present Thesis fits within the more general framework of Single Molecule Chemistry, with particular attention to one of its most striking aspects, that is, the possibility of finely–tuned surface patterning by means of the manipulation of moieties at the very atomic level. We investigated the adsorption and reactivity of halogenated hydrocarbons on silicon and copper surfaces using Grimme's vdW–corrected DFT, CI–NEB and STM simulations. Halogenated hydrocarbons on surfaces are systems of particular interest. These molecules adsorb and self–assembly at surfaces and many experimental works show that, if one provides energy to the complex, in the form of heat, light, or electrons dropped with an STM tip, they easily react resulting in single, or patterns of, chemisorbed halogen atoms at specific and controllable sites.

Part I of the present Thesis will illustrate the background in which our work unwinds, presenting an overview of the state of the art of Single Molecule Chemistry (Chapter 2), as well as a description of the most commonly used experimental techniques, focusing in particular on Scanning Tunneling Microscopy (Chapter 3).

In Part II, a thorough treatment of the essential theoretical toolbox used throughout our work will be given. Chapter 4 will present the fundamentals of Density Functional Theory, which is the core of all the calculations we performed. Chapter 5 will give highlights on the theory of STM simulations, focusing in particular on the Tersoff–Hamann approach. Despite the development of a number of more sophisticated models throughout the decades, such elegant approach is still the workhorse in STM simulations, as it provides qualitatively correct results in a large number of cases and under a broad range of conditions, yet being fairly easy to implement as it does not require a description of the electronic structure of the tip. In Chapter 6, an overview of the wide range of available methods for the search of saddle points in reactive processes will be given, as well as a detailed treatment of the method of our choice, that is, the Nudged Elastic Band. The latter has the advantage of not demanding prior knowledge of the transition state, but only of the initial and final states, as well as the ability, in its Climbing Image variant, to converge exactly to the Minimum Energy Path (MEP)

for a given potential.

In Part III, results will be presented. In Chapter 7 we will describe how 1–chloropentane forms asymmetric (A) and symmetric (S) pairs on Si(001)–2×1. Experimentally, Prof. J. Polanyi's group at University of Toronto found that the rate of thermal reaction of A is greater than S in chlorinating room–temperature silicon. The energy threshold for electron–induced reaction is also different. We have used DFT and NEB tools to explain the features of this system and we simulated STM images in agreement with the experiments.

On the other hand, diiodobenzenes physisorbed on Cu(110) have been shown, in works by Prof. J. Polanyi's group, to be able to undergo Localized Atomic Reactions (LARs) on smooth metal surfaces as nicely as the well established halogenated hydrocarbons on semiconductor surfaces. We have computationally modelled the adsorption of 1,3–diiodobenzene on Cu(110) and simulated STM images for the four most stable configurations using the Tersoff–Hamann approach at different bias voltages. We find that all the adsorption orientations have comparable energy and we discuss the relative probabilities of experimental observation as well as the structural details (Chapter 8). Furthermore, we have compared the electronic ground–state reaction paths of the first C–I bond cleavage for 1,3– and 1,4–diiodobenzene on Cu(110) (Chapter 9). The motivation for this comparison is that, while 1,4–diiodobenzene, which has been observed to act as a molecular caliper, physisorbs on Cu(110) in a symmetric configuration, its 1,3– isomer was found by our simulations to physisorb preferentially in an asymmetric arrangement, which we will show to greatly affect its reactivity.

Finally, since the studied systems provide a means to surface functionalization via site–specific imprinting of single atoms, we also propose a model for three–dimensional Cu nanostructures on Cu(110) supported by one or two chemisorbed S (or Cl) atoms. Results will be discussed in Chapter 10.

Part I

Background

Chapter 2

Single Molecule Chemistry

2.1 Introduction to Single Molecule Chemistry

Single molecule chemistry is the investigation of individual atoms and molecules as opposed to an ensemble.

In the gas phase, single molecule observations are achievable only at ultralow pressures or confining the object in some way (for example, ions in an electromagnetic trap). Some experiments were carried out in the 80's [1], but since the pionieering works of W. E. Moerner *et al.* [2] and M. Orritt *et al.* [3], who observed the spectra of single pentacene molecules in a p–terpenyl host crystal in the first condensed matter single molecule experiments, a whole new type of spectroscopy has emerged. In the following 20 years a large number of experimental and imaging techniques of growing sensibility and sophistication were applied to the investigation of single molecules confined in the bulk of a low–temperature condensed phase and, more recently, in room–temperature liquid phase or adsorbed on a surface.

In ordinary bulk experiments, a particular observable of the system is measured as an average over a large number of objects, hence the individual characteristics of a single component are lost. Conversely, an individual observation obviously carries different information than an averaged one, and single molecule experiments show, for example, that each molecule in an ensemble has its own distinct spectrum which is time–dependent. Similarly, the behaviour of a molecule is strongly affected by its local environment, even in counterintuitive ways, to the point that it can exhibit fluctuations as a result to changes in the surroundings (spectral diffusion; see for example Ref. [4]).

The most common techniques for condensed–matter single molecule spectroscopy, thoroughly reviewed in Refs. [5–9], are frequency–modulated absorption and laser–induced fluorescence excitation, in solid as well as liquid state. It has to be noted that, while bulk–phase single molecule experiments are already interesting due to the possibility of observing the signature of individual molecules, a whole new range of possibilities stems when it comes to surface experiments, thanks to the fact that, if a molecule is bound to a surface, it can be accessed for direct manipulation. Optical tweezers are

often employed for the observation of molecular motors relevant to the understanding of biological systems and the fabrication of nanodevices. Finally, Scanning Probe Microscopy (SPM) has been widely used in recent years for both detection and manipulation of single atoms and molecules attached to a wide range of surfaces. The latter is the field of greatest interest for the purpose of the present thesis. Hence only a brief overview of the main experimental tools a scientist has at his disposal for SMC will be given here, while we shall later focus on one of the most widely used instrument in Surface Science, that is, the Scanning Tunneling Microscope (STM) (cfr. Chapter 3).

2.2 Experimental techniques in SMC

An extensive review of experimental methods employed in single molecule chemistry, which we will here briefly summarize, can be found in Ref. [10]. Imaging experiments fall roughly in two categories. Optical techniques such as fluorescence are fast but can achieve only limited spatial resolution. Scanning probe microscopies, which require more time due to the necessity of scanning the sample, allow much higher spatial resolution, down to the nanometer scale. Furthermore, some experimental tools, such as optical tweezers and the STM, allow for the manipulation of the sample at the atomic or molecular level.

2.2.1 Laser induced fluorescence

Thanks to the low background and the high signal–to–noise ratio, laser–induced fluorescence is most extensively used in condensed matter Single Molecule Spectroscopy. It is a very versatile tool as it can be operative at both low or room temperatures and for solid as well as liquid substrates [5]. A narrow band single–frequency laser illuminates the sample and is tuned over the excitation frequency range of the single molecule of interest, whose presence is detected by measuring the emitted fluorescence.

2.2.2 Optical Tweezers

Optical tweezers (or laser traps) [11, 12] consist in a highly focused laser beam capable of generating forces of the order of piconewtons in order to hold or manipulate microscopic dielectric objects. Optical tweezers have been widely used in the study of molecular motors (see, for example, [13]).

2.2.3 Scanning Probe Microscopy

Near–Field Microscopy

Near–Field Scanning Optical Microscopy (NSOM) [14] is a type of Scanning Probe Microscopy, where a scanning optical fiber probe is placed at distances from the surface smaller than the wavelength λ. This allows to break the optical diffraction limit,

yielding resolutions down to the order of 20 nm. The resolution is only limited by the size of the detector aperture, not by the wavelength of the illuminating source. This technique can be used for imaging as well as the investigation of dynamic properties.

AFM

The Atomic Force Microscope was developed by Binnig, Quate and Gerber in 1986 [15]. It consists of a cantilever with a probe tip at its end, typically made of silicon or silicon nitride and with a radius of curvature of a few nanometers. The tip is placed close to a sample. Intermolecular forces between tip and sample cause a deflection of the cantilever that follows Hooke's law. The deflection is then recorded while the tip scans in two dimensions, resulting in a topological map of the sample. An AFM can operate in contact mode (the force is kept constant using the deflection as a feedback signal; it is used when the forces are repulsive), non–contact mode (the cantilever is oscillated with a quasi–resonant frequency which is perturbed by the tip–sample interaction; the perturbations are used as the recorded signal), or dynamic/tapping mode (the cantilever comes in contact with the sample at every oscillation cycle, and subsequently a force is applied to detach the tip from the sample). As opposed to the STM, the AFM can be used to scan non–conducting surfaces.

STM

The Scanning Tunneling Microscope (STM) was developed by G. Binnig and H. Rohrer at IBM laboratories in 1982 [16] and its impact was immediately so great that its inventors were awarded the Nobel Prize in Physics in 1986.
A Scanning Tunneling Microscope has a lateral resolution of 0.2 Å and a vertical resolution of less than 0.1 pm [17], which allows to detect and manipulate individual atoms. It is commonly used in vacuum, but the sample can also be in air, water or other gaseous and liquid enviroment.
The Scanning Tunneling Microscope is based on the principle of quantum tunneling. A sharp metallic tip, ideally ending with a single atom, is brought close to a surface and a bias voltage is applied, generating a tunneling current which will depend on the distance between the sample and the tip. The tunneling current is detected while the tip scans across the surface in two dimensions, and the linescans are then combined to provide a topographic map of the sample. An extensive description of the instrument and the theory of tunneling microscopy and simulations will be given in Chapters 3 and 5 respectively.

2.3 On–surface SMC: Localized Atomic Reactions

2.3.1 Gas–phase vs surface: selected impact parameters

The characterization of reaction dynamics is rooted in the collision theory independently developed by M. Trautz in 1916 [18] and W. Lewis in 1918 [19], which qualitatively describes how, in order for a reaction to occur, the reactants must hit each other in some convenient geometry and with sufficient energy to allow the exchange of atoms. It was quantitatively developed in the past half century with the introduction of quantum scattering theory (see, for example, Ref. [20]).

Experimentally, the advent of molecular beams made it possible to directly observe collisions in the gas phase [21]. However, the main limitation of this approach resides in the fact that observations are averaged over all possible impact parameters. Intuitively, if one of the reactants is instead attached to a surface, the degrees of freedom of a reactive collision are significantly reduced, thus allowing to conduct, and in principle to observe, reactions with selected impact parameters.

Success in exploiting reactions with selected impact parameters was initially reported by J. Polanyi and coworkers by means of surface–aligned photochemistry [22–26].

In the past decade, it has become evident that the Scanning Tunneling Microscope can play a crucial role in the field and it has been widely used since. Even though it is at present impossible to follow a reactive event in real time with an STM, since its response time is orders of magnitude larger than the typical collision timescale (10^{-14}-10^{-13} s), it can indeed be used to picture the reactants and the products immediately before and immediately afterwards, respectively. Provided that the system is simple enough, some appropriate theoretical transition state method such as the Nudged Elastic Band can help resolve the processes occurring during reaction.

Furthermore, as mentioned before, the STM is not merely an imaging instrument but it can also be used to manipulate surfaces and adsorbates, either moving moieties around or inducing reactions. The tunneling current generated by the tip can be used, for example, to selectively excite a portion of the surface, that is, where a molecule is attached. Hence, a reaction on a surface can be triggered either thermally (in which case we are referring to a ground–state mechanism) or by means of electronic excitation (in which case we are referring to an excited–state mechanism), the latter being achieved either with light or directly with the STM tip.

2.3.2 Localized Atomic Reactions

Another striking aspect of reactions on surfaces is that in most cases, that is, when no subsequent on–surface diffusion occurs, the products of the reaction will be in close vicinity to where the reactant was. This makes it possible to obtain a predictable and reproducible pattern of chemically bound products and to analyse the reaction

products, e.g. single atoms, which are imprinted on the surface.
Furthermore, on–surface reactions are usually more efficient than the same reactions in the gas–phase as the bonding to the surface stabilizes the transition state.
Such reactions were achieved and described for the first time by J. Polanyi and coworkers with chlorobenzene adsorbed on Si(111)–7×7 [27] and defined Localized Atomic Reactions, from now on often referred to as LAR. An extensive review up to 2006 can be found in Ref. [28]. Here, we highlight only the most relevant reactions reported in the cited Review as well as some more recent, with particular emphasis on halogenated compounds.

Patterned reactions at semiconductor surfaces

In 1999 Lu *et al.* [27] reported localized electron–induced chlorination of Si(111)–7×7 by chlorobenzene at ∼40% coverage. A continuous line of chemically attached Cl atoms was formed applying a continuous sequence of 4 V pulses along the line. The halogen atoms are imprinted on sites adjacent to the electron impact. In the same work, intermittent pulses at 60 Å intervals were found to produce three chemisorbed Cl atoms per pulse, localized predominantly at three adjacent silicon atoms beneath the tip. Analogous behaviour was reported for the thermal reaction of 1,2– and 1,4–dibromobenzenes at Si(111)–7×7 by Dobrin *et al.* [29] in 2004.
Chlorinated benzene was also found to react in a similar manner on Si(001)–2×1. In 2003, experimental and theoretical studies [30, 31] showed that chlorobenzene and 1,2–dichlorobenzene undergo localized reaction such that the C–Cl bond cleavage is accompanied by the formation of an adjacent vertical benzene ring, where both fragments are attached to silicon atoms belonging to the same silicon dimer.
As reported by Hossain *et al.* in 2005 [32, 33], allyl mercaptan (CH_2CHCH_2SH) on hydrogen–passivated Si(001)–2×1 undergoes a radical chain reaction at 300 K leading to the growth of a covalently bonded molecular line across the dimer rows, consisting in connected allyl mercaptan and styrene lines.
In 2008, Harikumar *et al.* [34] reported that 1,5–dichloropentane on Si(001)–2×1 self–assembles at room temperature into lines growing perpendicularly to the silicon dimer rows. Line growth is directed by the displacement of surface charge caused by the dipole momentum of the adsorbate.
In 2009, the same group deposited 1–fluoropentane on Si(001)–2×1 and triggered reaction using heat or electrons. In both cases, physisorbed 1–fluoropentane pairs undergo cooperative reaction resulting in a pair of chemisorbed F atoms on the surface. DFT calculations carried out in our group proved the reaction to be sequential to the scale of femtoseconds, that is, the second C–F bond cleavage is almost barrierless, due to the formation of a dangling bond subsequent to the first C–F bond cleavage followed by C–Si attachment.

Patterned reactions at metal surfaces

As opposed to semiconductor surfaces, which present localized charge densities giving rise to largely corrugated potential energy surfaces, metal surfaces are commonly referred to as "smooth" due to their large degree of surface charge delocalization. Hence, metal surfaces are dominated by diffusion. However, patterning is possible at metal surfaces as well as at semiconductor surfaces, even at room temperature.

The dissociative adsorption of diatomic molecules was first studied in the 90's by Brune *et al.* [35, 36] who investigated the reaction of O_2 molecules on Al(111) at 300 K. Spontaneous dissociation occurred with attachment of both atoms to the surface. However, the separation of the resulting chemisorbed adatoms was observed to be much wider than the O–O bond of the parent molecule. This result was interpreted as part of the chemisorption energy being converted into translational energy across the surface. For O_2 molecules on Pt(111) at lower temperatures (150-160 K), Wintterlin *et al.* observed spontaneous dissociative adsorption with the resulting adatoms separated by two lattice constants [37]. Similar behaviour was reported at still lower temperatures (40-150 K) by Stipe *et al.* [38].

Further, atomic sulphur adlayers resulting from the abstractive adsorption of hydrogen sulphide or methanethiol [39–41] have been reported to lead to different reconstructions depending on the coverage.

Local surface patterning was also observed by Maksymovych *et al.* in the propagation of the conformation of single CH_3SSCH_3 molecules on Au(111) [42]. Following STM–induced reaction at < 5 K, the *trans* conformation of the parent molecule is retained as the CH_3S species are ejected away from each other.

Local chemical reaction of benzene on Cu(110) was reported by Komeda *et al.* [43]. The dissociation of one of the C–H bonds induces a bonding geometry change from flat–lying to upright configuration.

More recently, Leung *et al.* reported localized atomic reaction of p–diiodobenzene on Cu(110) [44]. The latter finding is particularly relevant to the purpose of the present Thesis and will be further discussed in Part III.

REFERENCES

[1] W. M. Itano, J. C. Bergquist, and D. J. Wineland. Laser spectroscopy of trapped atomic ions. *Science*, 237(4815):612–7, 1987.

[2] W. E. Moerner and L. Kador. Optical detection and spectroscopy of single molecules in a solid. *Physical Review Letters*, 62(21):2535–2538, 1989.

[3] M. Orrit and J. Bernard. Single pentacene molecules detected by fluorescence excitation in a p–terphenyl crystal. *Physical Review Letters*, 65(21):2716–2719, 1990.

[4] W. E. Moerner. A dozen years of single–molecule spectroscopy in physics, chemistry, and biophysics. *The Journal of Physical Chemistry B*, 106(5):910–927, 2002.

[5] S. Nie and R. N. Zare. Optical detection of single molecules. *Annual Review of Biophysics and Biomolecular Structure*, 26:567–96, 1997.

[6] T. Plakhotnik, E. A. Donley, and U. P. Wild. Single-molecule spectroscopy. *Annual Review of Physical Chemistry*, 48:181–212, 1997.

[7] X. S. Xie and J. K. Trautman. Optical studies of single molecules at room temperature. *Annual Review of Physical Chemistry*, 49(1):441–80, 1998.

[8] W. E. Moerner. Illuminating single molecules in condensed matter. *Science*, 283(5408):1670–1676, 1999.

[9] R. J. Silbey. Introduction to the special feature on single–molecule chemistry and biology. *Proceedings of the National Academy of Science*, 104(31):12595, 2007.

[10] W. Ho. Single–molecule chemistry. *The Journal of Chemical Physics*, 117(24):11033, 2002.

[11] A. Ashkin. Acceleration and trapping of particles by radiation pressure. *Physical Review Letters*, 24:156–159, 1970.

[12] A. Ashkin, J. M. Dziedzic, J. E. Bjorkholm, and S. Chu. Observation of a single–beam gradient force optical trap for dielectric particles. *Optics Letters*, 11:288–290, 1986.

[13] A. D. Mehta, M. Rief, J. A. Spudich, D. A. Smith, and R. M. Simmons. Single–molecule biomechanics with optical methods. *Science*, 283(5408):1689–1695, 1999.

[14] U. Durig, D. W. Pohl, and Rohner. F. Near–field optical–scanning microscopy. *Journal of Applied Physics*, 59(10):3318–3327, 1986.

[15] G. Binnig, C. F. Quate, and C. Gerber. Atomic Force Microscope. *Physical Review Letters*, 56:930–933, Mar 1986.

[16] G. Binnig. Tunneling through a controllable vacuum gap. *Applied Physics Letters*, 40(2):178, 1982.

[17] H. Gawronski, M. Mehlhorn, and K. Morgenstern. Imaging phonon excitation with atomic resolution. *Science*, 319(5865):930–933, 2008.

[18] M. Trautz. Das Gesetz der Reaktionsgeschwindigkeit und der Gleichgewichte in Gasen. Bestätigung der Additivität von C_v–3/2R. Neue Bestimmung der Integrationskonstanten und der Molekül durchmesser. *Zeitschrift fúr Anorganische und Allgemeine Chemie*, 96(1):1–28, 1916.

[19] W. C. Lewis. Studies in catalysis. Part IX. The calculation in absolute measure of velocity constants and equilibrium constants in gaseous systems. *Journal of Chemical Society, Transactions*, 113:471–492, 1918.

[20] W. H. Miller. Recent advances in quantum mechanical reactive scattering theory: Including comparison of recent experiments with rigorous calculations of state–to–state cross sections for the H/D + H_2 → H_2/HD + H reactions. *Annual Review of Physical Chemistry*, 41(1):245–281, 1990.

[21] Lee Y. T. Molecular beam studies of elementary chemical processes. *Science*, 236(4803):793–798, 1987.

[22] J. C. Polanyi and R. J. Williams. Dynamics of surface–aligned photochemistry (theory). I. Trajectory study of H$\searrow$+Br′(ad). *The Journal of Chemical Physics*, 88(5):3363–3371, 1988.

[23] I. Harrison, J. C. Polanyi, and P. A. Young. Photochemistry of adsorbed molecules. IV. Photodissociation, photoreaction, photoejection, and photodesorption of H_2S on LiF(001). *The Journal of Chemical Physics*, 89(3):1498–1523, 1988.

[24] V. J. Barclay, D. B. Jack, J. C. Polanyi, and Y. Zeiri. Dynamics of surface–aligned photochemistry (theory). II. Localized H–atom scattering in the HBr(ad)/LiF(001)+$h\nu$ system. *The Journal of Chemical Physics*, 97(12):9458–9467, 1992.

[25] J. C. Polany and H. Rieley. Photochemistry in the adsorbed state. In C. T. Rettner and N. R. Ashfold, editors, *Dynamics of gas–surface interactions*, Advances in gas–phase photochemistry and kinetics. Royal Society of Chemistry, 1991.

[26] J. C. Polanyi and Y Zeiri. Dynamics of adsorbate chemistry. In H. L. Dai and W. Ho, editors, *Laser spectroscopy and photochemistry on metal surfaces*. World Scientific, 1995.

[27] P. H. Lu, J. C. Polanyi, and D. Rogers. Electron–induced 'Localized Atomic Reaction' (LAR): Chlorobenzene adsorbed on Si(111)–7×7. *The Journal of Chemical Physics*, 111(22):9905, 1999.

[28] I. R. McNab and J. C. Polanyi. Patterned atomic reaction at surfaces. *Chemical Reviews*, 106(10):4321–54, 2006.

[29] S. Dobrin, K. R. Harikumar, and J. C. Polanyi. An STM study of the localized atomic reaction of 1,2– and 1,4–dibromobenzene at Si(111)–7×7. *Surface Science*, 561(1):11–24, 2004.

[30] F. Y. Naumkin, J. C. Polanyi, D. Rogers, W. A. Hofer, and A. Fisher. Electron–induced attachment of chlorinated benzenes to Si(100)–2×1. *Surface Science*, 547(3):324–334, 2003.

[31] F. Y. Naumkin, J. C. Polanyi, and D. Rogers. Reaction of chlorinated benzenes with Si(100)–2×1: a theoretical study. *Surface Science*, 547(3):335–348, 2003.

[32] M. Z. Hossain, H. S. Kato, and M. Kawai. Controlled fabrication of 1D molecular lines across the dimer rows on the Si(100)–(2×1)–H surface through the radical chain reaction. *Journal of the American Chemical Society*, 127(43):15030–1, 2005.

[33] M. Z. Hossain, H. S. Kato, and M. Kawai. Fabrication of interconnected 1D molecular lines along and across the dimer rows on the Si(100)–(2×1)–H surface through the radical chain reaction. *The Journal of Physical Chemistry B*, 109(49):23129–33, 2005.

[34] K. R. Harikumar, T. Lim, I. R. McNab, J. C. Polanyi, L. Zotti, S. Ayissi, and W. A. Hofer. Dipole–directed assembly of lines of 1,5–dichloropentane on silicon substrates by displacement of surface charge. *Nature Nanotechnology*, 3(4):222–8, 2008.

[35] H. Brune, J. Wintterlin, R. J. Behm, and G. Ertl. Surface migration of "hot" adatoms in the course of dissociative chemisorption of oxygen on Al(111). *Physical Review Letters*, 68(5):624–626, 1992.

[36] H. Brune, J. Wintterlin, J. Trost, G. Ertl, J. Wiechers, and R. J. Behm. Interaction of oxygen with Al(111) studied by scanning tunneling microscopy. *The Journal of Chemical Physics*, 99(3):2128, 1993.

[37] J. Wintterlin, R. Schuster, and G. Ertl. Existence of a "hot" atom mechanism for the dissociation of O_2 on Pt(111). *Physical Review Letters*, 77(1):123–126, 1996.

[38] B. C. Stipe, M. A. Rezaei, W. Ho, S. Gao, M. Persson, and B. I. Lundqvist. Single–molecule dissociation by tunneling electrons. *Physical Review Letters*, 78:4410–4413, 1997.

[39] A. F. Carley, P. R. Davies, R. V. Jones, K. R. Harikumar, G. U. Kulkarni, and M. W. Roberts. The structure of sulfur adlayers at Cu(110) surfaces: an STM and XPS study. *Surface Science*, 447(1-3):39–50, 2000.

[40] A. F. Carley, P. R. Davies, R. V. Jones, K. R. Harikumar, G. U. Kulkarni, and M. W. Roberts. Structural aspects of chemisorption at Cu(110) revealed at the atomic level. *Topics in Catalysis*, 12:299–306, 2000.

[41] A. F. Carley, P. R. Davies, R. V. Jones, K. R. Harikumar, and M. W. Roberts. An STM and XPS study of the chemisorption of methyl mercaptan at a Cu(110) surface. *Surface Science*, 490(1-2):L585–L591, 2001.

[42] P. Maksymovych and J. T. Yates. Propagation of conformation in the surface–aligned dissociation of single CH_3SSCH_3 molecules on Au(111). *Journal of the American Chemical Society*, 128(33):10642–10643, 2006.

[43] T. Komeda, Y. Kim, Y. Fujita, Y. Sainoo, and M. Kawai. Local chemical reaction of benzene on Cu(110) via STM–induced excitation. *The Journal of Chemical Physics*, 120(11):5347–52, 2004.

[44] L. Leung, T. B. Lim, J. C. Polanyi, and W. A. Hofer. Molecular calipers control atomic separation at a metal surface. *Nano Letters*, 11(10):4113–4117, 2011.

Chapter 3

Scanning Tunneling Microscopy

The Scanning Tunneling Microscope (STM), as anticipated in Chapter 2, is a powerful instrument for the imaging of surfaces at the molecular level. Furthermore, its ability to allow for the manipulation of single moieties at the nanoscale makes it such a remarkably versatile tool that its employment in Single Molecule Chemistry has become an essential routine. In the present Chapter, a description of its functioning will be given from the operational and experimental point of view. A detailed theoretical treatment will be given in Chapter 5.

3.1 The instrument

A schematic diagram of a Scanning Tunneling Microscope is shown in Figure 3.1. Essential components of a STM are a scanning tip, usually made of tungsten, gold or a platinum–iridium alloy, a piezoelectric tube for the control of the height of the tip, an x–y scanner, a control unit, a vibration isolation system, and a computer for data processing.

3.2 Operational principle

The functioning of a Scanning Tunneling Microscope is based on the phenomenon of electron tunneling. A conducting tip is placed close to the sample, consisting of either a clean surface or a surface with adsorbates, and a bias voltage is applied so that a tunneling current is generated in the vacuum gap between the tip and the sample. The tunneling current is a function of the position of the tip, the applied bias voltage and the local density of states of the sample. As the tip scans the surface in two dimensions, the current is monitored, recorded and elaborated in the form of an image, providing a topological map of the sample which is, in all respects, a microscopic picture of the surface charge density.
In an ideal picture, the tip is terminated with a single atom. This implies that the tunneling process is strongly localized and allows for a spatial resolution down to the

order of magnitude of Angstroms. The resolution of the image is inversely related to the radius of curvature of the scanning tip.

Tunneling is the ability of an object, possessing a pronounced quantum character (that is, a momentum of the order of magnitude comparable to the Planck constant), to pass through barriers which would be classically impenetrable. For the sake of clarity and in a one–dimensional model a barrier can be seen as an external potential $U(z)$, acting on the particle, so that over a finite range of the coordinate z, the external potential will be greater than the kinetic energy E of the particle. This condition implies that, within classical mechanics, the presence of the particle on the other side of the barrier is forbidden, but if the particle is quantic, there is a nonzero probability of observing it beyond the barrier.

Through a square potential barrier, the solution of the Scrödinger equation is an exponential decay of the wave function:

$$\psi_n(z) = \psi_n(0)e^{-\kappa z} \tag{3.1}$$

with, in atomic units:

$$\kappa = \sqrt{2(U - E)} \tag{3.2}$$

The tunneling current is proportional to the probability of finding an electron beyond the barrier, that is:

$$I(z) \propto P(z) \propto |\psi_n(0)|^2 e^{-2\kappa z} \ . \tag{3.3}$$

In the low–bias regime, $U - E \simeq \phi$, where the work function ϕ is the amount of energy required to bring an electron from the Fermi level E_F to the vacuum range, that is, only the electrons whose energy is close to the Fermi level undergo the transition to the vacuum range necessary to achieve tunneling,

Therefore, rearranging, the tunneling current becomes

$$I(z) \propto e^{-k\sqrt{2\phi}z} \ . \tag{3.4}$$

Equation 3.4 is a qualitative approximation that does not take into account the electronic structure of the leads of the junction. For tunneling to occur, there must be at least one unoccupied state of appropriate energy on the other side of the barrier. The greater the availability of empty states is, the greater the tunneling current will be. In other words, the tunneling current depends on the local density of states of the sample. While for the purpose of the present Chapter Equation 3.4 is adequate enough to exemplify the principle of operation of an STM, a detailed theoretical treatment which includes the local density of states will be given in Chapter 5.

3.2.1 Operational modes

A Scanning Tunneling Microscope can be operated in Constant Height Mode (CHM) or Constant Current Mode (CCM).
In CHM, the height of the tip is kept constant while the tip scans the sample in two dimensions. Hence, to keep the voltage and the height from changing, the current varies and the image is obtained as a current map. This mode only works for surfaces with small corrugation, as corrugations higher than a few Angstroms may cause the tip to crash. However, the advantage of this technique is to allow for considerably faster scans.
In CCM, the current is kept constant while a feedback mechanism controls the height of the tip. If a protrusion is encountered, the tunneling current increases and the control mechanism retracts the piezotube until the value of the current is restored. Similarly, if a hole is encountered, the current decreases and the control mechanism brings the tip closer to the sample. The vertical displacement of the tip is recorded resulting in a topological map of the sample as an isocurrent surface.

3.3 Historical remarks

The Scanning Tunneling Microscope (STM) was developed by G. Binnig and H. Rohrer at IBM laboratories in 1982 [1] and its impact was immediately so great that its inventors were awarded the Nobel Prize in Physics in 1986. Below are listed outstanding achievements made possible by its use.

- In 1983, Binnig *et al.* imaged the terraced structure of Au(110), showing ribbons of narrow (111) facets along the [1$\underline{1}$0] direction [2].
- In 1986, Bryant *et al.* obtained the first atomically resolved image of graphite [3].
- In 1990, D. M. Eigler and E. K. Schweizer at IBM laboratories employed an STM to arrange Xe atoms on a Ni(110) surface to spell out the name of the company [4], giving birth to the most popular example of STM–controlled nanowriting in history. The experiment was performed in ultrahigh vacuum at 4 K; the nickel surface was sprayed with Xe gas and then the STM tip was used to move adsorbed Xe atoms one by one across the surface until the IBM logo was formed.
- In 1990, Driscoll *et al.* obtained STM images of uncoated duplex DNA on a ghraphite substrate [5].
- In 1993, Schmid *et al.* obtained the first chemically resolved STM image with a clear distinction of chemical species in a Pt/Ni alloy [6]. The chemical discrimination was made possible by a difference in corrugation between Pt and Ni of 0.3 Å.

- In 1993, Crommie *et al.* first directly imaged resonant patterns of surface states using a low–temperature STM on Cu(111) [7] and later confined them in a corral made of iron adatoms, assembled individually positioning iron adatoms with the STM tip [8].

- In the late 90's, STM–induced single molecule reactions began to be achieved, as reviewed in Chapter 2.

- In 1998, Stipe *et al.* used tunneling electrons to induce reversible rotation of molecular oxygen on Pt(111) [9]. In 2001, the same group obtained vibrational spectra of acetylene adsorbed on Cu(110) by observing an increase in the tunneling conductance resulting from the excitation of the C–H stretch mode [10].

An image gallery of the relevant historical development of scientific capabilities and applications of the STM is illustrated in Figure 3.2.

3.4 Figures

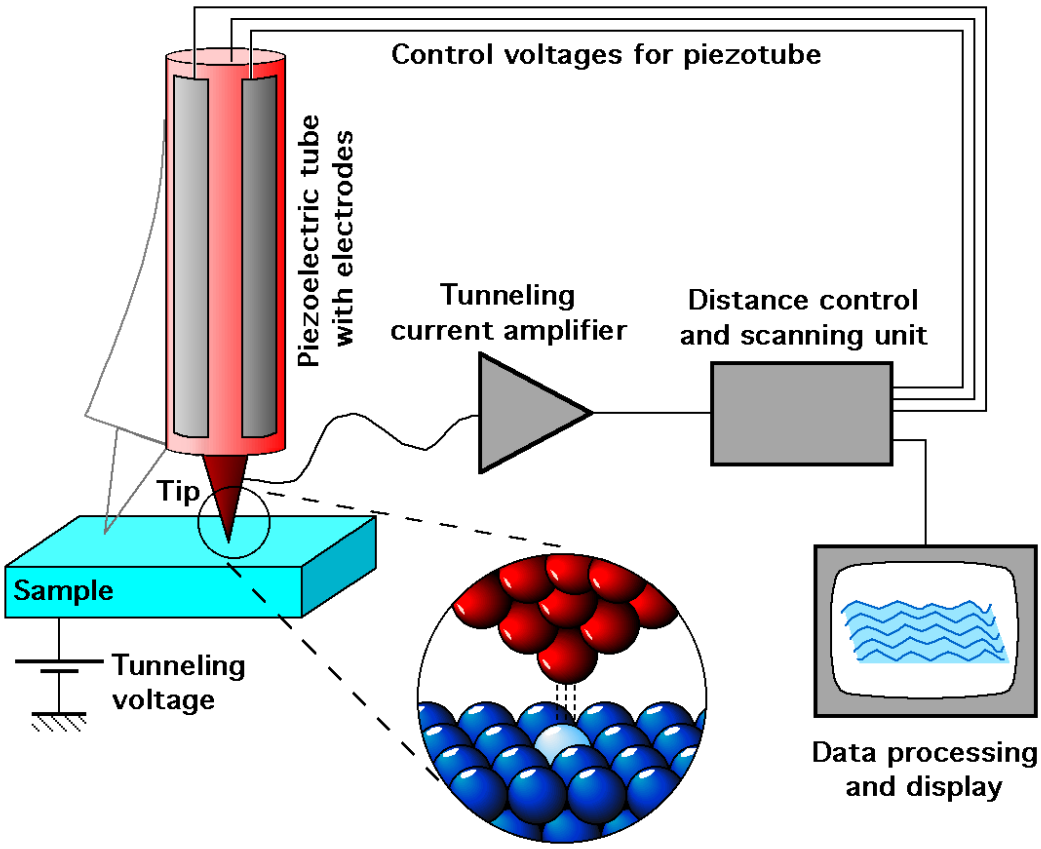

Figure 3.1: Schematic diagram of a Scanning Tunneling Microscopy experimental setup. Figure by Michael Schmid, TU Wien.

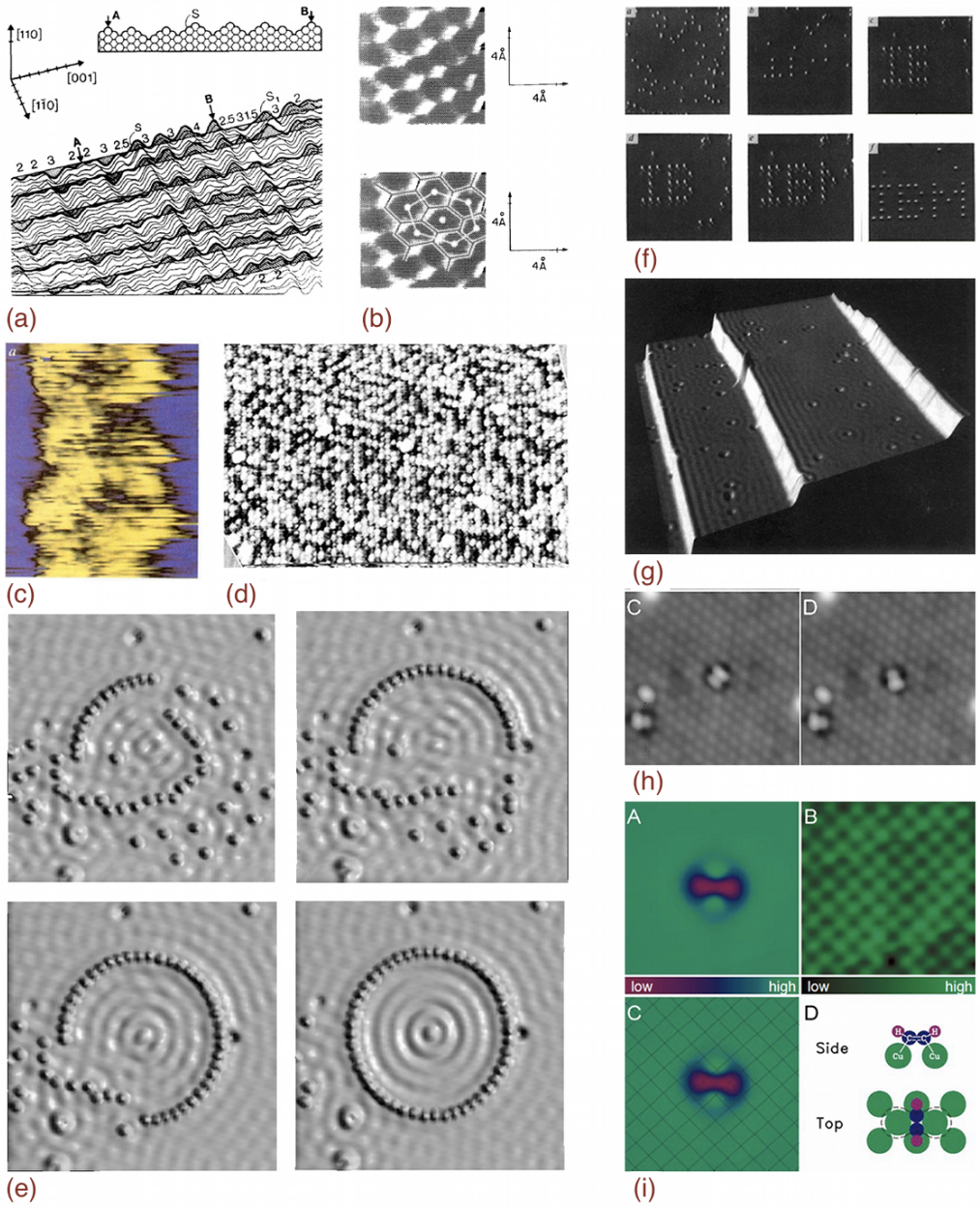

Figure 3.2: Selection of images illustrating the development of scientific capabilities and applications of the STM. (a) Terraced structure of Au(110) [2]. (b) STM image of graphite with highlighted atomic positions of carbon atoms [3]. (c) Sequence of STM images of Xe atoms on a Ni(110) surface illustrating the stages of forming the IBM logo. Adapted from [4]. (d) STM image of uncoated DNA duplex on a graphite substrate [5]. (e) STM image of a Pt/Ni alloy with distinguishable domains of different atomic species [6]. (f) Surface states of a Cu(111) surface [7]. (g) Sequence of STM images illustrating the stages of the formation of a Fe corral on Cu(110). In the last panel, the confinement of electron waves is clearly visible [8]. (h) STM–induced rotation of a single oxygen molecule on Pt(111) [9]. (i) Acetylene molecule on Cu(100). An increase of the tunneling current marks the stretching of the C–H bond (not shown) [10].

REFERENCES

[1] G. Binnig. Tunneling through a controllable vacuum gap. *Applied Physics Letters*, 40(2):178, 1982.

[2] G. Binnig, H. Rohrer, C.. Gerber, and E. Weibel. (111) facets as the origin of reconstructed Au(110) surfaces. *Surface Science Letters*, 131(1):L379–L384, 1983.

[3] A. Bryant, D. P. E. Smith, and C. F. Quate. Imaging in real time with the tunneling microscope. *Applied Physics Letters*, 48(13):832, 1986.

[4] D. M. Eigler and E. K. Schweizer. Positioning single atoms with a scanning tunnelling microscope. *Nature*, 344(6266):524–526, 1990.

[5] R. J. Driscoll, M. G. Youngquist, and J. D. Baldeschwieler. Atomic–scale imaging of DNA using scanning tunnelling microscopy. *Nature*, 346(6281):294–296, 1990.

[6] M. Schmid, H. Stadler, and P. Varga. Direct observation of surface chemical order by scanning tunneling microscopy. *Physical Review Letters*, 70(10):1441–1444, 1993.

[7] M. F. Crommie, C. P. Lutz, and D. M. Eigler. Imaging standing waves in a two–dimensional electron gas. *Nature*, 363(6429):524–527, 1993.

[8] M F Crommie, C P Lutz, and D M Eigler. Confinement of electrons to quantum corrals on a metal surface. *Science*, 262(5131):218–20, 1993.

[9] B. C. Stipe, M. A. Rezaei, and W. Ho. Inducing and viewing the rotational motion of a single molecule. *Science*, 279(5358):1907–1909, 1998.

[10] B. C. Stipe, M. A. Rezaei, and W. Ho. Single–molecule vibrational spectroscopy and microscopy. *Science*, 280(5370):1732–1735, 1998.

Part II

Theory

Chapter 4

Density Functional Theory

In solid state physics, and subsequently in surface science, one deals with a very large amount of particles. Orders of magnitude span from few to few hundred atoms, which means hundreds or thousands of electrons. It is evident that a quantum picture of the system in terms of many–body wave functions is extremely time consuming. Moreover, a simple argument carried out by van Vleck, and reported in Kohn's Nobel lecture [1], shows that such description is not only time consuming, but even physically meaningless. Precisely:

Definition 1 (van Vleck catastrophe)**.** For a system of N electrons, Ψ is not a legitimate scientific concept when $N > 10^3$.

Let us suppose we want to calculate the total energy of a many–body system of M atoms and N electrons. This requires the evaluation of its wave function with sufficient accuracy, that is, the overlap of the calculated wave function $\widetilde{\Psi}$ and the real wave function Ψ must be sufficiently close to unity. Let us adopt a fairly loose criterion, such as

$$|\langle\widetilde{\Psi}|\Psi\rangle|^2 \geqslant 0.5 \; . \tag{4.1}$$

Let us now assume that, for an atom of, for example, 10 electrons, this can be done with very high accuracy:

$$|\langle\widetilde{\psi}|\psi\rangle| \approx 1 - \epsilon \qquad \epsilon = 10^{-2} \; . \tag{4.2}$$

Then, for a system of $M = 10^2$ atoms, assuming 10 electrons per atom on average, that is, $N = 10^3$, the accuracy is still arguably acceptable, even though much looser:

$$|\langle\widetilde{\Psi}|\Psi\rangle| = (1-\epsilon)^M \approx e^{M\epsilon} = e^{-1} = 0.37 \quad \Rightarrow |\langle\widetilde{\Psi}|\Psi\rangle|^2 \approx 0.14 \; . \tag{4.3}$$

But if we increase the number of atoms to 10^4, it becomes evident that, even starting from reasonably accurate orbitals, it is not possible to obtain accurate many–body wave functions:

$$|\langle\widetilde{\Psi}|\Psi\rangle| = (1-\epsilon)^M \approx e^{M\epsilon} = e^{-10} \approx 5\times10^{-5} \quad \Rightarrow |\langle\widetilde{\Psi}|\Psi\rangle|^2 \approx 10^{-9}\ . \tag{4.4}$$

As if it was not enough, if we also wanted to store this wave function, things would get even worse. If we assume that every variable requires 3 bits, then we would need, for $N = 1000$, $3^{3000} = 10^{1431}$ bits. The total number of particles in the universe is of the order of 10^{80}, which means that storing that wave function would require more information than it is actually existing in the universe.

It is evident, from these considerations, that the very concept of wave function loses physical significance rapidly with increasing order of magnitude of the number of electrons. Therefore, a different approach is needed for many–body systems. One of the possible approaches is Density Functional Theory.

4.1 Schrödinger Equation

Within the Born–Oppenheimer approximation, the electrons move in an external potential V and an electronic state can be described as a wave function $\Psi(\mathbf{r}_1,\ldots,\mathbf{r}_N)$ which is a solution of the many–body Schrödinger equation

$$\hat{\mathcal{H}}\Psi = \left[\hat{\mathcal{T}}+\hat{\mathcal{V}}+\hat{\mathcal{U}}\right]\Psi = \left[\sum_i^N -\frac{\hbar^2}{2m}\nabla_i^2 + \sum_i^N V(\mathbf{r}_i) + \sum_{i<j} U(\mathbf{r}_i,\mathbf{r}_j)\right]\Psi = E\Psi \tag{4.5}$$

where $\hat{\mathcal{H}}$ is the electronic Hamiltonian operator, given by the sum of the operators $\hat{\mathcal{T}},\hat{\mathcal{V}},\hat{\mathcal{U}}$, that is, respectively, kinetic energy, external and internal potential. N is the number of electrons and U is an internal potential which accounts for the electron–electron interaction. Here, the complication with respect to a single–particle problem is represented by the interelectronic potential U. Equation 4.5 can be, in principle, solved by means of sophisticated yet computationally expensive post Hartree–Fock methods (see, for example, Ref. [2]), but in case of very large systems, as the ones of our interest, such methods are beyond the grasp of currently available computer power. Hence, Density Functional Theory is employed.

Since the Hamiltonian only contains mono– and bielectronic terms, the calculation of the expectation value of the total energy only requires one– and two–body density matrices and Equation 4.5 can be reformulated as follows:

$$\begin{aligned} E &= \langle\Psi|\hat{\mathcal{H}}|\Psi\rangle = \langle\Psi|\hat{\mathcal{T}}+\hat{\mathcal{V}}+\hat{\mathcal{U}}|\Psi\rangle = \\ &= -\frac{\hbar^2}{2m}\int d\mathbf{r}\,\nabla^2\rho(\mathbf{r}) + \int d\mathbf{r}\,v(\mathbf{r})\rho(\mathbf{r}) + \iint d\mathbf{r}_1 d\mathbf{r}_2\,\frac{\rho(\mathbf{r}_1,\mathbf{r}_2)}{r_{12}}\ . \end{aligned} \tag{4.6}$$

where

$$\rho(\mathbf{r}) = N \int d\sigma_1 \int d\mathbf{x}_2 ... \int d\mathbf{x}_N \, |\Psi(\mathbf{r}_1\sigma_1, \mathbf{x}_2 ... \mathbf{x}_N)|^2 \tag{4.7}$$

$$\rho(\mathbf{r}_1, \mathbf{r}_2) = N(N-1) \iint d\sigma_1 d\sigma_2 \int d\mathbf{x}_3 ... \int d\mathbf{x}_N \, |\Psi(\mathbf{r}_1\sigma_1, \mathbf{r}_2\sigma_2, \mathbf{x}_3 ... \mathbf{x}_N)|^2 \, . \tag{4.8}$$

The general idea of Density Functional Theory is that the energy can be expressed and calculated as a *functional* of the electron density, thus avoiding the computationally challenging task of the evaluation of the wave functions. Its general form will then be

$$E[\rho] = T[\rho] + U[\rho] + V[\rho] \, . \tag{4.9}$$

In Equation 4.5, as it is reasonable to assume, the operator $\hat{\mathcal{U}}$ can be approximated with its classical counterpart, that is the Coulombian self–interaction of a charge distribution:

$$\langle \Psi | \hat{\mathcal{U}} | \Psi \rangle = J[\rho] = \frac{1}{2} \iint d\mathbf{r}_1 d\mathbf{r}_2 \, \frac{\rho(\mathbf{r}_1)\rho(\mathbf{r}_2)}{r_{12}} \, . \tag{4.10}$$

This approximation presents two substantial limitations:

- it does not include the exchange interaction which arises from the antisymmetry of the wave function with respect to coordinate exchange for fermions; in other words, $\rho(\mathbf{r})$ does not distinguish between fermions and bosons;
- it also does not include particle self–interaction.

Hence, if we introduce a pair correlation function $h(\mathbf{r}_1, \mathbf{r}_2)$ that includes non–classical effects, we may rewrite the two–particle density function as

$$\rho(\mathbf{r}_1, \mathbf{r}_2) = \rho(\mathbf{r}_1)\rho(\mathbf{r}_2)[1 + h(\mathbf{r}_1, \mathbf{r}_2)] \tag{4.11}$$

and the expectation value of $\hat{\mathcal{U}}$ then becomes

$$\langle \Psi | \hat{\mathcal{U}} | \Psi \rangle = J[\rho] + \frac{1}{2} \iint d\mathbf{r}_1 d\mathbf{r}_2 \, \rho(\mathbf{r}_1)\rho(\mathbf{r}_2) \frac{h(\mathbf{r}_1, \mathbf{r}_2)}{r_{12}} = J[\rho] + \frac{1}{2} \int d\mathbf{r}_1 \rho(\mathbf{r}_1) v_{xc}(\mathbf{r}_1) \tag{4.12}$$

where

$$v_{xc}(\mathbf{r}_1) := \int d\mathbf{r}_2 \, \rho(\mathbf{r}_2) \frac{h(\mathbf{r}_1, \mathbf{r}_2)}{r_{12}} \tag{4.13}$$

is a local potential which accounts for correlation and exchange effects. The accuracy of DFT, therefore, is essentially determined by the accuracy of the description of v_{xc}.

4.2 Hohenberg–Kohn Theorems

It is straightforward to prove that the one–particle external potential $\hat{\mathcal{V}}$ operating on a system of N electrons, that is, the attractive potential between the nuclei, uniquely determines the ground state of a system. In fact, since $\hat{\mathcal{T}}$ and $\hat{\mathcal{V}}$ have the same form for every N–electron molecule, the specificity of the system is all contained in the external potential.

Let us consider the set $\mathcal{V}$ of all one–particle potentials. The solution of the Schrödinger equation defines a map M from $\mathcal{V}$ to a subset $\mathcal{G} \subset \mathcal{H}$ of the Hilbert space. This map is, by construction, surjective:

$$M \colon \mathcal{V} \twoheadrightarrow \mathcal{G} \; . \tag{4.14}$$

The calculation of the density from the wave function by integration of $N-1$ coordinates also defines a map D from the Hilbert space to the density space $\mathcal{N}$ which is also surjective by construction:

$$D \colon \mathcal{G} \twoheadrightarrow \mathcal{N} \; . \tag{4.15}$$

Hence, the composite map $D \circ M$ is also surjective:

$$D \circ M \colon \mathcal{V} \twoheadrightarrow \mathcal{N} \; . \tag{4.16}$$

Naively, one may conclude that there is a one–to–one correspondence between the space of potentials and the space of densities, but this is not a trivial conclusion. To be so, the map $D \circ M$ should also be injective. The first Hohenberg–Kohn Theorem proves, by *reductio ad absurdum*, the bijection between $\mathcal{V}$ and $\mathcal{N}$, while the second Hohenberg–Kohn Theorem assesses the variational nature of DFT [3].

Theorem I (First Hohenberg–Kohn Theorem)**.** *For a non degenerate ground state, the external potential $V = \langle \hat{\mathcal{V}} \rangle$, and hence the total energy, is a unique functional of the electron density $\rho(\mathbf{r})$.*

Proof. Let $\hat{\mathcal{V}}^{(1)}$ and $\hat{\mathcal{V}}^{(2)}$ be two different external potentials differing by more than a constant and generating the same electron density $\rho^{(1)}(\mathbf{r}) = \rho^{(2)}(\mathbf{r}) = \rho(\mathbf{r})$.
$\hat{\mathcal{V}}^{(1)}$ and $\hat{\mathcal{V}}^{(2)}$ belong to two distinct Hamiltonians $\hat{\mathcal{H}}^{(1)}$ and $\hat{\mathcal{H}}^{(2)}$ whose respective eigenstates are $|\Psi^{(1)}\rangle$ and $|\Psi^{(2)}\rangle$ with eigenvalues $E^{(1)}$ and $E^{(2)}$.
So, for the variational principle:

$$E^{(1)} < \langle \Psi^{(2)} | \hat{\mathcal{H}}^{(1)} | \Psi^{(2)} \rangle = \langle \Psi^{(2)} | \hat{\mathcal{H}}^{(2)} | \Psi^{(2)} \rangle + \langle \Psi^{(2)} | \hat{\mathcal{H}}^{(1)} - \hat{\mathcal{H}}^{(2)} | \Psi^{(2)} \rangle \tag{4.17}$$

$$E^{(1)} < E^{(2)} + \langle \Psi^{(2)} | \hat{\mathcal{V}}^{(1)} - \hat{\mathcal{V}}^{(2)} | \Psi^{(2)} \rangle = E^{(2)} + \int d\mathbf{r} \rho(\mathbf{r}) [v^{(1)}(\mathbf{r}) - v^{(2)}(\mathbf{r})] \; . \tag{4.18}$$

Likewise:

$$E^{(2)} < E^{(1)} + \langle \Psi^{(1)} | \hat{\mathcal{V}}^{(2)} - \hat{\mathcal{V}}^{(1)} | \Psi^{(1)} \rangle = E^{(1)} + \int d\mathbf{r} \rho(\mathbf{r}) [v^{(2)}(\mathbf{r}) - v^{(1)}(\mathbf{r})] \; . \tag{4.19}$$

Summing Equations 4.18 and 4.19 gives $E^{(1)} + E^{(2)} < E^{(1)} + E^{(2)}$ which is a contradiction. This results descends from the assumption that $|\Psi^{(1)}\rangle$ and $|\Psi^{(2)}\rangle$, although being different, generate the same electron density, that is $\rho^{(1)}(\mathbf{r}) = \rho^{(2)}(\mathbf{r}) = \rho(\mathbf{r})$. Hence the assumption is wrong and it must be:

$$\rho^{(1)}(\mathbf{r}) \neq \rho^{(2)}(\mathbf{r}) \; . \qquad \square$$

This means that $D \circ M \colon \mathcal{V} \leftrightarrow \mathcal{N}$, therefore the relation is invertible and the electron density uniquely determines the external potential and hence all the properties of the system. Then, for a generic operator $\hat{\mathcal{O}}$, there must exist some functional $O[\rho]$ such that

$$\langle \hat{\mathcal{O}} \rangle = \langle \Psi[\rho] | \hat{\mathcal{O}} | \Psi[\rho] \rangle = O[\rho] \tag{4.20}$$

where $O[\rho]$ is a universal functional which is independent of the nature of the system but will be observable–specific. The Schrödinger equation may then be rewritten as

$$E[\rho] = \langle \Psi | \hat{\mathcal{T}} + \hat{\mathcal{U}} + \hat{\mathcal{V}} | \Psi \rangle = \langle \Psi | \hat{\mathcal{T}} + \hat{\mathcal{U}} | \Psi \rangle + V[\rho] = \tag{4.21}$$

$$= F_{HK} + \int d\mathbf{r} \rho(\mathbf{r}) v(\mathbf{r}) \tag{4.22}$$

where F_{HK} is a functional whose form is unknown but whose existence is proven. In general, as shown in Equation 4.12, the latter can be expressed separating the classical terms, that is kinetic and coulombian, from the non–classical terms:

$$F_{HK}[\rho] = T[\rho] + U[\rho] = T[\rho] + J[\rho] + V_{xc}[\rho] \tag{4.23}$$

Theorem II (Second Hohenberg–Kohn Theorem)**.** *The density ρ that minimizes the total energy $E[\rho]$ is the exact ground state density.*

Proof. Given that, from the first Hohenberg–Kohn Theorem, $D \circ M \colon \mathcal{V} \leftrightarrow \mathcal{N}$, then let us consider a density $\rho^{(2)}$ such that $\rho^{(2)} \geqslant 0$ and $\int d\mathbf{r} \rho^{(2)} = N$.
Then, for the variational principle:

$$E^{(1)} = E[\rho^{(1)}] = \langle \Psi^{(1)} | \hat{\mathcal{H}}^{(1)} | \Psi^{(1)} \rangle \leqslant \langle \Psi^{(2)} | \hat{\mathcal{H}}^{(1)} | \Psi^{(2)} \rangle = E[\rho^{(2)}] = E^{(2)} \tag{4.24}$$

and the inequality is strict if $\rho^{(2)} \neq \rho^{(1)}$.
Therefore, since minimizing the functional $E[\rho]$ with respect to ρ leads to the energy of the ground state, the density ρ_0 which minimizes $E[\rho]$ is the ground state density. $\square$

4.2.1 Degenerate ground states

If the ground state is degenerate, the bijectivity between density and wave function breaks down, and so does the uniqueness of the ground state expectation value of operators. In particular, the correspondence between the density and the potential is no longer bijective. This means that the first Hohenberg–Kohn theorem can no longer be proven. A particular case is the functional F_{HK} which is the same for every degenerate state, and hence it can still be defined unique.

4.2.2 $N-$ and $V-$representability

Let us assume to approach a calculation using DFT. We choose an external potential and we assume to know $F_{HK}[\rho]$ with sufficient accuracy, that is, we have a good model for v_{xc}. We may start with an assumed initial density, physically acceptable, and operate small variations based on the variational nature of the problem. Since the wave function never appears in the process, it is legitimate to wonder whether the chosen density satisfies the Hohenberg–Kohn theorems. In other words, it is not clear that an arbitrary density, although physically acceptable, would necessarily be the ground state of a smooth external potential.

Definition 2. A density function is defined *$V-$representable* if it corresponds to the density of an $N-$particle antisymmetric ground state $|\Psi\rangle$ associated to an external potential $\hat{\mathcal{V}}$.

Example: Excited state density of single particles in finite systems. A singlet and a triplet generate the same density function even though they have different energies.
The issue arises from the fact that the Hohenberg–Kohn theorems prove that there is a bijective correspondence between the space of the densities and the space of the potentials, but this does not necessarily mean that the correspondence between the Hilbert space and the space of densities is revertible as well. In fact, if a generic composite mapping $g \circ f$ is bijective, it can only be concluded that f is injective and g is surjective. Hence, g (in our case, D) need not be injective. In other words, different wave functions can generate the same density.
Equation 4.22 is only defined for $V-$representable density functions. In order to overcome this limitation, a more general formulation was proposed independently by Levy and Lieb [4–7]. Their extended minimization algorithm requires the densities to be only $N-$representable.

Definition 3. A density function is defined *$N-$representable* if it corresponds to the density of an arbitrary $N-$particle antisymmetric ground state $|\Psi\rangle$.

This condition is much weaker than $V-$representability and it was proven to be easily satisfied by an arbitrary density [8].

4.2.3 Harriman's orbitals and the Lieb–Levy scheme

For a one–dimensional N–particle density $\rho(x)$, let us define the auxiliary function $f(x)$ as

$$f(x) = \frac{2\pi}{N} \int_{-\infty}^{x} dx' \rho(x') \tag{4.25}$$

and an orthogonal and complete set of single–particle orbitals

$$\phi_k(x) = \left(\frac{\rho(x)}{N}\right)^{\frac{1}{2}} \exp\left\{i[kf(x) + \phi(x)]\right\} \tag{4.26}$$

where k is an integer and $\phi(x)$ is an arbitrary phase factor. A Slater orbital $|\Psi\rangle$ may always be constructed from N such orbitals and, from the properties of the Hartree–Fock derivation, a density may be obtained from it as

$$\langle\Psi|\hat{\rho}|\Psi\rangle = \sum_{i=1}^{N} |\phi_k|^2 = \rho(x) \ . \tag{4.27}$$

A density thus defined is N–representable.
Given a Hamiltonian

$$\hat{\mathcal{H}} = \hat{\mathcal{T}} + \hat{\mathcal{V}} + \hat{\mathcal{U}} \tag{4.28}$$

we may now redefine the universal part of the energy functional as

$$Q[\rho] := \min_{\Psi^\rho \to \rho} \langle\Psi^\rho|\hat{\mathcal{T}} + \hat{\mathcal{U}}|\Psi^\rho\rangle = \langle\Psi^\rho_{\text{min}}|\hat{\mathcal{T}} + \hat{\mathcal{U}}|\Psi^\rho_{\text{min}}\rangle \tag{4.29}$$

where a constrained minimization is conducted over all the antisymmetric wave functions Ψ^ρ yielding the arbitrary trial N–representable density ρ. We define $|\Psi^\rho_{\text{min}}\rangle$ as the wave function that minimizes $\hat{\mathcal{T}} + \hat{\mathcal{U}}$ for a fixed N. In particular, for the ground state density ρ_0

$$Q[\rho_0] = \langle\Psi^{\rho_0}_{\text{min}}|\hat{\mathcal{T}} + \hat{\mathcal{U}}|\Psi^{\rho_0}_{\text{min}}\rangle \ . \tag{4.30}$$

Theorem III. *For an arbitrary N–representable density $\rho(\mathbf{r})$,*

$$\int d\mathbf{r} v(\mathbf{r})\rho(\mathbf{r}) + Q[\rho] \geqslant E_0 \tag{4.31}$$

where E_0 is the ground state energy.

Proof. We have defined $|\Psi^\rho_{\text{min}}\rangle$ as the wave function that minimizes $\hat{\mathcal{T}} + \hat{\mathcal{U}}$ for a fixed N. Then, using Equation 4.29:

$$\int d\mathbf{r} v(r)\rho(\mathbf{r}) + Q[\rho] = \int d\mathbf{r} v(\mathbf{r})\rho(\mathbf{r}) + \langle \Psi^{\rho}_{\min} | \hat{\mathcal{T}} + \hat{\mathcal{U}} | \Psi^{\rho}_{\min} \rangle = \tag{4.32}$$

$$= \langle \Psi^{\rho}_{\min} | \hat{\mathcal{T}} + \hat{\mathcal{V}} + \hat{\mathcal{U}} | \Psi^{\rho}_{\min} \rangle = \langle \Psi^{\rho}_{\min} | \hat{\mathcal{H}} | \Psi^{\rho}_{\min} \rangle \tag{4.33}$$

Since the density in the equation above is not generally the ground state density, we have, by the variational principle:

$$\langle \Psi^{\rho}_{\min} | \hat{\mathcal{T}} + \hat{\mathcal{V}} + \hat{\mathcal{U}} | \Psi^{\rho}_{\min} \rangle \geqslant E_0 \ . \tag{4.34}$$

The combination of Equations 4.33 and 4.34 completes the proof. □

Theorem IV. *For the ground state density,*

$$\int d\mathbf{r} v(\mathbf{r})\rho_0(\mathbf{r}) + Q[\rho_0] = E_0 \ . \tag{4.35}$$

Proof. The true ground state of the system $|\Psi_0\rangle$ is not necessarily equal to $|\Psi^{\rho_0}_{\min}\rangle$.It follows, by the variational principle, that

$$\langle \Psi^{\rho_0}_{\min} | \hat{\mathcal{T}} + \hat{\mathcal{V}} + \hat{\mathcal{U}} | \Psi^{\rho_0}_{\min} \rangle \geqslant \langle \Psi_0 | \hat{\mathcal{T}} + \hat{\mathcal{V}} + \hat{\mathcal{U}} | \Psi_0 \rangle \tag{4.36}$$

which can be rewritten as

$$\int d\mathbf{r} \rho_0(\mathbf{r}) v(\mathbf{r}) + \langle \Psi^{\rho_0}_{\min} | \hat{\mathcal{T}} + \hat{\mathcal{U}} | \Psi^{\rho_0}_{\min} \rangle \geqslant \int dr |\Psi_0|^2 v(\mathbf{r}) + \langle \Psi_0 | \hat{\mathcal{T}} + \hat{\mathcal{U}} | \Psi_0 \rangle \tag{4.37}$$

which, since the first terms of both sides are equal, reduces to

$$\langle \Psi^{\rho_0}_{\min} | \hat{\mathcal{T}} + \hat{\mathcal{U}} | \Psi^{\rho_0}_{\min} \rangle \geqslant \langle \Psi_0 | \hat{\mathcal{T}} + \hat{\mathcal{U}} | \Psi_0 \rangle \tag{4.38}$$

But, by definition of $|\Psi^{\rho_0}_{\min}\rangle$:

$$\langle \Psi_0 | \hat{\mathcal{T}} + \hat{\mathcal{U}} | \Psi_0 \rangle \geqslant \langle \Psi^{\rho_0}_{\min} | \hat{\mathcal{T}} + \hat{\mathcal{U}} | \Psi^{\rho_0}_{\min} \rangle \ . \tag{4.39}$$

The only way both Equations 4.38 and 4.39 can be satisfied is if the equality holds. Therefore

$$\langle \Psi_0 | \hat{\mathcal{T}} + \hat{\mathcal{U}} | \Psi_0 \rangle = Q[\rho_0] \ . \tag{4.40}$$

Using the definition of the ground state energy with the true ground state of the system yields

$$E_0 = \int d\mathbf{r} \rho_0(\mathbf{r}) v(\mathbf{r}) + \langle \Psi_0 | \hat{\mathcal{T}} + \hat{\mathcal{U}} | \Psi_0 \rangle = \int d\mathbf{r} \rho_0(\mathbf{r}) v(\mathbf{r}) + Q[\rho_0] \tag{4.41}$$

which completes the proof. □

We have thus replaced the too strict V–representability condition with the much weaker N–representability condition. It should be noted that

Remark 1. When the density is V–representable, $F_{HK}[\rho] = Q[\rho]$, that is, the Lieb–Levy formulation is equivalent to the Hohenberg–Kohn formulation. This, and the fact that non V–representable densities are not commonly found in physical problems, allows to safely use the Hohenberg–Kohn formulation in a vast majority of cases.

Remark 2. Since $|\Psi_0\rangle = |\Psi^{\rho_0}_{\min}\rangle$, the ground state can be found in terms of the density, even if the external potential $\hat{\mathcal{V}}$ is unknown, exploring the wave functions until the one which minimizes the energy is found. As such, there is no restriction on the number of wave functions that would satisfy this condition. Hence, this resolves the degeneracy issue, as, in principle, any of the wave functions belonging to a degenerate ground state can be identified.

4.3 The Thomas–Fermi model

Historically, the first attempt at solving a physical problem in terms of density, well before the formalisation of Density Functional Theory, was carried out independently by Thomas and Fermi in 1927 [9, 10]. They proposed a model for the kinetic energy of a homogeneous free electron gas.

Let us consider a model system composed of non–interacting fermions; we may divide the space in small cubic subcells of volume V each containing N particles. In the ground state, only the levels up to a certain value ϵ_F are occupied. This value is called the Fermi energy. In the reciprocal space, the momentum vectors of the occupied states form a sphere (Fermi sphere) whose radius k_F must be sufficient to hold $N/2$ states, that is $N/2$ small boxes of volume Δk. This condition relates to the density through the following:

$$\frac{4\pi}{3}k_F^3 = \frac{N}{2}\Delta k = \frac{N}{2}\frac{(2\pi)^3}{V} \tag{4.42}$$

and since $N/V = \rho$, it follows

$$k_F = (3\pi^2\frac{N}{V})^{1/3} = (3\pi^2\rho)^{1/3} \tag{4.43}$$

or, back in real space:

$$\epsilon_F = \frac{\hbar^2 k_F^2}{2m} = \frac{\hbar^2}{2m}(3\pi^2\rho)^{2/3}\ . \tag{4.44}$$

The fraction of electrons with momentum between k and $k + dk$ is

$$g(k)dk = \begin{cases} \dfrac{4\pi k^2 dk}{4/3\pi^3 k_F^3} & \text{if } p \leqslant p_F \\ 0 & \text{otherwise} \end{cases} \tag{4.45}$$

and the kinetic energy per unit volume is

$$t(r) = \int_0^{k_F} \frac{p^2}{2m}\rho(r)g(k)dk = \int_0^{k_F} \frac{p^2}{2m}\rho(r)\frac{4\pi k^2 dk}{4/3\pi^3 k_F^3} = \tag{4.46}$$

$$= \int_0^{k_F} \frac{p^2}{2m}\rho(r)\frac{3}{k_F^3}k^2 dk = \frac{3\hbar^2}{2mk_F^3}\rho(r)\int_0^{k_F} k^2 dk = \tag{4.47}$$

$$= \frac{3\hbar^2}{10m}\rho(r)k_F^2 \tag{4.48}$$

which, using Equation 4.43, becomes

$$t(r) = \frac{3\hbar^2}{10m}(2\pi^2)^{2/3}[\rho(r)]^{5/3} = C_F[\rho(r)]^{5/3}\ . \tag{4.49}$$

The total kinetic energy is obtained simply integrating over all the space:

$$T[\rho] = \int_\Omega t(r)dr = C_F\int_\Omega [\rho(r)]^{5/3}dr\ . \tag{4.50}$$

Let us now introduce the potential terms as in Equation 4.9 and minimize the total energy with the Lagrange multiplier μ under the condition that the total number of electrons is N:

$$\frac{\delta}{\delta\rho(\mathbf{r})}E[\rho] = 0 = \tag{4.51}$$

$$= \frac{\delta}{\delta\rho(\mathbf{r})}\left[T[\rho] + U[\rho] + \int V(\mathbf{r}')\rho(\mathbf{r}')d\mathbf{r}' - \mu\left(\int \rho(\mathbf{r}')d\mathbf{r}' - N\right)\right]\ . \tag{4.52}$$

From the properties of functional derivatives we know that

$$\frac{\delta\rho(\mathbf{r}')}{\delta\rho(\mathbf{r})} = \delta(\mathbf{r}-\mathbf{r}') \tag{4.53}$$

whence follows

$$\frac{\delta T[\rho]}{\delta\rho(\mathbf{r})} + \frac{\delta U[\rho]}{\delta\rho(\mathbf{r})} + V(\mathbf{r}) - \mu = 0\ , \tag{4.54}$$

that is, the Euler–Lagrange equation of the problem.
Within the Hartree–Fock model, the exchange energy of a homogeneous fermion gas is given by the cubic root of the density. The functional of the internal potential is then

$$U[\rho] = J[\rho] + V_{xc}[\rho] = \frac{1}{2}\int d\mathbf{r}d\mathbf{r}'\frac{\rho(\mathbf{r})\rho(\mathbf{r}')}{|\mathbf{r}-\mathbf{r}'|} + C\int[\rho(\mathbf{r})]^{4/3}d\mathbf{r}\ . \tag{4.55}$$

Combining the external potential, the Coulomb interaction and the exchange term in one effective potential V_{eff} yields the Euler–Lagrange equations of the Thomas–Fermi model:

$$C_F[\rho(\mathbf{r})]^{2/3} + V_{eff}(\mathbf{r}) - \mu = 0 \ , \tag{4.56}$$

where the Lagrange multiplier has the meaning of a chemical potential.
This model, as elegant as it is, does not however provide an accurate solution for chemical systems, such as a stable molecule or the closed–shell structure of a noble gas. The kinetic energy functional can be improved by adding the Weizsäcker correction [11], but in order to accomplish an accurate description of real physical systems, we must take a step back and consider a description of the system in terms of orbitals.

4.4 Kohn–Sham equations

The Hohenberg–Sham theorems provide a solid base for Density Functional Theory and allow to determine the ground state density, and subsequently the ground state energy, of a system, variationally with respect to densities instead of orbitals, with obvious advantages. The resulting self–consistent scheme, introduced in 1965, is known as the Kohn–Sham method [12].
Let us consider a system composed of N non interacting electrons, that is assume that $\hat{\mathcal{U}} = 0$. The Hamiltonian will then be

$$\hat{\mathcal{H}}_s = \hat{\mathcal{T}}_s + \hat{\mathcal{V}}_s \tag{4.57}$$

where $\hat{\mathcal{V}}_s$ is in the usual form $V = \sum_{i=1}^{N} v_s(\mathbf{r}_i)$. The Hohenberg–Kohn theorems are applicable and establish that a unique functional must exist such that

$$E_s[\rho] = T_s[\rho] + \int d\mathbf{r}\rho(\mathbf{r})v_s(\mathbf{r}) \tag{4.58}$$

where the subscript s of T_s indicates that this is the universal kinetic energy functional for non interacting systems. The reason for this approximation is that for non interacting systems the kinetic energy can be calculated easily. The solution to this problem consists in a Slater determinant $|\Psi_s\rangle$ constructed with the N spin–orbitals $\{\psi(\mathbf{x})\} = \{\xi(\sigma)\phi(\mathbf{r})\}$ that satisfy the following:

$$\left(-\frac{\hbar^2}{2m}\nabla^2 + V_s(\mathbf{r})\right)\phi_\lambda(\mathbf{r}) = \epsilon_\lambda\phi_\lambda(\mathbf{r}) \qquad\qquad \epsilon_1 \leqslant \epsilon_2 \leqslant ... \leqslant \epsilon_{N/2} \ \ (\lambda = 1 : N/2) \tag{4.59}$$

where we have taken into account the fact that, if $\mathbf{x}$ is the general coordinate that includes spin states, every orbital λ is occupied by two electrons. The corresponding density is

$$\rho(\mathbf{x}) = \sum_{i-1}^{N}|\psi_i(\mathbf{x})|^2 \qquad \Rightarrow \qquad \rho(\mathbf{r}) = 2\sum_{\lambda-1}^{N/2}|\phi_i(\mathbf{r})|^2 \ . \tag{4.60}$$

As $|\Psi_s\rangle$ is a functional of ρ, so are all the orbitals $\{\phi_\lambda\}$.
The kinetic energy of a non interacting system will then be

$$T_s[\rho] = \langle\Psi_s|\hat{\mathcal{T}}|\Psi_s\rangle = -\frac{\hbar^2}{2m}2\sum_{\lambda=1}^{N/2}\langle\phi_\lambda|\nabla^2|\phi_\lambda\rangle = -\frac{\hbar^2}{2m}2\sum_{\lambda=1}^{N/2}\int d\mathbf{r}\phi_\lambda^*(\mathbf{r})\nabla^2\phi_\lambda(\mathbf{r})\ . \quad (4.61)$$

But the kinetic energy T_s of a non interacting system is different from the kinetic energy of an interacting system, that is, the true T, which contains non–diagonal terms. The idea is to include the difference in an effective potential:

$$\frac{\delta T_s[\rho]}{\delta\rho(\mathbf{r})} + V_{eff} - \mu = 0 \quad (4.62)$$

where

$$V_{eff} = V(\mathbf{r}) + \frac{\delta U[\rho]}{\delta\rho(\mathbf{r})} + \left(\frac{\delta T[\rho]}{\delta\rho(\mathbf{r})} - \frac{\delta T_s[\rho]}{\delta\rho(\mathbf{r})}\right) \quad (4.63)$$

which leads to the Kohn–Sham equations

$$\left(-\frac{\hbar^2}{2m}\nabla^2 + V_{eff}(\mathbf{r})\right)\phi_\lambda(\mathbf{r}) = \epsilon_\lambda\phi_\lambda(\mathbf{r}) \quad (4.64)$$

whose iterative solutions give the Kohn–Sham orbitals $\{\phi_\lambda\}$.
The problem now reduces to finding the appropriate expression for the effective potential (in particular, for the exchange–correlation potential, which now includes also the kinetic energy correction), which determines the ground state density, rather than finding the ground state density itself.
It has to be noted that the Kohn–Sham orbitals represent an auxiliary system with no physical meaning, and it can be shown that the auxiliary eigenstate $|\Psi_s\rangle$ is not the real $|\Psi\rangle$, but yields the exact density if the exchange potential is known. In other words, the Kohn–Sham scheme is, in principle, exact, but the exchange potential is generally unknown.

4.4.1 Exchange–correlation potential and exchange–correlation hole.

The exchange–correlation energy is defined as the difference between the energy of an interacting system and that of the same system interacting only by means of the Coulomb interaction:

$$E_{xc}[\rho] = (U[\rho] - J[\rho]) + (T[\rho] - T_s[\rho])\ . \quad (4.65)$$

Because the functional derivative of the charge density with respect to an orbital is

$$\frac{\delta\rho(\mathbf{r}')}{\delta\phi_\lambda^*(\mathbf{r})} = \frac{\delta}{\delta\phi_\lambda^*(\mathbf{r})}\sum_{\lambda'}|\phi_{\lambda'}|^2 = \phi_\lambda\delta(\mathbf{r}-\mathbf{r}') \quad (4.66)$$

we may calculate the potential contributions as functional derivatives of the energy term. For the Coulomb interaction:

$$\frac{\delta J[\rho]}{\delta \phi_\lambda^*(\mathbf{r})} = -e \int d\mathbf{r}' J(\mathbf{r}')\phi_\lambda(\mathbf{r})\delta(\mathbf{r}-\mathbf{r}') = -eJ(\mathbf{r})\phi_\lambda(\mathbf{r}) \; . \tag{4.67}$$

For the external potential:

$$\frac{\delta E_{e-ion}[\rho]}{\delta \phi_\lambda^*(\mathbf{r})} = \int d\mathbf{r}' V(\mathbf{r}')\phi_\lambda(\mathbf{r})\delta(\mathbf{r}-\mathbf{r}') = V(\mathbf{r})\phi_\lambda(\mathbf{r}) \; . \tag{4.68}$$

For the exchange–correlation energy:

$$\frac{\delta E_{xc}[\rho]}{\delta \phi_\lambda^*(\mathbf{r})} = e \int d\mathbf{r}' V_{xc}(\mathbf{r}')\phi_\lambda(\mathbf{r})\delta(\mathbf{r}-\mathbf{r}') = V_{xc}(\mathbf{r})\phi_\lambda(\mathbf{r}) \; . \tag{4.69}$$

Hence, the effective potential has the form

$$V_{eff}(\mathbf{r}) = V(\mathbf{r}) - eJ(\mathbf{r}) + V_{xc}(\mathbf{r}) \tag{4.70}$$

and

$$V_{xc} = \frac{\delta E_{xc}[\rho]}{\delta \phi_\lambda^*(\mathbf{r})} = \frac{\delta}{\delta \phi_\lambda^*(\mathbf{r})}\{U[\rho] - J[\rho] + T[\rho] - T_s[\rho]\} \; . \tag{4.71}$$

This potential only depends on the number of electrons but not on the external potential, that is, it needs to be calculated for every given charge density.

Physically, the exchange–correlation interaction tends to pull electrons apart; this gave rise to the description of the phenomenon in terms of a hole surrounding each electron. The exchange–correlation hole is defined as the change in charge density at $\mathbf{r}$ due to the presence of an electron at $\mathbf{r}'$, that is, the joint probability of finding an electron at $\mathbf{r}$ given that there is another electron at $\mathbf{r}'$:

$$\rho_{xc}(\mathbf{r}|\mathbf{r}') := \rho(\mathbf{r}|\mathbf{r}') - \rho(\mathbf{r}) \; . \tag{4.72}$$

The exchange–correlation hole cannot be calculated analytically, nor can the exchange–correlation energy be an analytic functional. Generally, in practical implementations, the exchange and correlation terms are separated.

A number of methods have been proposed over the years, such as the Wigner crystal model [13], the Gell–Mann and Breuckner model [14], and the most widely used Quantum Monte Carlo calculated potentials such as the Perdew–Zunger [15] and Vosko–Wilk–Nusair potentials [16]. Whatever the method of choice is, there are some restrictions that need to be obeyed, such as:

1. Sum rule: The hole must integrate over space to -1 per electron.

2. Uniform scaling [17]:

$$E_x[\rho_\lambda] = \lambda E_x[\rho] \tag{4.73}$$

$$E_c[\rho_\lambda] > \lambda E_c[\rho] \qquad for \lambda > 1 \tag{4.74}$$

$$E_c[\rho_\lambda] < \lambda E_c[\rho] \qquad for \lambda < 1 \; . \tag{4.75}$$

3. One–electron limit: in the one–electron limit, the exchange energy still exists and it is equal to the negative Hartree energy.

4. Lieb–Oxford bound [18]:

$$E_{xc}[\rho] \geqslant -D \int d\mathbf{r} \rho^{4/3}(\mathbf{r}) \qquad 1.44 \leqslant D \leqslant 1.86 \; . \tag{4.76}$$

Local Density Approximation

In the Local Density Approximation (LDA), one assumes that the exchange–correlation potential depends only on the value of the charge density, that is:

$$E_{xc}^{LDA} = \int d\mathbf{r} f_{xc}(\rho(\mathbf{r})) = \int d\mathbf{r} \rho(\mathbf{r}) \epsilon_{xc}(\rho(\mathbf{r})) \tag{4.77}$$

therefore, from the properties of functional derivatives:

$$V_{xc}^{LDA} = \frac{\partial f_{xc}}{\partial \rho} = \epsilon_{xc}(\rho(\mathbf{r})) + \rho(\mathbf{r}) \left(\frac{\partial \epsilon_{xc}(\rho)}{\partial \rho} \right) \Bigg|_{\rho=\rho(\mathbf{r})} \; . \tag{4.78}$$

Even though LDA is a rather crude approximation, it performs surprisingly well. This is in part explained with the fact that LDA typically underestimates the correlation and overestimates the exchange, causing the errors to partly cancel. Moreover, among its advantages are the full locality, the compliance with the uniform scaling rule (but not with the non–uniform scaling). It does not satisfy the one–electron limit, but this can be fixed by adding a self–interaction correction.
LDA functionals, also in the spin–dependent flavour (LSDA) have been widely used until the 1990s, when they have been overruled by more sophisticated functionals, which include the dependence on the gradient of the density.

Generalized Gradient Approximation

In the Generalized Gradient Approximation (GGA), one assumes that the exchange–correlation potential depends on the values of both the charge density and its gradient, that is:

$$E_{xc}^{LDA} = \int d\mathbf{r} f_{xc}(\rho(\mathbf{r}), \nabla\rho(\mathbf{r})) = \int d\mathbf{r} \rho(\mathbf{r}) \epsilon_{xc}(\rho(\mathbf{r}), \nabla\rho(\mathbf{r})) \tag{4.79}$$

and

$$V_{xc}^{GGA} = \frac{\partial f_{xc}}{\partial \rho} - \nabla \frac{\partial f_{xc}}{\partial \nabla \rho} \, . \tag{4.80}$$

The gradient of the density is usually determined numerically.

4.4.2 Self–consistent Iterative scheme

Computationally, the Kohn–Sham method for DFT is implemented in an iterative scheme, as the Kohn–Sham equations are a nonlinear set of differential equations. Roughly, with i marking the iteration step counter, the scheme may be summarized as follows:

1. An existing distribution $\rho^{(i)}$ (initial guess distribution for the first step $i = 0$) is used to construct the potential terms: the external potential V by means of an Ewald summation over the ions, the Coulomb potential J solving the Poisson equation for the charge distribution, and the exchange–correlation potential V_{xc} determined point–to–point from tabulated values. The single terms are then summed to obtain the effective potential

$$V_{eff}^{(i)} = V^{(i)} + J^{(i)} + V_{xc}^{(i)} \, . \tag{4.81}$$

2. The corresponding Kohn–Sham equation

$$\left(-\frac{\hbar^2}{2m} \nabla^2 + V_{eff}^{(i)}(\mathbf{r}) \right) \phi_{\lambda)}^{(i)}(\mathbf{r}) = \epsilon_{\lambda}^{(i)} \phi_{\lambda,}^{(i)}(\mathbf{r}) \tag{4.82}$$

   is solved either by matrix inversion or some other method such as a predictor–corrector scheme.

3. The total energy is calculated as a sum over the occupied space and the corrections:

$$E^{(i)} = \sum_{\lambda}^{occ} \epsilon_{\lambda}^{(i)} - J^{(i)} + E_{xc}^{(i)} - \int V_{xc}^{(i)}(\mathbf{r}) \rho^{(i)}(\mathbf{r}) d\mathbf{r} \, . \tag{4.83}$$

4. The energy thus obtained is compared with the previous one. If they are equal within a predetermined accuracy treshold δ, the iteration is stopped:

$$\text{if} \qquad E^{(i)} - E^{(i-1)} < \delta \qquad \text{Stop;} \tag{4.84}$$

   if not, the calculation proceeds to the next step.

5. All the occupied states are summed up to obtain a new density

$$\rho_{new}^{(i)} = \sum_{\lambda}^{occ} |\phi_{\lambda}^{(i)}|^2 \, . \tag{4.85}$$

6. Part of this new charge density is mixed with the previous charge density:

$$\rho^{(i+1)} = \mathcal{M}[\rho^{(i)}, \rho^{(i)}_{new}] \tag{4.86}$$

   where the operator $\mathcal{M}$ represents the mixing algorithm of choice among the many available. This procedure ensures numerical stability.

7. Go back to step 1.

The Kohn–Sham scheme is illustrated as a flow chart in Figure 4.1.
This scheme provides a single–point calculation of the electronic ground state of the system. This means that the external potential is determined by the ionic configuration and is not, in general, the minimum of the Born–Oppenheimer potential energy surface. By virtue of the Hellmann–Feynman theorem [19, 20] (see Appendix A), the scheme above is usually embedded in a cycle of ionic relaxation, that is, after a geometry is electronically converged, the forces between the ions are calculated, then the ions are moved by a small displacement and a new self–consistent cycle is started, until the maximum force acting on the ions is smaller than a predetermined threshold. Both the speed and the reliability of a ionic relaxation depend strongly on the initial guess geometry, which must be wisely chosen, as the minimization algorithms are local and will converge to the closest local minimum instead of the global minimum. A relaxation calculation typically consists of few to few hundreds ionic steps.

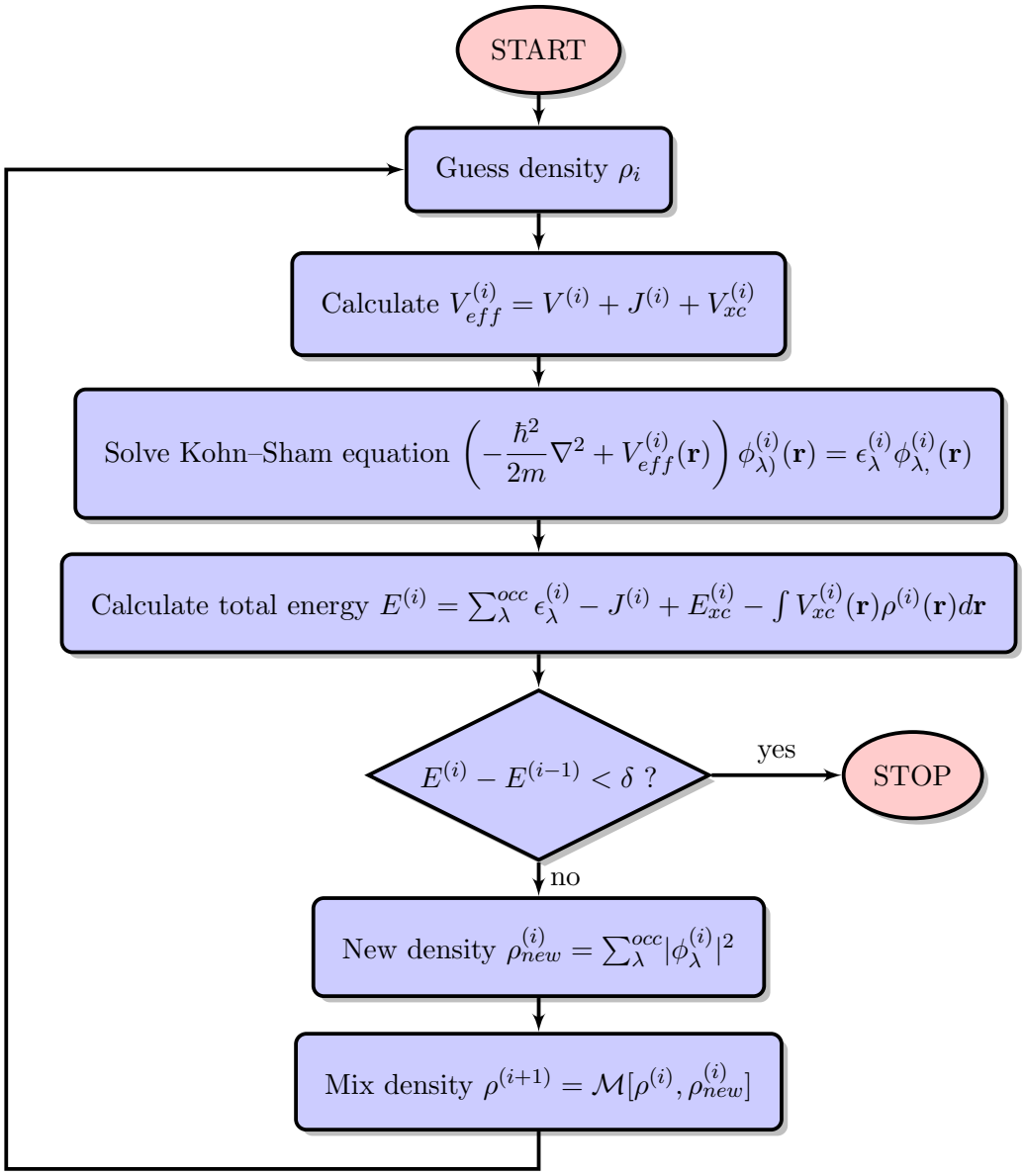

Figure 4.1: Flow chart summarizing the passages of the iterative Kohn–Sham scheme for Density Functional Theory.

REFERENCES

[1] W. Kohn. Nobel lecture: Electronic structure of matter–wave functions and density functionals. *Reviews of Modern Physics*, 71(5):1253–1266, 1999.

[2] F. Jensen. *Introduction to Computational Chemistry*. Wiley, 2 edition, 2006.

[3] P. Hohenberg and W. Kohn. Inhomogeneous electron gas. *Physical Review*, 136(3B):B864–B871, 1964.

[4] M. Levy. Universal variational functionals of electron densities, first–order density matrices, and natural spin–orbitals and solution of the v-representability problem. *Proceedings of the National Academy of Sciences*, 76(12):6062–6065, 1979.

[5] M. Levy and J. P. Perdew. In defense of the Hohenberg–Kohn theorem and density functional theory. *International Journal of Quantum Chemistry*, 21(2):511–513, 1982.

[6] E. H. Lieb. Thomas–Fermi and related theories of atoms and molecules. *Reviews of Modern Physics*, 53:603–641, 1981.

[7] E. H Lieb. Density functionals for Coulomb systems. *International Journal of Quantum Chemistry*, 24(3):243–277, 1983.

[8] J. Harriman. Orthonormal orbitals for the representation of an arbitrary density. *Physical Review A*, 24(2):680–682, 1981.

[9] L. H. Thomas. The calculation of atomic fields. *Mathematical Proceedings of the Cambridge Philosophical Society*, 23(05):542, 1926.

[10] E. Fermi. Eine statistische methode zur bestimmung einiger eigenschaften des atoms und ihre anwendung auf die theorie des periodischen systems der elemente. *Zeitschrift für Physik*, 48(1-2):73–79, 1928.

[11] C. F. V. Weizsäcker. Zur theorie der kernmassen. *Zeitschrift für Physik*, 96(7-8):431–458, 1935.

[12] W. Kohn and L. J. Sham. Self–consistent equations including exchange and correlation effects. *Physical Review*, 140(4A):A1133–A1138, 1965.

[13] E. Wigner. On the interaction of electrons in metals. *Physical Review*, 46(11):1002–1011, 1934.

[14] M. Gell-Mann and K. Brueckner. Correlation energy of an electron gas at high density. *Physical Review*, 106(2):364–368, 1957.

[15] J. P. Perdew. Self–interaction correction to density–functional approximations for many–electron systems. *Physical Review B*, 23(10):5048–5079, 1981.

[16] S. H. Vosko, L. Wilk, and M. Nusair. Accurate spin–dependent electron liquid correlation energies for local spin density calculations: a critical analysis. *Canadian Journal of Physics*, 58(8):1200–1211, 1980.

[17] M. Levy and J. P. Perdew. Hellmann–Feynman, virial, and scaling requisites for the exact universal density functionals. Shape of the correlation potential and diamagnetic susceptibility for atoms. *Physical Review A*, 32(4):2010–2021, 1985.

[18] E. H. Lieb and S. Oxford. Improved lower bound on the indirect Coulomb energy. *International Journal of Quantum Chemistry*, 19(3):427–439, 1981.

[19] H. Hellmann. *Einführung in die Quantenchemie*, page 285. F. Deuticke, 1937.

[20] R. P. Feynman. Forces in molecules. *Physical Review*, 56:340–343, 1939.

Chapter 5

Theory of STM

5.1 Electron transport in the low–conductance regime

In Scanning Tunneling Microscopy the main physical obstacle to the transport of electrons is the vacuum barrier between the sample and the probe tip. In this case variations of the conductance across the tunneling barrier due to electron–electron interactions can be considered small enough to be treated with perturbation theory. Therefore, the main task is a suitable description of the transport across the barrier. Additional effects, such as electron–phonon excitations, can be incorporated as extensions of the basic model. Together with the variation of the tunneling current due to the magnetic properties of the system, they account for the bulk of experimental observations. At present, the following four theoretical models of electron tunneling are used in nearly all simulations of STM processes:

- the Tersoff–Hamann approach [1, 2]: isocurrent contours are derived from the electronic structure of the sample alone;
- the Bardeen, or transfer Hamiltonian approach [3]: the electronic structure of the tip is included;
- the Landauer–Büttiker approach [4]: equivalent to the Bardeen's method, but it includes multiple tunneling pathways between the tip and the surface;
- the Keldysh [5] approach, or non–equilibrium Green's function approach: it incorporates inelastic effects.

The models are listed in order of increasing complexity. For the purpose of the present Thesis, the Tersoff–Hamann approach has proved sufficiently accurate and therefore will be presented in more detail. We will present Bardeen's tunneling derivation first, as it provides the basis upon which the Tersoff–Hamann model is built. A thorough treatment can be found in Ref. [6].

5.1.1 Bardeen's tunneling model

We will here use the equivalent time–dependent derivation developed by Julian Chen [7], as it renders the explicit relation to the wave functions clearer. To do so, it is assumed that:

- in the absence of current, the whole system is described by a complete set of orthonormal eigenstates, conveniently split into two subsets, one located at the sample, marked with μ, and one located at the tip, marked with ν. Under these conditions, the Hamiltonians of the two subsets differ only by their potentials, which we will refer to as, respectively, U_S and U_T.
- the total potential is the sum of the two potentials mentioned above. Since both potentials decay exponentially, their overlap at a surface belonging to the vacuum range of the junction will be negligible.

At $t < 0$, the tip potential is turned off. Hence, the Schrödinger equation of the sample is

$$\left(-\frac{\hbar^2}{2m}\nabla^2 + U_S\right)\psi_\mu = E_\mu\psi_\mu \ . \tag{5.1}$$

Likewise, the Schrödinger equation of the tip is

$$\left(-\frac{\hbar^2}{2m}\nabla^2 + U_T\right)\psi_\nu = E_\nu\psi_\nu \ . \tag{5.2}$$

At $t = 0$ the tip is turned on and the sample follows the time–dependent Schrödinger equation:

$$\left(-\frac{\hbar^2}{2m}\nabla^2 + U_S + U_T\right)\Psi = i\hbar\frac{\partial\Psi}{\partial t} \ . \tag{5.3}$$

The wave function can be expanded in terms of the tip states:

$$\Psi = \sum_\nu a_\nu(t)\psi_\nu e^{-iE_\nu t/\hbar} \ . \tag{5.4}$$

If we assume that

$$a_\nu(t) = \langle\psi_\nu|\psi_\mu\rangle e^{-i(E_\mu - E_\nu)t/\hbar} + c_\nu(t) \tag{5.5}$$

with $c(0) = 0$, we have rewritten the wave function as a linear combination of the surface state with all the tip states:

$$\Psi = \psi_\mu e^{-iE_\mu t/\hbar} + \sum_\nu c_\nu(t)\psi_\nu e^{-E_\nu t/\hbar}. \tag{5.6}$$

The transition amplitude $c_\nu(t)$, whose square is the transition probability, is given by first order perturbation theory as

$$c_\nu(t) = \frac{1}{\hbar}\int_0^t dt' e^{i(E_\nu - E_\mu)t'/\hbar}\langle\psi_\nu|U_T|\psi_\mu\rangle \tag{5.7}$$

Let us now consider the following general relations:

$$\left|\int_0^t dt' e^{i\omega t}\right|^2 = \left|\frac{\sin(\omega t/2)}{\omega/2}\right|^2 \ ; \tag{5.8}$$

$$\lim_{t\to\infty}\frac{\sin^2(\alpha t}{\alpha^2 t} = \pi\delta(\alpha)\ . \tag{5.9}$$

We may apply them to Equation 5.7 in the limit of quasi–continuous spectrum, such as in metals. We hence obtain, from the transition amplitude, the transition rate as

$$\omega_{\mu\nu} = \frac{|c_\nu|^2}{t} = \frac{2\pi}{\hbar}\delta(E_\nu - E_\mu)|\langle\psi_\nu|U_T|\psi_\mu\rangle|^2 \tag{5.10}$$

In other words, a transition only occurs when $E_\nu = E_\mu$.
Let us now consider the matrix element

$$M_{\mu\nu} = \int_\Omega d\tau\psi_\nu^* U_T\psi_\mu = \int_\Omega d\tau\psi_\nu^*\left(E_\nu - \frac{\hbar^2}{2m}\nabla^2\right)\psi_\mu \tag{5.11}$$

where Ω is only the region of the tip, as the potential is zero outside. Using the previous result, that is, $E_\mu = E_\nu$, we may rewrite it as

$$M_{\mu\nu} = \int_\Omega d\tau(\psi_\mu\nabla^2\psi_\nu^* - \psi_\nu^*\nabla^2\psi_\mu)\ . \tag{5.12}$$

Using Gauss's theorem, we may transform the volume integral into a surface integral:

$$M_{\mu\nu} = \frac{\hbar^2}{2m}\int_S d\sigma(\psi_\nu^*\nabla\psi_\mu - \psi_\mu\nabla^2\psi_\nu)\ . \tag{5.13}$$

The transition matrix is related to the tunneling current I through the following relation:

$$I = \frac{4\pi e}{\hbar}\int_{-\infty}^{\infty} d\epsilon[f(E_F - eV + \epsilon) - f(E_F + \epsilon)]\rho_S(E_F - eV + \epsilon)\rho_T(E_F + \epsilon)|M_{\mu\nu}|^2 \tag{5.14}$$

where ρ_S and ρ_T indicate, respectively, the local density of states of the surface and the tip.

5.1.2 The Tersoff–Hamann approach

This model was developed in 1983 by Tersoff and Hamann [1, 2] as an approximation of the Bardeen description of the electron tunneling. Here, the STM tip is assumed to be consisting of a single spherically symmetric state, as shown in Figure 5.1. Therefore, a detailed description of the electronic structure of the tip is not required and STM images are modelled by means of the electronic structure of the surface alone. The convenience of such approach appears evident considering that, usually, the exact structure of the tip is unknown and non–reproducible. Despite its apparent simplicity and the existence of extended models, the Tersoff–Hamann model continues to be the core of every STM simulation and gives qualitative results in a broad range of cases.
Following the treatment that can be found in the original Tersoff and Haman papers [1, 2], in Bardeen's formalism, the tunneling current is given by

$$I = \frac{2\pi e}{\hbar} \sum_{\mu,\nu} f(E_\mu)[1 - f(E_\nu + eV)]|M_{\mu\nu}|^2 \delta(E_\mu - E_\nu) \tag{5.15}$$

where μ and ν label different electronic states of the probe and the sample, $f(E) = [1+e^{(E-E_F)/k_bT}]^{-1}$ is the Fermi distribution, V is the bias voltage, $M_{\mu\nu}$ is the tunneling matrix element between states $|\mu\rangle$ and $|\nu\rangle$, and E_ν is the energy of the state $|\nu\rangle$ in the absence of tunneling. Equation 5.15 is formally equivalent to a first order perturbation expression, but conceptually differs in that $|\mu\rangle$ and $|\nu\rangle$ are non–orthogonal eigenstates of different Hamiltonians.
To the limit of small bias voltage and temperature, which covers the large majority of ordinary experiments, the tunneling current becomes

$$I = \frac{2\pi}{\hbar} e^2 V \sum_{\mu,\nu} |M_{\mu\nu}|^2 \delta(E_\mu - E_F)\delta(E_\nu - E_F) \; . \tag{5.16}$$

From Bardeen's derivation, the matrix element is the integral of the current operating over any surface S lying entirely within the vacuum region between the tip and the sample:

$$M_{\mu\nu} = \frac{\hbar^2}{2m} \int_S d\sigma (\psi_\mu^* \nabla \psi_\nu - \psi_\nu^* \nabla \psi_\mu) \; . \tag{5.17}$$

To evaluate it, let us expand the sample wave function in the general form for small potential

$$\psi_\nu = \Omega_s^{-1/2} \sum_G a_G \exp[z(\kappa^2 + |\mathbf{k}_\parallel + \mathbf{G}|^2)^{1/2}] \exp[i(\mathbf{k}_\parallel + \mathbf{G}) \cdot \mathbf{x}] \tag{5.18}$$

where Ω_s is the sample volume, κ is the inverse decay length of the wave functions in vacuum, and $\mathbf{k}_G = \mathbf{k}_\parallel + \mathbf{G}$, where $\mathbf{k}_\parallel$ is the Bloch wave vector and $\mathbf{G}$ is a reciprocal lattice vector.

In the locally spherical tip approximation, as shown in Figure 5.1, R is the curvature radius around the centre $\mathbf{r}_0$, and d is the minimum distance between the tip and the sample. In this asymptotic region, the wave functions of the tip are assumed to be spherical:

$$\psi_\mu = \Omega_t^{-1/2} c_t \kappa R e^{\kappa R} \frac{e^{-\kappa|\mathbf{r}-\mathbf{r_0}|}}{\kappa|\mathbf{r}-\mathbf{r_0}|} \tag{5.19}$$

where Ω_t is the volume of the probe. Of note, since κ is proportional to the work function ϕ, we are here assuming that the work function of the tip and that of the sample are equal. Using the fact that

$$\frac{e^{\kappa\mathbf{r}}}{\kappa\mathbf{r}} = \int d^2q\, b(\mathbf{q}) \exp[-(\kappa^2+q^2)^{-1/2}|z|] \exp[i\mathbf{q}\cdot\mathbf{x}] \;, \tag{5.20}$$

where $b(\mathbf{q}) = (2\pi)^{-1}\kappa^{-2}(1+g^2/\kappa^2)^{-1/2}$, we expand the wave function of the tip in the same form as that of the surface, which, substituted in Equation 5.17 and after some working out, gives

$$M_{\mu\nu} = \frac{\hbar^2}{2m}\frac{4\pi}{\kappa}\Omega_t^{-1/2}\kappa R e^{\kappa R}\psi_\nu(\mathbf{r_0}) \;. \tag{5.21}$$

Substituting the latter in Equation 5.16 yields the result

$$I = \frac{32\pi^3 e^2 V \phi^2 D_t E_F R^2}{\hbar_{-1}\kappa^{-4}} e^{2\kappa R} \sum_\nu |\psi_\nu(\mathbf{r}_0)|^2 \delta(E_\nu - E_F) \;, \tag{5.22}$$

where D_t is the density of states per unit volume of the tip. In other words:

$$I \propto \sum_\nu |\psi_\nu(\mathbf{r}_0)|^2 \delta(E_\nu - E_F) := \rho(\mathbf{r}_0, E_F) \;. \tag{5.23}$$

The spherical tip approximation consists in having evaluated the matrix element only for an s–wave of the tip.

The current only depends on the undistorted wave function of the sample. Since $\rho(\mathbf{r}_0, E_F)$ is the local density of states (LDOS) of the sample, the tunneling current depends on the surface LDOS at the position of the tip. If the current is kept constant, the tip follows a contour of constant LDOS.

The sharper is the tip, the more accurate is the approximation. Realistically, one can imagine the tip to be terminated with a single atom, supported on a cluster or small plateau.

5.2 Figures

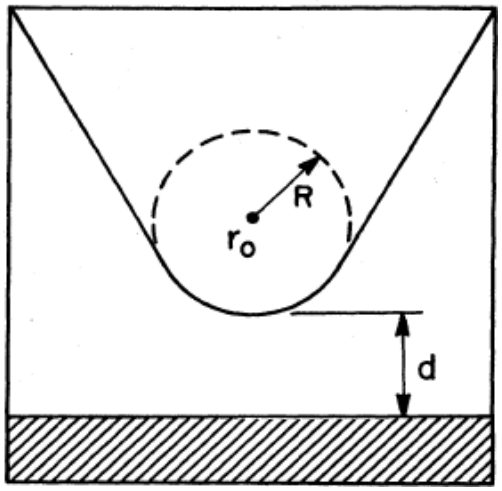

Figure 5.1: Schematic representation of the Tersoff–Hamann model tip. The tip is of arbitrary shape but it is assumed to be terminating with a single atom. We assume the terminal atom to be a point centred in $\mathbf{r}_0$, whose charge density is locally spherically symmetric. R is the curvature radius, and d is the distance of nearest approach to the sample [1, 2].

REFERENCES

[1] J. Tersoff and D. R. Hamann. Theory and Application for the Scanning Tunneling Microscope. *Physical Review Letters*, 50(25):1998–2001, June 1983.

[2] J. Tersoff and D R Hamann. Theory of the scanning tunneling microscope. *Physical Review B*, 31(2):805–813, January 1985.

[3] J. Bardeen. Tunnelling from a Many-Particle Point of View. *Physical Review Letters*, 6(2):57–59, January 1961.

[4] M. Büttiker, Y. Imry, R. Landauer, and S. Pinhas. Generalized many–channel conductance formula with application to small rings. *Physical Review B*, 31(10):6207–6215, May 1985.

[5] L. V. Keldysh. Diagram technique for nonequilibrium processes. *Sov. Phys. JETP*, 20(4):1018–1026, 1965.

[6] A Foster and W. A. Hofer. *Scanning Probe Microscopy: Atomic Scale Engineering by Forces and Currents (NanoScience and Technology)*. Springer, 2006.

[7] J. C. Chen. *Introduction to scanning tunneling microscopy*. Oxford University Press, 1993.

Chapter 6

Reactions on surfaces

A problem of central importance in theoretical chemistry, and no less in condensed matter theory and surface science, is the evaluation, reproduction and prediction of reaction rates. The fundamental background is provided by Transition State Theory, developed independently in the 30's by Henry Eyring [1], Meredith Gwynne Evans and Michael Polanyi [2] and further formalized by Eugene Wigner [3]. It postulates the existence of a well defined Transition State whose features are intermediate between those of the reactants and the products.

From a mathematical point of view, a reaction can be described as happening along a Minimum Energy Path connecting a point A (reactants) with a point B (products) of the ground state potential energy hypersurface. The transition state will then be the configuration the system assumes at the maximum of said path, that is, a saddle point of the surface (see Fig. 6.1). The energy difference between the reactants and the transition state is the activation barrier of the reaction and will determine its rate. For a given reaction, and relative path, there could be more than one stage, hence more than one transition state. In that case, the reaction rate will be controlled only by the highest activation barrier (slow stage).

It should be noted that this theory only refers to thermal reactions, that is, those which involve the evolution of the system along the electronic ground state hypersurface. For reactions involving excited states, as in electron– or light–induced reactions, a wholly different treatment is needed.

In the present Chapter, we will review the fundamentals of Transition State Theory, as well as some methods for the search of minimum energy paths and saddle points, with particular focus on the one that has been used throughout the present Thesis, that is, the Nudged Elastic Band Method.

6.1 Transition State Theory

Similarly to the collision theory, with which it shares some basic ideas, the transition state theory describes a macroscopic phenomenon (the reaction rate) starting from

the motion of particles at the microscopic scale. However, unlike the first, it does not consider the molecules as hard spheres, but it takes their degrees of freedom into account.
In Transition State Theory, the reactants move on the potential energy surface along a minimum energy path (MEP), which has the units of a distance and corresponds to the reaction coordinate. The energy increases up to a maximum and then decreases to a new minimum where the reaction is complete. The process is illustrated in Figure 6.1. The maximum of the MEP, which is a saddle point of the potential energy surface, is defined as the *transition state*.
Transition state theory is based on two basic assumptions:

- the Born–Oppenheimer approximation is valid;
- the velocities of the molecules follow the Maxwell–Boltzmann distribution.

Furthermore, three more strict hypotheses need to be satisfied:

(i) *Non–recrossing path:* for a system with D degrees of freedom, a dividing surface of dimensionality $D-1$ can be identified such that the reactive trajectory only crosses it once. In other words, once the reactants have evolved to the point of becoming a transition state, they proceed to completeness of the reaction with no possibility of reversing their path.

(ii) At the transition point, the motion along the reaction path can be treated, separately from the other internal motions, as a translation. This is justified by the observation that, at a saddle point, the surface is locally flat.

(iii) The reactants and the transition state are in chemical equilibrium. This happens if the rate is slow enough that a Boltzmann distribution is established and maintained.

The latter condition, in particular, provides a means to tackle a formulation for the rate of reaction. Let us consider an arbitrary reaction

$$A + B \rightleftharpoons C + D \; . \tag{6.1}$$

This is, of course, a simple model reaction, while more complex cases require some adjustments in the treatment, but for our purposes it is general enough. The reaction can, under such hypotheses, be decomposed into two stages. The first one is the equilibrium between the reactants and the transition state $X^{\dagger}$, while the second one is the quantitative transformation of the transition state into the products:

$$A + B \rightleftharpoons X^{\dagger} \rightarrow C + D \; . \tag{6.2}$$

From the definition of chemical equilibrium, we may write:

$$\frac{[X^\dagger]}{[A][B]} \propto \frac{Q_{X^\dagger}}{Q_A Q_B} \tag{6.3}$$

where Q is the grand canonical partition function.

Hypothesis (i) allows us to write the rate of reaction as the flow of molecules crossing the dividing surface at the transition point per unit of time and volume, that is, the crossing frequency ν multiplied by the concentration of the activated complex:

$$R = \nu[X^\dagger] \, . \tag{6.4}$$

The crossing frequency ν can be estimated using hypothesis (ii). The molecules crossing the transition region will translate along a distance δ with a velocity v_δ. Under the assumption that half of the molecules in the state $X^\dagger$ will move towards the reagents and half towards the products, the frequency can be calculated as

$$\nu = \frac{v_\delta}{2\delta} \, . \tag{6.5}$$

Substituting 6.4 and 6.5 into Equation 6.3 we obtain

$$R = \frac{v_\delta}{2\delta} \frac{Q_{X^\dagger}}{Q_A Q_B} [A][B] \, . \tag{6.6}$$

The terms that multiply the concentrations are, by definition, the kinetic constant, that is:

$$k = \frac{v_\delta}{2\delta} \frac{Q_{X^\dagger}}{Q_A Q_B} \, . \tag{6.7}$$

This expression of the kinetic constant depends on an arbitrary constant δ that can be cancelled out using the definition of partition functions. For a perfect gas, the partition function Q is the product of the translational, vibrational, rotational and electronic partition functions, keeping in mind that, for the transition state, one of the normal modes has imaginary frequency. In other words, one of the degrees of freedom of the transition states is no longer vibrational but becomes translational.

Hence, using the definition of the one–dimensional translational partition function

$$Q^{t(1D)} = [Q^t]^{1/3} = \left[\left(\frac{2\pi m k_b T}{h^2} \right)^{3/2} V \right]^{1/3} \tag{6.8}$$

and using the Maxwell distribution for v_δ, we may rewrite

$$k = \frac{1}{2\delta}\left(\frac{2k_bT}{\pi m}\right)^{1/2} \frac{Q_{X^\dagger}^{t(1D)} Q_{X^\dagger}^{v(3N-7)} Q_{X^\dagger}^{t} Q_{X^\dagger}^{r} Q_{X^\dagger}^{e}}{Q_A Q_B} = \tag{6.9}$$

$$= \frac{1}{2\delta}\left(\frac{2k_bT}{\pi m}\right)^{1/2} \left(\frac{2\pi m k_b T}{h^2}\right)^{1/2} \delta \frac{Q_{X^\dagger}^{v(3N-7)} Q_{X^\dagger}^{t} Q_{X^\dagger}^{r} Q_{X^\dagger}^{e}}{Q_A Q_B} = \tag{6.10}$$

$$= \frac{k_bT}{h} \frac{Q_{X^\dagger}^{v(3N-7)} Q_{X^\dagger}^{t} Q_{X^\dagger}^{r} Q_{X^\dagger}^{e}}{Q_A Q_B} \, . \tag{6.11}$$

The latter is often expressed in a concise way, which is the most general formulation of the Transition State Theory kinetic constant:

$$k = \frac{k_bT}{h} \frac{Q_{X^\dagger}}{Q_R} \, , \tag{6.12}$$

where the subscript R now replaces A and B in labelling the reactants, for the sake of brevity.

Bearing in mind that

$$Q^e = g^e \exp(-E/k_bT) \, , \tag{6.13}$$

where g^e is the electronic degeneracy, Eqn 6.12 may be rewritten as

$$k = \frac{k_bT}{h} \frac{Q_{X^\dagger}^{t} Q_{X^\dagger}^{r} Q_{X^\dagger}^{v} g_{X^\dagger}^{e}}{Q_R^t Q_R^r} Q_R^v g_R^e \exp(-E_a/k_bT) \, , \tag{6.14}$$

where the activation energy E_a takes into account the Zero Point Energy difference between the reactants and the transition state and is thus defined as

$$E_e := (E_{el} + ZPE)_{X^\dagger} - (E_{el} + ZPE)_R \, . \tag{6.15}$$

Of note, Equation 6.14 has the form of the familiar Arrhenius equation, which is empirical:

$$k = A \exp\left(-E_a/k_bT\right) \tag{6.16}$$

which is, in practical applications, commonly used today. Transition State Theory provides the physical background to it.

In the Arrhenius equation, the pre–exponential factor A, also called the frequency factor, has units of s^{-1} and depends on how often properly oriented molecules collide. As it is not trivial to evaluate, its value is commonly taken as 10^{13}, but in some cases it should be chosen with care, as for slow processes, such some surface phenomena, is can be several orders of magnitude smaller.

6.2 Methods for the search for a saddle point

The validity of the Born–Oppenheimer approximation ensures that the motion of the nuclei is separated from that of the electrons, therefore the motion of the nuclei may be, in principle, treated as a classical mechanics problem of masses moving across the electronic potential surface. However, the transitions of interest are many orders of magnitude slower than vibrations, which makes molecular dynamics simulations impossible. In other words, a molecular dynamics simulation will sample mostly modes that are not relevant for a reaction, and catching the rare reactive path among them would require extremely long simulations, well beyond the computational power accessible nowadays. Hence, a different approach is needed. Over the years, many different methods have been developed, such as drag methods and chain–of–states methods, the latter including the Nudged Elastic Band method. We will here give an overview following Refs. [4, 5].

6.2.1 Drag methods

Under the category "drag methods" goes a number of methods based on the same idea (see, for example, Ref. [6]). One degree of freedom (defined the drag coordinate) is kept fixed while the other $D-1$ degrees of freedom are relaxed. The drag coordinate is then increased by a small step and the process is repeated until the system is dragged from the reactants to the products. The maximum energy along the path is taken as the activation energy.
This method has the advantage of simplicity and intuitiveness, though it can fail badly. If a reasonable guess of the reaction path is already available, the corresponding reaction coordinate can be chosen as the drag coordinate. But in absence of a good guess, the most sensible guess is a linear interpolation between the initial and the final state. In both cases, however the chosen drag coordinate can turn out to be a bad reaction coordinate.

6.2.2 Chain–of–states methods

The common idea is that several replicas of the system are connected through a path of some sort, forming a chain. Mathematically, a chain of replicas is analogous to a Feynman path integral [7]. Several chain methods have been developed over the years [8–15], but among those, only the (Climbing Image) Nudged Elastic Band converges to the true MEP without the need of evaluating second derivatives of the potential surface. For this reason, this is the scheme of choice throughout the present Thesis and we will discuss it thoroughly in Section 6.3. We will here briefly review some other chain–of–states methods.

Conjugate Peak Refinement method

The Conjugate peak refinement (CPR) method [16] requires the knowledge of the initial and final state as well as the potential and its gradient. It consists in generating and optimizing a set of images one by one, which, after the optimization, will be taken as the MEP. Each point is generated in a cycle of line maximization and conjugate gradient minimization. In the first cycle, the maximum $\mathbf{y}_1$ along the vector connecting the initial and the final state is found. Then, a minimization is carried out along the direction of each of the $D-1$ conjugate vectors to obtain a new point $\mathbf{x}_1$. In the second cycle, the maximum $\mathbf{y}_2$ along an estimated tangent to the path connecting the initial state to $\mathbf{y}_1$ to the final state is found, and so on. The process is repeated until the gradient of a maximum $\mathbf{y}_i$ is smaller than a given tolerance.

Ridge method

The idea beyond the ridge method [17] is exploring the ridge separating the two minima, corresponding to the initial and final state, until a minimum is found. It does not require neither the evaluation of the Hessian matrix of the potential nor any guess of the geometry of the transition state. Initially, the maximum $\mathbf{y}_1$ along the vector connecting the initial and the final state is found. Then, two images are taken, one on each side, and moved in cycles of side steps and downhill steps towards the saddle point. This method has the same advantages as the NEB, but its performance is poorer in the final stage, as most of the force evaluations are needed in proximity of the saddle point.

DHS method

This method finds saddle points for unimolecular and bimolecular reactions without prior knowledge of the geometry of the transition state [18]. It also involves two images of the system, starting from the initial and the final state connected by a segment. Each cycle consists of two steps. In the first one, the image with lower energy is pulled towards the one with higher energy along the segment. In the second one, the image with the lower energy is minimized keeping the distance between the two fixed. The process is repeated until the distance between the images is smaller than a given tolerance. This method can quickly locate the neighbouring region of the saddle point, but does not converge efficiently to the saddle point. In fact, as the images approach the saddle point, there is a high probability of both images ending on the same side of the ridge, causing both of them to slip into one of the minima.

Dimer method

This method is remarkable for its ability to find minimum energy paths when the final state is unknown. Typically, methods for the search of the saddle point in this case re-

quire the calculation and diagonalization of the full Hessian matrix [19–24]. The Dimer method [25, 26] only requires first derivatives of the potential and no diagonalization. It involves two replica of the system, that is, the dimer. The force acting on the centre of the dimer, obtained by interpolation of the forces acting on the images, is modified by inverting its component along the direction of the dimer. Then, the force is minimized with respect to orientation and the dimer subsequently translated. This provides the direction of the normal mode of lowest frequency. On landscapes where multiple saddle points are accessible, the dimer method preferably converges to the lowest.

6.3 Nudged Elastic Band

The Nudged Elastic Band (NEB) method was proposed by Henkelman and Jónsson [5] for the search of saddle points and minimum energy paths between known reactants and products. Such method, in principle, requires no prior knowledge of the geometry of the transition state. It also does not require the evaluation of the Hessian matrix. However, it has been proven not only to converge efficiently, but also to be able to locate the *exact* saddle point in its Climbing Image version.

Like the other chain–of–states methods, a string of replicas is initially created and connected with spring forces in order to form a discrete representation of the reaction path. The initial guess images are typically chosen by linear interpolation of the coordinates between the initial and the final state. The replicas are then relaxed along the path until each image converges to the lowest possible energy while maintaining equal spacing to neighbouring images.

An elastic band with N+1 images can be denoted by $\{\mathbf{R_0}, \mathbf{R_1}...\mathbf{R_N}\}$ where $\mathbf{R_0}$ and $\mathbf{R_N}$ are fixed (initial and final state). From an algorithmic point of view, this translates into constructing an object function

$$\mathcal{S}(\mathbf{R_0}, \mathbf{R_1}...\mathbf{R_N}) = \sum_{i=1}^{N-1} E(\mathbf{R}_i) + \sum_{i=1}^{N} \frac{k}{2}[E(\mathbf{R}_i) + E(\mathbf{R}_{i-1})]^2 \tag{6.17}$$

where k is the spring constant.

If we relax such object with respect to the replicas as is, then the method would be subject to "cutting corners", that is, the band tends to be pulled off the MEP in regions where the potential is particularly curved. This can be limited by choosing a weaker spring constant, but in that case the images will tend to slide down towards the minima, giving lower resolution around the saddle point where it is most needed.

Both problems can be solved with nudging, that is, projecting out the component of the force due to the potential perpendicular to the band. In other words, the force on each image only contains the parallel component of the spring force $\mathbf{F}_i^s$ and the perpendicular component of the true force $\nabla E(\mathbf{R_i})$. The total force acting on an image is then:

$$\mathbf{F}_i = \mathbf{F}_i^s \mid_{\parallel} -\nabla E(\mathbf{R_i}) \mid_{\perp} \tag{6.18}$$

where

$$\mathbf{F}_i^s \mid_{\parallel} = k(|\mathbf{R}_{i+1} - \mathbf{R}_i \mid - \mid \mathbf{R}_i - \mathbf{R}_{i-1}|)\hat{\tau}_i \tag{6.19}$$

and

$$\nabla E(\mathbf{R}_i) \mid_{\perp} = \nabla E(\mathbf{R}_i) - \nabla E(\mathbf{R}_i) \cdot \hat{\tau}_{\parallel}\hat{\tau}_{\parallel} \tag{6.20}$$

where k is the spring constant and $\hat{\tau}_i$ is the tangent unit vector at image i.
Notably, among the considered methods, only the NEB and the CPR methods are able to provide not only a saddle point, but a wider view over the general landscape, for example, by being able to locate more than one transition state along a reaction path.

6.3.1 Climbing Image Nudged Elastic Band

The Climbing Image NEB or CI–NEB [27] is an improvement of the NEB method, within which, after a few iterations, the image $\mathrm{i_{max}}$ with the highest energy is identified as the transition state and hence driven up to the saddle point by maximizing its energy along the band while minimizing it in all other directions. When this image converges, it will be at the exact saddle point. The force on this image is not given by Equation 6.18 but rather

$$\mathbf{F_{i_{max}}} = - \bigtriangledown \mathrm{E}(\mathbf{R_{i_{max}}}) + 2 \bigtriangledown \mathrm{E}(\mathbf{R_{i_{max}}}) \mid_{\parallel} , \tag{6.21}$$

that is, the image does not feel the spring forces along the band; instead, the true force acting upon this image along the tangent is inverted. Since the climbing image is not affected by the spring force, the spacing of the neighbouring images on each side of the climbing image will eventually be different.
The advantage with respect to the classic NEB method is that its Climbing Image version converges rigorously to the exact saddle point. This removes completely small errors due to the fact that, in the original NEB method, once the chain of states has converged, the location of the saddle must be obtained by interpolation of the reaction path. This advantage comes with nearly no added computational cost.

6.4 Figures

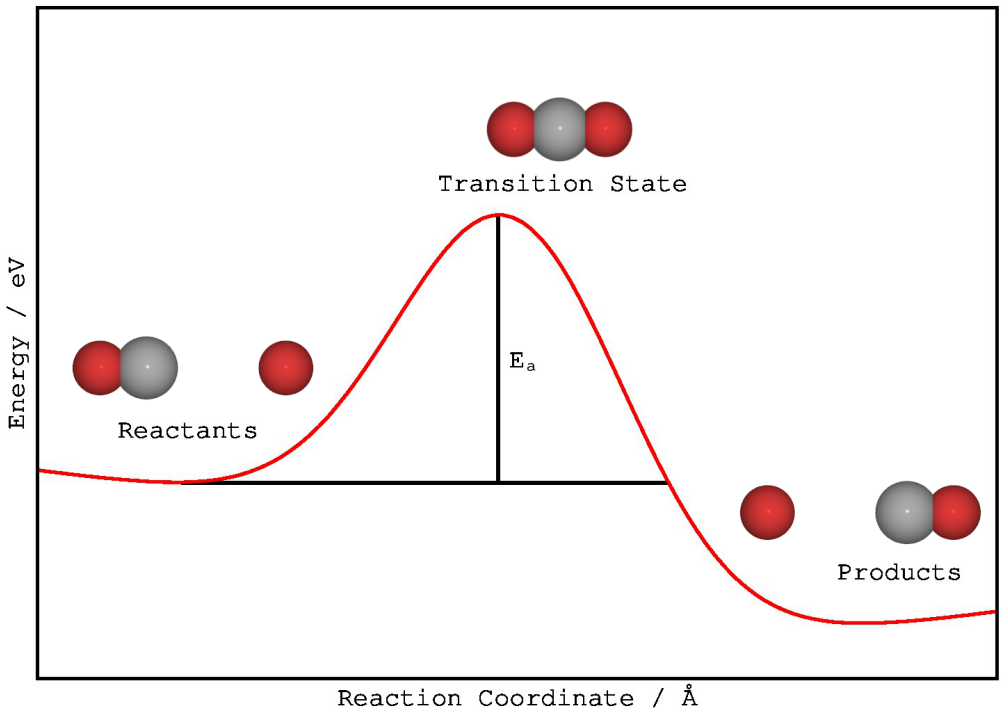

Figure 6.1: Plot of the Minimum Energy Path (MEP) (see Section 6.1) of an arbitrary bimolecular reaction of the type $AB + C \rightleftharpoons A + BC$. E_a is the activation barrier for the reaction (neglecting the Zero Point energy).

REFERENCES

[1] H. Eyring. The activated complex in chemical reactions. *The Journal of Chemical Physics*, 3(2):107, 1935.

[2] M. G. Evans and M. Polanyi. Some applications of the transition state method to the calculation of reaction velocities, especially in solution. *Transactions of the Faraday Society*, 31:875, 1935.

[3] E. Wigner. The transition state method. *Transactions of the Faraday Society*, 34:29, 1938.

[4] G. Henkelman, G. Jóhannesson, and H. Jónsson. Methods for finding saddle points. In *Progress on Theoretical Chemistry and Physics*, chapter 10, pages 269–300. Kluwer Academic Publishers, 2000.

[5] H. Jónsson, G. Mills, and K. W. Jacobsen. Nudged elastic band method for finding minimum energy paths of transitions. In *Classical and Quantum Dynamics in Condensed Phase Simulations*, chapter 16, page 385. World Scientific, 1998.

[6] T. A. Halgren and W. N. Lipscomb. The synchronous–transit method for determining reaction pathways and locating molecular transition states. *Chemical Physics Letters*, 49(2):225 – 232, 1977.

[7] R. P. Feynman and A. R. Hibbs. *Quantum Mechanics and Path Integrals*. McGraw-Hill Companies, 1965.

[8] R. Czerminski and R. Elber. Reaction path study of conformational transitions in flexible systems: applications to peptides. *The Journal of Chemical Physics*, 92(9):5580, 1990.

[9] A. Ulitsky and R. Elber. A new technique to calculate steepest descent paths in flexible polyatomic systems. *The Journal of Chemical Physics*, 92(2):1510, 1990.

[10] C. Choi and R. Elber. Reaction path study of helix formation in tetrapeptides: effect of side chains. *The Journal of Chemical Physics*, 94(1):751, 1991.

[11] E. M. Sevick, A. T. Bell, and D. N. Theodorou. A chain of states method for investigating infrequent event processes occurring in multistate, multidimensional systems. *The Journal of Chemical Physics*, 98(4):3196, 1993.

[12] R. E. Gillilan and K. R. Wilson. Shadowing, rare events, and rubber bands. A variational Verlet algorithm for molecular dynamics. *The Journal of Chemical Physics*, 97(3):1757, 1992.

[13] R. Czerminski and R. Elber. Self–avoiding walk between two fixed points as a tool to calculate reaction paths in large molecular systems. *International Journal of Quantum Chemistry*, 38(S24):167–185, March 1990.

[14] R. Elber and M. Karplus. A method for determining reaction paths in large molecules: application to myoglobin. *Chemical Physics Letters*, 139(5):375–380, January 1987.

[15] O. S. Smart. A new method to calculate reaction paths for conformation transitions of large molecules. *Chemical Physics Letters*, 222(5):503–512, May 1994.

[16] S. Fischer and M. Karplus. Conjugate peak refinement: an algorithm for finding reaction paths and accurate transition states in systems with many degrees of freedom. *Chemical Physics Letters*, 194(3):252–261, June 1992.

[17] I. V. Ionova and E. A. Carter. Ridge method for finding saddle points on potential energy surfaces. *The Journal of Chemical Physics*, 98(8):6377, 1993.

[18] M. J. S. Dewar, E. F. Healy, and J. J. P. Stewart. Location of transition states in reaction mechanisms. *Journal of the Chemical Society, Faraday Transactions 2*, 80(3):227, 1984.

[19] C. J. Cerjan and W. H. Miller. On finding transition states. *The Journal of Chemical Physics*, 75(6):2800, 1981.

[20] D. T. Nguyen and D. A. Case. On finding stationary states on large–molecule potential energy surfaces. *The Journal of Physical Chemistry*, 89(19):4020–4026, September 1985.

[21] W. Quapp. A gradient–only algorithm for tracing a reaction path uphill to the saddle of a potential energy surface. *Chemical Physics Letters*, 253(3-4):286–292, May 1996.

[22] H. Taylor and J. Simons. Imposition of geometrical constraints on potential energy surface walking procedures. *The Journal of Physical Chemistry*, 89(4):684–688, February 1985.

[23] J. Baker. An algorithm for the location of transition states. *Journal of Computational Chemistry*, 7(4):385–395, August 1986.

[24] D. J. Wales. Finding saddle points for clusters. *The Journal of Chemical Physics*, 91(11):7002, 1989.

[25] G. Henkelman and H. Jónsson. A dimer method for finding saddle points on high dimensional potential surfaces using only first derivatives. *The Journal of Chemical Physics*, 111(15):7010, 1999.

[26] J. Kastner and P. Sherwood. Superlinearly converging dimer method for transition state search. *The Journal of Chemical Physics*, 128(1):014106, 2008.

[27] G. Henkelman, B. P. Uberuaga, and H. Jónsson. A climbing image nudged elastic band method for finding saddle points and minimum energy paths. *The Journal of Chemical Physics*, 113(22):9901, 2000.

Part III

Results

Chapter 7

1–chloropentane on Si(001)

As summarized in Chapter 2, halogenated hydrocarbons have been shown to be an ideal candidate for surface patterning by means of a two–step process: (1) a self–assembly of physisorbed patterns followed by (2) a localized reaction to chemically imprint the halogens leaving the pattern substantially unchanged. 1–chloropentane (from now on often referred to as CP in the text) belongs to the class of molecular templates able to achieve surface patterning and has been the subject of experimental studies by J. Polanyi's group at University of Toronto [1, 2], supported by theoretical calculations performed in our group. It will be therefore extensively treated in the present Chapter. 1–chloropentane physisorbs on Si(001)–2×1 at room temperature as self–assembled lines. The physisorbed lines consist of pairs that grow perpendicularly to the silicon dimer rows. Pairs can physisorb in two distinct configurations, one asymmetric (A) and one symmetric (S), differing only in the curvature of one pentane tail, as shown in Figure 7.1. Chemical reaction was triggered using three different modes of energization: heat, electrons or light. In all cases, physisorbed CP molecules undergo localized atomic reaction resulting in chemisorbed lines of Cl pairs.
Pairwise adsorption of other haloalkanes and dipole–directed self assembly at silicon surfaces were previously reported at [3–5].

7.1 Experiments

7.1.1 Materials and methods

Experiments were performed in a UVH STM at base pressure of 5×10^{-11} Torr. Images were taken in constant current mode with a tunneling current of 0.2 nA. The substrate is a n–type phosphorous–doped silicon sample of 0.01-0.02 Ωcm and 250±25 μm thickness. The STM images of the surface shows a 2×1 reconstruction with $< 0.2\%$ defects.
The adsorbate was cleaned by repeated freeze–pump–thaw cycles and dosed through a leak valve.
The electron–induced reaction was studied with two methods. The reaction threshold was determined positioning the STM tip over the centre of a CP pair maintaining the

current at 0.2 nA until reaction occurred. In order to chemically imprint the Cl atoms, repeated scans were performed at a bias voltage of 1.6 V.
For thermal reaction, CP molecules were dosed at 325 K. The chosen temperature is such that thermal desorption of CP–pairs is negligible. 113 terminal A pairs and 105 middle S pairs were observed using sequential imaging with non–uniform intervals for a period of 230 minutes.
The photo–induced reaction was achieved by illumination at 308 nm with a XeCl excimer laser.

7.1.2 Results

The reagent 1–chloropentane was deposited on Si(001)–2×1 at room temperature [1, 2]. At low coverage (0.004/0.007 L), STM imaging shows that CP physisorbed exclusively as isolated CP–pairs or lines of CP–pairs.

Geometries

CP–pairs physisorb on Si(001)–2×1 in two distinct stereoisomeric configurations, symmetric (S) and asymmetric (A), differing only in the curvature of one pentane tail, as illustrated in Figure 7.1. Each CP–pair has its chlorine atoms positioned above the silicon atoms of a single dimer at the centre of three covered silicon dimers. Both asymmetric and symmetric configurations of CP–pairs have been observed in isolation. Figure 7.1 also shows lines of CP–pairs. When self–assembled in a line, the head of the line consists, in the large majority of cases, of an asymmetric unit, while the body of the line is always formed by a variable number of symmetric units. Surprisingly, the symmetry difference renders the rate of thermal reaction of A 15 times greater than that of S, that is, the stereoisomerism of the reagent has a dramatic effect on surface reactivity. Correspondingly, for electron–induced reaction, the energy threshold for A is 1 eV smaller than that for S.
The two isolated pairs have been observed to interconvert thermally. The switching is clearly visible in STM images as an adjacent silicon atom (the "perturbed spot" also observed at [4, 5]) changes from bright (A state) to dark (S state), as shown in Figure 7.1.
The two configurations also differ by the local buckling of the neighbouring silicon dimers. For A, physisorption locally pins the surface in a c(4×2) reconstruction. Also, the silicon dimer in the adjacent dimer row is buckled in the sense that the closest silicon atom is up and bright. Conversely, for S, physisorption locally pins the surface in a p(2×2) reconstruction, and the silicon dimer in the adjacent dimer row is buckled in the sense that the farthest silicon atom is up and less bright than in the former case. The perturbation is only observed on one side of the CP–pair.
In isolation, A and S are found in equal proportion, suggesting comparable adsorption

energies. Moreover, reversible A⇋S thermal switching was observed, with a room temperature rate of $5 \times 10^{-2}\,\mathrm{s}^{-1}$, corresponding to a thermal activation energy of 0.8 ± 0.1 eV according to the Arrhenius equation

$$k = A \exp\left(-E_a/k_b T\right) \tag{7.1}$$

assuming a pre–exponential factor between 10^{11} and 10^{15} s^{-1}.

Thermal Reaction

Similarly to 1–fluoropentane pairs [5], and regardless of the energization method used, the reaction of 1–chloropentane pairs on Si(001)–2×1 is cooperative, always yielding pairs of chemically imprinted chlorine atoms attached to the two silicon atoms of the underlying silicon dimer. The cooperative reaction occurs in two steps, where the rate–determining stage is the transfer of the first Cl atom to the surface. The second Cl atom attaches to the subsequently formed Si dangling bond in a barrierless reaction.
Figure 7.2 shows a logarithmic plot of the fractional survival of unreacted S and A pairs over time at 325 K. Using Arrhenius equation and assuming a pre–exponential factor between 10^{11} and 10^{15} s^{-1}, the activation energies are estimated as 1.07 eV and 1.14 eV for A and S respectively, with a relative uncertainty of 4 meV and an absolute uncertainty of 0.13 eV (see Appendix B).
For A pairs, the reaction was monitored in isolation, at the end of line farthest from the buckling, and at the end of line closer to the buckling. In all three cases the rate remained the same, that is, the presence of a neighbouring S pair does not affect the reactivity of the A pair. The electron–induced reaction will be described in Appendix B, while details for the photo–induced reaction can be found at [1].

7.2 Theory

The level of theory used in this work is known to yield accurate adsorption geometries, and energetic, but is also known to be insufficient to recover the phenomena of buckling which is evident in the experimental images. Previous work on pairs of 1–fluoropentane [5] molecules was able to recover this surface buckling, but to do so required that the system was reduced to a 1×6 super-cell and the molecules to fluoromethane. For this reduced system DFT simulations were performed at the hybrid level using the HSE03 [6] hybrid functional implemented in VASP [7, 8], including a dopant phosphorus atom in the supercell. In this simulation, the image became brighter at the buckled site, B, due to local charging. The high cost of these calculations make them impractical for the simulation of large systems using currently available computers.

7.2.1 Theoretical setup

All *Ab–initio* calculations were performed using the Vienna Ab–initio Simulation Package (VASP) [7, 8] installed at the SciNet supercomputer [9]. Using VASP 5.2.11, the ground state electronic structure of A and S CP pairs on Si(001)–2×1 was simulated with ultrasoft pseudopotentials [10] (without van der Waals corrections) or Projected Augmented Wave [11, 12] PBE functionals [13, 14] (with van der Waals corrections). The dispersion was calculated using the semi–empirical DFT–D method of Grimme [15], as implemented in VASP (see Appendix A). Accounting for boundary conditions of buckled dimer rows the surface was mimicked by a 8×6 supercell for A and a 6×6 supercell for S. The Si(001) slab contained 8 layers, the bottom of which was passivated with hydrogen. The high number of layers was necessary to mimic the high elasticity of the silicon lattice. Due to the sufficiently large number of surface atoms, the Brillouin zone was sampled using the Γ point only. The molecular adsorption sites were determined by placing the bent molecules about 3 Å above the surface plane, with the molecular backbone parallel to the surface. The molecule and the four uppermost surface layers were then fully relaxed with a Quasi–Newton optimizer [16] until the forces on individual ions were less than 0.02 eV/Å.

7.2.2 Results

Geometries

Two stable configurations of CP–pairs were found, A and S, in accordance with the experimental observations as described in Section 7.1.2. Table 7.1 gives the distances between the Cl atoms of each chloropentane molecule and the silicon atom beneath.
It is the Cl atom closest to the surface that reacts in the rate determining step. This is also the Cl atom that is closest to the buckled dimer. As can be seen, the difference between the distance between adjacent Cl atoms and underlying Si atoms for A and S varies by less than 0.05 Å.

Adsorption energies

Adsorption energies were calculated for both A and S on both the Si(001)–c(4×2) and Si(001)–p(2×2) surfaces. In the absence of adsorbate the energy of the two surface configurations is known to be almost identical, c(4×2) being slightly favoured. The molecular physisorption actually occurs at the dynamically flipping surfaces of Si(001)–2×1, and physisorption of a CP pair results in the local pinning of some five or six silicon dimers close to the adsorbates. Close to the A adsorbate silicon-dimers are pinned in the c(4×2) configuration, whereas close to the S adsorbate silicon dimers are pinned in the p(2×2) configuration (as highlighted in Table 7.2).
The calculated adsorption energies were surface dependent in the absence of van der

Waals corrections. With van der Waals corrections, the physisorption energies of the A pair and S pair are found to be within 30 meV of one another, in good agreement with experiment. In other words, the choice of the correct local pinning of the silicon surface correctly yields equal adsorption energies.

Energy barriers

Calculation of energy barriers to A⇌S switching were made using the Climbing Image Nudged Elastic Band method [17], as described in Chapter 6 and included semi–empirical corrections for dispersion interactions using the method of Grimme [15], as implemented in VASP 5.2.11.

The process to be modelled, A⇌S switching, occurs on a Si(100)–2×1 surface, in which only dimers close to the adsorbate are pinned. All calculations were made with periodic boundary conditions, and therefore required a supercell with a repeating surface symmetry.

Since we cannot simultaneously accommodate the differing surface symmetries that apply to A and S, we made an estimate of the energy barrier as follows. We first calculated the minimum energy path for A⇌S on a p(2×2) symmetry surface. The resulting energy barrier was around 0.2 eV. Next, we allowed for the additional energy required by dimer flipping by adding 0.1 eV / Si–dimer [18]. We therefore estimate the total energy barrier for A⇌S (including the flipping of five adjacent silicon dimers) as 0.7 eV. This constitutes a rough upper estimate of the theoretical energy barrier for A⇌S, including the motion of the substrate, since cooperative effects could lower the total energy barrier.

Simulated STM images

The experimental STM images shown in Figure 7.3 were obtained at a surface bias of −1.5 V and with a tunneling current of 0.2 nA. Simulated STM images were generated, using the same −1.5 V surface bias, from the electronic structure of the fully relaxed systems by plotting isodensity contours. The value of the electron density of states was adjusted so that the distance of the contour from the silicon surface dimers was held constant at about 6 Å, which corresponds to the set distance to the surface under the experimental tunneling conditions. Images were simulated using the Tersoff–Hamann approach [20, 21], as described in Chapter 5 and implemented in BSKAN [19]. Simulated and experimental images are compared below in Figure 7.3. The simulated images fail to reproduce the experimental observations in detail because, *inter alia*, the calculations do not recover the "buckled dimer", which is adjacent to the A and S configurations, and therefore do not recover the brightness in the experimental images which is at one side of the CP pair (at left, as shown), on a silicon dimer row adjacent to the adsorbates. In Figure 7.3 the positions at which the brightness appears in the

STM images due to the buckled dimer is indicated by a white dot on the lower set of images of each panel. The images were calculated using an 8×6 supercell for A and a 6×6 supercell for S. The images have been tiled in the figure. The geometry of the substrates is shown, fading from right to left.

7.3 Conclusions

We report the existence and structure of two different stereoisomers of 1–chloropentane (CP) pairs at a Si(001)–2×1 surface; asymmetric (A) and symmetric (S). These two configurations, differing in the direction of curvature of one pentane tail, show remarkably different reactivities in surface chlorination. The A pair, both in a line of CP–pairs or in isolation, is found to be fifteen times more reactive at room temperature than the S pair. A further marked difference in reactivity in the same sense (A more reactive than S) was found for electron–induced reaction; the A stereoisomer exhibited a threshold for reaction 1 eV less than the S stereoisomer.
DFT calculations correctly explain and reproduce the energetics of the system, showing that, matching the correct local surface buckling to the corresponding adsorbed geometry, the two stereoisomers have roughly the same adsorption energies. However, the level of theory used is not capable of fully recovering some details, such as the existence of "perturbed spots", which would be visible in the STM simulations only with the employment of hybrid functionals.

7.4 Figures and tables

System	Geometry on Si(001)–p(2×2)		Geometry on Si(001)–c(4×2)	
	$Si–Cl_{far}$ / Å	$Si–Cl_{far}$ / Å	$Si–Cl_{far}$ / Å	$Si–Cl_{far}$ / Å
A pair	–	–	5.23	2.47
S pair	4.44	2.44	–	–

Table 7.1: Si–Cl bond lengths for the A pair and the S pair. The bond lengths shown here were calculated with Grimme's semiempirical correction for the van der Waals attraction, on the correct surface symmetry for each.

System	E_{ads} on Si(001)–p(2×2) / eV		E_{ads} on Si(001)–c(4×2) / eV	
	with vdW	without vdW	with vdW	without vdW
A pair	**1.20**	0.63	1.29	0.55
S pair	1.19	0.55	**1.23**	0.42

Table 7.2: Computed physisorption energies of the A pair and the S pair on both reconstructions of Si(001). Calculations of physisorption geometries and energies were performed with and without Grimme's semiempirical correction for the van der Waals interaction. The error of integration is believed to be ∼0.01 eV. Bold entries correspond to the best calculation for the correct surface geometry.

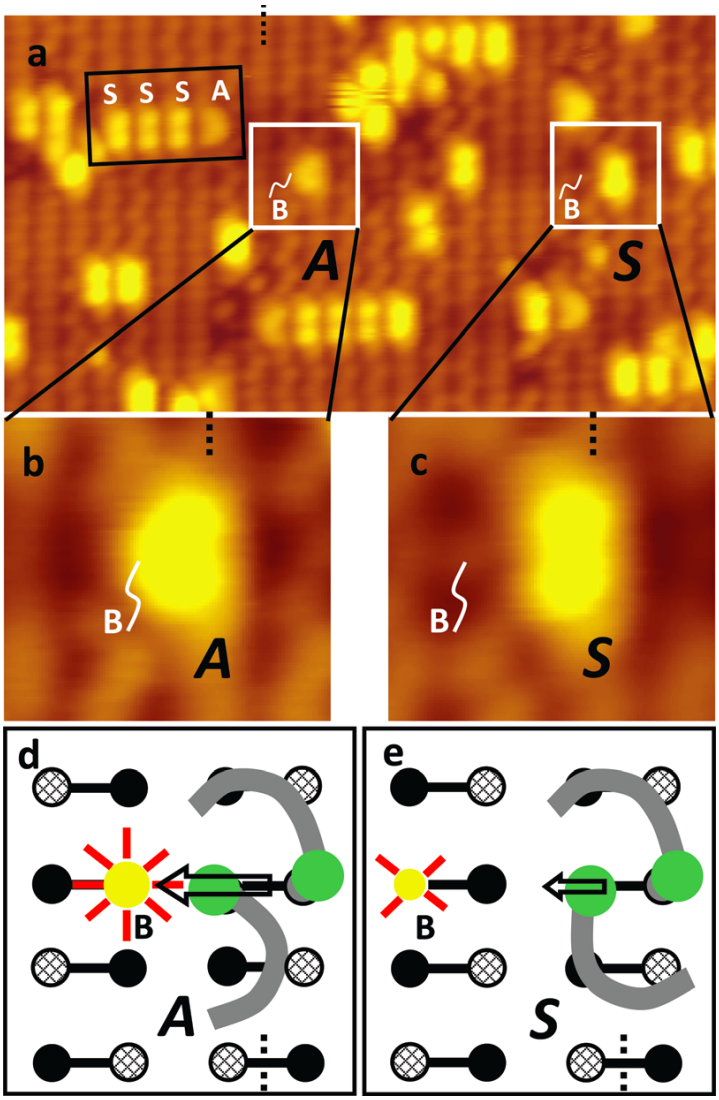

Figure 7.1: Self–assembled 1–chloropentane lines and two stereoisomers at Si(001)–2×1. (a) Filled state STM image (300 K, $V_{surf} = -1.5$ V, $I_t = 0.2$ nA, 180×90 Å^2) of a Si(001)–2×1 surface exposed to 0.3 L of CP. The dotted vertical lines indicate the centres of the dimer rows. CP–pairs are observed in isolation (in white squares) and lines (in dark rectangles). Two stereoisomers of CP–pairs are found: asymmetric (A) and symmetric (S). (b), (c) Close–ups (25×25 Å^2) of A and S pairs. The features marked "B" are the buckled dimers ("perturbed spots"). (d), (e) Schematic structures of A and S. In A, the two Si dimer rows are locally buckled in a c(4×2) reconstruction (zig–zag rows opposite to each other), whereas, in S, the neighbouring Si dimer rows are locally buckled in a p(2×2) reconstruction (zig–zag rows in the same direction). Silicon "up" atoms are represented by hatched circles, while "down" atoms are represented as black filled circles. The arrows in (d) and (e) indicate the adsorbate dipoles. Chlorine atoms are coloured green and the hydrocarbon chain is coloured gray. Red rays highlight the perturbed spot.

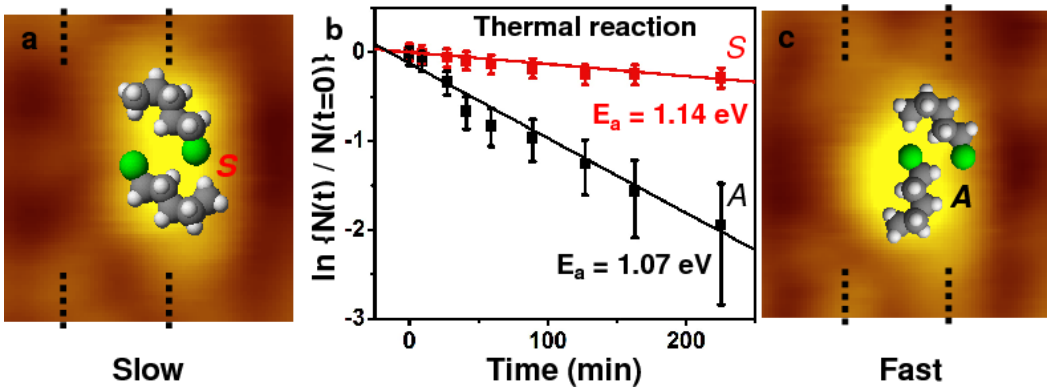

Figure 7.2: Thermal reaction of S and A physisorbed CP pairs in a line. Panels (a) and (c) show STM images overlaid by schematic structures. Dashed lines marke the centres of silicon dimer rows. (b) Plot of logarithm of fractional survival os 105 S pairs (red) and 101 A pairs (black) against time at 325 K.

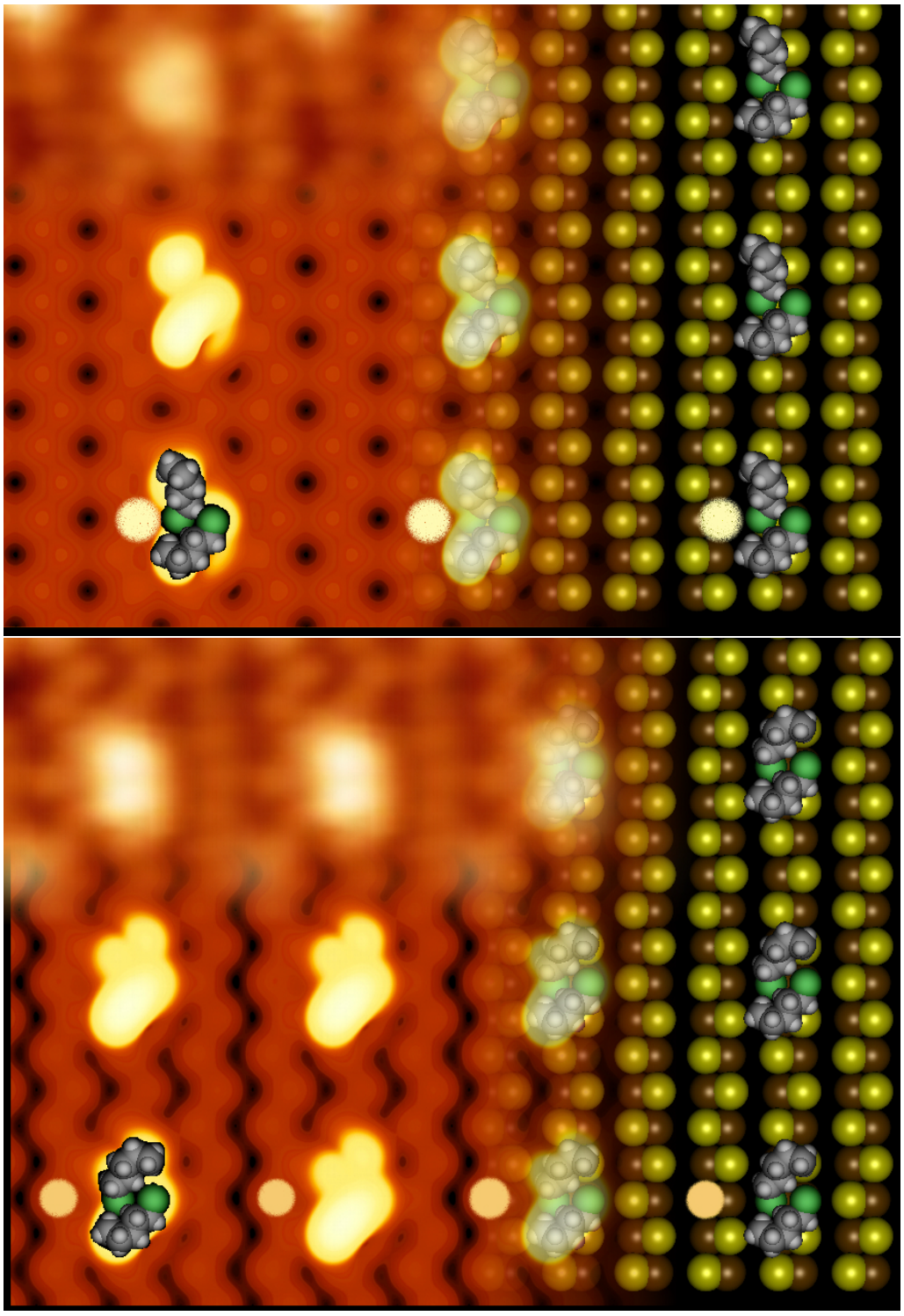

Figure 7.3: Simulated and experimental STM images of an A pair (top) and a S pair (bottom) on Si(001)–c(4×2). Experiment and simulation were obtained using a voltage bias of 1.5 V. Top row: experimental image (tiled). Middle row: simulated image (tiled). Bottom row: Simulated image (tiled) with the position of the buckled dimer indicated by white circles. All images are overlaid onto the surface used for the simulations. The images are faded to the right to show the computed surface geometry. Atoms are shown with van der Waals radii. Si "up" atoms yellow, Si "down" atoms brown, Cl atoms green, C atoms grey, H atoms white.

REFERENCES

[1] K. R. Harikumar, I. R. McNab, J. C. Polanyi, A. Zabet-Khosousi, and W. A. Hofer. Imprinting self–assembled patterns of lines at a semiconductor surface, using heat, light, or electrons. *Proceedings of the National Academy of Sciences of the United States of America*, 108(3):950–5, January 2011.

[2] K. R. Harikumar, I. R. McNab, J. C. Polanyi, A. Zabet-Khosousi, C. Panosetti, and W. A. Hofer. Stereo–isomerism controls surface reactivity: 1–chloropentane–pairs on Si(100)–2×1. *Chemical Communications*, 47(44):12101–3, November 2011.

[3] S. Dobrin, K. R. Harikumar, Jones. R. V., N. Li, I. R. McNab, J. C. Polanyi, P. A. Sloan, Z. Waqar, J. S. Y. Yang, S. Ayissi, and W. A. Hofer. Self–assembled molecular corrals on a semiconductor surface. *Surface Science*, 600(5):43 – 47, 2006.

[4] K. R. Harikumar, T. Lim, I. R. McNab, J. C. Polanyi, L. Zotti, S. Ayissi, and W. A. Hofer. Dipole–directed assembly of lines of 1,5–dichloropentane on silicon substrates by displacement of surface charge. *Nature nanotechnology*, 3(4):222–8, April 2008.

[5] K. R. Harikumar, L. Leung, I. R McNab, J. C. Polanyi, H. Lin, and W. A. Hofer. Cooperative molecular dynamics in surface reactions. *Nature chemistry*, 1(9):716–21, December 2009.

[6] J. Heyd, G. E. Scuseria, and M. Ernzerhof. Hybrid functionals based on a screened Coulomb potential. *The Journal of Chemical Physics*, 118(18):8207, 2003.

[7] G. Kresse and J. Furthmüller. Efficiency of ab–initio total energy calculations for metals and semiconductors using a plane–wave basis set. *Computational Materials Science*, 6(1):15–50, 1996.

[8] G. Kresse and J. Furthmüller. Efficient iterative schemes for *ab initio* total–energy calculations using a plane–wave basis set. *Physical Review B*, 54:11169–11186, 1996.

[9] J. Dursi, L. Groer, D. Gruner, C. Loken, S. Northrup, S. Ross, R. Sobie, and C. Yip. High performance computing symposium (hpcs2010). *Journal of Physics: Conference Series*, 256(1):011001, 2010.

[10] D. Vanderbilt. Soft self–consistent pseudopotentials in a generalized eigenvalue formalism. *Physical Review B*, 41:7892–7895, Apr 1990.

[11] P. E. Blöchl. Projector augmented–wave method. *Phys. Rev. B*, 50:17953–17979, 1994.

[12] G. Kresse and D. Joubert. From ultrasoft pseudopotentials to the projector augmented–wave method. *Physical Review B*, 59:1758–1775, 1999.

[13] J. P. Perdew, K. Burke, and M. Ernzerhof. Generalized gradient approximation made simple. *Physical Review Letters*, 77:3865, 1996.

[14] J. P. Perdew, K. Burke, and M. Ernzerhof. Erratum: Generalized gradient approximation made simple. *Physical Review Letters*, 78:1396, 1997.

[15] S. Grimme. Semiempirical gga–type density functional constructed with a long–range dispersion correction. *Journal of Computational Chemistry*, 27(15):1787–1799, 2006.

[16] P. Pulay. Convergence acceleration of iterative sequences. the case of scf iteration. *Chemical Physics Letters*, 73(2):393–398, 1980.

[17] G. Henkelman, B. P. Uberuaga, and H. Jönsson. A climbing image nudged elastic band method for finding saddle points and minimum energy paths. *The Journal of Chemical Physics*, 113(22):9901, 2000.

[18] J. H. Cho and H. Kang, M. Atomic structure of the sb/si(100)–(2×) surface. *Phys. Rev. B*, 51:5058–5060, Feb 1995.

[19] W. A. Hofer, A. J. Fisher, G. P. Lopinski, and R. A. Wolkow. Adsorption of benzene on Si(100)–(2×1): Adsorption energies and STM image analysis by *ab initio* methods. *Physical Review B*, 63:085314, Feb 2001.

[20] J. Tersoff and D. R. Hamann. Theory of the scanning tunneling microscope. *Physical Review B*, 31:805–813, 1985.

[21] J. Tersoff and D. R. Hamann. Theory and application for the scanning tunneling microscope. *Physical Review Letters*, 50:1998–2001, 1983.

Chapter 8

Meta–diiodobenzene on Cu(110)

8.1 Introduction

In recent years, the adsorption of aromatic, organic and halo–organic compounds on metal and semi–conductor surfaces has been a subject of growing interest in the field of Surface Science. Small molecules such as substituted and unsubstituted hydrocarbons and benzenes have been shown to be able to adsorb, self–assemble and react on surfaces such as Si(100), Si(111) [1], Al(111), Pt(111), Cu(110) [2] opening a wide range of possibilities in the manufacturing of nanodevices such as catalysts, biosensors, chemosensors, nanocircuits, molecular machines; small molecules can also act as a template for the engineering of more complex structures [3]. Both experimental and theoretical effort has been made in understanding the energetics and reactivity of such systems [4–8].
In the present Chapter, we will focus on the theoretical modelling of the adsorption of 1,3–diiodobenzene (from now on referred to as meta–diiodobenzene or m–DIB) on Cu(110) by means of Density Funcional Theory as implemented in VASP 5.2.11 [9, 10] and STM imaging with the Tersoff–Hamann approach [11, 12]. A similar system, that is, 1,4–diiodobenzene (para–diiodobenzene or p–DIB), has been proven to be able to act as a molecular caliper, as the cleavage of the terminal C–I bonds of physisorbed monomers and polymers can be triggered by means of an STM tip resulting in highly site–specific attachment of I atoms on a Cu(110) surface [13]. We believe that the meta isomer may show an analogous behaviour; therefore one could, in principle, tune the Iodine–Iodine distance by controlling the number and type of molecules physisorbed on the surface and subsequently inducing localized reaction using the STM tip.
Considering that, as proven in the references above, the outcome of halogenated hydrocarbon reactions on metal and semiconductor surfaces can be easily controlled at the nanoscale, the present work is intended to be a ground study within the more general question of whether the surface reactivity of Cu(110) can be locally changed by site–specific functionalization such as the imprinting of individual atoms and clusters. Cu(110) itself is fairly easy to model theoretically, but it is smooth and not too reactive, hence, for instance, not catalytic. Physisorbed molecules tend to diffuse across

the surface, but localized chemical imprinting of atoms such as halogens, carbon, oxygen or sulphur may act as an anchor for the formation of Cu–atom–Cu clusters which could increase the surface reactivity similarly to Au/TiO_2 catalysts [14]. In particular, halo–hydrocarbons are a good template for atomic imprinting on both semiconductors and metal surfaces as the C–X bond cleavage is easily accomplished via thermal and/or photo–induced and/or electron–induced reaction [2, 5–7, 13, 15–17].
A theoretical treatment can serve as a basis to provide guidance to experimentalists interested in investigating the physisorption and reactivity properties of this and similar molecules by means of STM imaging and manipulation.

8.2 Theory

8.2.1 Density functional Theory

Density Functional Theory (DFT) [18, 19] as implemented in VASP 5.2.11 [9, 10] was employed as the core of all the calculations carried out in the present work, that is, to relax the physisorbed configurations, compute the corresponding adsorption energies and electronic properties, and then, for the chosen structures and by means of single point calculations, obtain charge isodensities to be used as an input to produce simulated STM images.

Theoretical setup

Throughout all the calculations, we employed Generalized Gradient Approximation potentials developed by Perdew–Burke–Ernzerhof (GGA–PBE potentials) [20, 21] in conjunction with the projected augmented wave approach for core electrons [22, 23]; the Brillouin zone was sampled using a 3×3×1 K–point mesh (3×3×3 for bulk calculations, see Section 8.3.1). The cutoff energy, which determines the size of the plane wave basis expansion, was set to 400 eV. The SCF convergence criterion was set to 10^{-4} eV. Where needed, structural minimization was accomplished by means of the Quasi–Newton algorithm [24] including van der Waals dispersion correction using Grimme's method [25]. The structural minimization was carried out until the forces acting on each nucleus were < 0.02 eV/Å, starting with the molecules parallel to and 3 Å above the surface and allowing the molecular degrees of freedom to relax together with the two uppermost layers of the Cu slab, while the bottom Copper layers were kept frozen. The clean surface was generated using the python–based ASE package [26], as a slab of 4×3 Cu atoms and 4 layers with a computationally optimized lattice constant (see Section 8.3.1) and adding 16 Å of vacuum. The chosen supercell corresponds to a coverage of $1.53 \cdot 10^{-8}$ mol/cm^2 , corresponding to 1/12 molecules per Cu atom.
The overall theoretical setup was considered appropriate without performing preliminary convergence checks, as identical settings have already been proven to give satis-

factory results in published works about analogous systems (see, for example, [13]).

8.2.2 Tersoff–Hamann approach to STM simulations

In the Tersoff–Hamann approach, STM tunneling is modeled between a crystal surface and a model probe tip whose shape is arbitrary, but is assumed to consist locally of a simple spherically symmetric electronic state. The tip scans the surface in two dimensions and its height is adjusted in order to mantain a constant tunneling resistance, resulting in a map of the electron density of the sample. Provided that the approximations hold, this model has the advantage of producing quantitative models of STM experiments and realistic images with no need to account for the electronic details and structure of the tip. A full exposition of the method can be found in [11, 12] and Chapter 5.

8.3 Results and Discussion

8.3.1 Clean surface

Lattice constant optimization

Before approaching the study of the surface–adsorbate system, we optimized the lattice constant for bulk Cu within the chosen theoretical model. This was accomplished by performing several single–point calculations of the bulk at different values of the lattice parameter. The resulting plot of the electronic energy vs lattice constant was fitted to a parabola whose minimum represents the optimal lattice constant for the chosen theoretical framework. We hence obtain a = 3.576 Å. It is known that the, generally, LDA approximation leads to an underestimation of the real (experimental) lattice constant, while the GGA approximation gives a larger lattice constant [27]. Nevertheless, this result is valid only when van der Waals correction is not included in the calculation. We find that, despite the employment of GGA–based paw–PBE functionals, the lattice constant is actually slightly underestimated, but still consistent with computed values ranging between 3.522 Å and 3.632 Å [27] and satisfyingly close to the experimental value of 3.615 Å [28].

Structural details of clean Cu(110)

Employing this optimized lattice constant, we have generated the clean Cu(110) supercell as described in Section 8.2.1 and we have relaxed the two uppermost layers, keeping the bottom layers frozen. We hence obtain a 10.72×10.11 Å supercell consisting of 3 rows of 4 Cu atoms parallel to the [1$\underline{1}$0] direction. The spacing between the rows is equal to the lattice constant, while the linear size of m–DIB is around 6 Å, hence an adsorbed m–DIB molecule will typically span over two rows. There are 5 possible adsorption sites:

1. **top**: centred over one of the uppermost Cu atoms;

2. **4–fold hollow**: centred between four adjacent uppermost Cu atoms, *i.e.* centred over one of the Cu atoms in the ridge between two rows;

3. **short bridge**: centred between two adjacent uppermost Cu atoms belonging to the same [1$\underline{1}$0] row;

4. **long bridge**: centred between two adjacent uppermost Cu atoms belonging to adjacent [1$\underline{1}$0] rows;

5. **asymmetric**: centred between teo uppermost Cu atoms belonging to the same [1$\underline{1}$0] row and a Cu atom in the ridge.

The adsorption sites are shown in Figure 8.1.

8.3.2 Adsorption configurations and energies

Initial guesses: possible adsorption arrangements

Similar to and consistent with a previous work on benzene, fluorobenzene and meta–difluorobenzene by L. Zotti *et al.* [29], we built the initial guesses for all the possible physisorbed configurations as shown in Figure 8.1. To clarify the nomenclature, consider the analogous physisorption arrangements of unsubstituted benzene. The configurations labeled with A are the ones for which one of the C_2'' axes of benzene lies along the [001] direction of the Cu surface, *i.e.* across rows, while the configurations labeled with B are the ones for which one of the C_2' axes lies along the [001] direction (or, equivalently, one of the C_2'' axes lies along the [1$\underline{1}$0] direction, *i.e.* along rows), as illustrated in Figure 8.1. Numbers from 1 to 5 mark the adsorption sites, assuming the adsorption centre to coincide with the centre of the benzene ring. The first four represent the positions with the highest symmetry, namely, from 1 to 4: top, 4–fold hollow, short bridge, long bridge. Also, one position with lower symmetry (number 5) was included. The labels x and y are used to distinguish the orientation of the substituted rings as shown in Figure 8.1.
In addition to these twenty configurations, we also took into account the additional configurations obtained from reflection of the A5 and B5 structures with respect to the [1$\underline{1}$0] surface axis, the latter not being symmetric upon such operation, differently from all the other configurations. These structures are denoted as A5x*, A5y* and B5y*. Note that the B5x* and B5x are equivalent. We then compared the adsorption energies and structures of all the 23 possible adsorption arrangements.

Computed adsorption energies

The adsorption energies obtained after structural optimization are reported in Table 8.1. All the adsorption energies are fairly large, around 2 eV. We may *a priori*

infer that the molecules are physisorbed as we expect most of the adsorption energy to be ascribable to the van der Waals binding energy. To support this assumption, we have estimated the dispersion contribution to the adsorption energy for every configuration by performing a single point energy calculation without including the dispersion correction and keeping all the coordinates fixed, then subtracting the result to the vdW–corrected adsorption energy, obtaining a fair approximation of the van der Waals binding energy. The results are shown in Table 8.2; the average van der Waals binding energy is 1.685 eV and, not including dispersion forces, the adsorption energies all decrease to below 0.5 eV, which is consistent with any physisorption scenario found in literature; hence we may conclude that the molecules are indeed physisorbed and not chemisorbed. However, since in the converged structures some distances, *e.g.* between I atoms and the underlying Cu atoms, are smaller than the sum of their van der Waals radii, further investigation is required to remove any doubt. The analysis of the electronic properties, *i.e.* Density of States and partial charges, can help to unambiguously exclude the possibility of chemisorption. The results are presented in Section 8.3.4.

Prediction of experimentally observed populations

The energies are all of the same order of magnitude; however, an estimate of the relative probabilities of experimentally observing one arrangement or another can be made using Boltzmann's equation

$$N_\alpha / N_{\text{ref}} = \exp\left(-\frac{\Delta E_{\text{ads}}}{kT}\right) \tag{8.1}$$

where N_α is the population of the configuration α and N_{ref} is a reference population, wich we shall choose as that of the most stable configuration. Applying Equation 8.1 to the case of the four most and the least stable configurations, at three easily accessible experimental temperatures, that is, liquid He (4.22 K), liquid N_2 (77.0 K) and room temperature (298.0 K), we calculate that, while at high temperatures relative populations of configurations with similar energy tend to the same order of magnitude, at low temperatures a strong preference for the two most stable adsorption arrangements is expected, as shown in Table 8.3. We may note that B5x and B3x have comparable probabilities even at low temperatures; thus we cannot, within the accuracy of the method, unambiguously decide which one of the two is the most stable. It will become clear later that the latter constitute, in fact, a bistable system.

Structural properties

The asymmetric configurations are generally favoured. Some of the configurations appear tilted with respect to the surface. The dihedral angle Θ between the average plane of the ring and the surface is reported in Table 8.1. We chose the four most stable configurations (A5x*, A5y, B3x, B5x, shown in Figure 8.2) to investigate in more detail. These are the only four configurations with adsorption energies larger

than 2.15 eV. Among these, only B3x is flat with respect to the surface, while A5x*, A5y and B5x appear tilted by a small angle. Essential structural details of the four most stable physisorbed orientations compared to that of the m–DIB in vacuum are reported in Table 8.4; full structural details will be given in Appendix C as fractional coordinates.

The distance from the surface was calculated as the difference between the z coordinate of the centre of the benzene ring and the average z coordinate of the uppermost Cu layer. The adsorption process slightly increases both the I–I separation and the C–I bond lengths with respect to that of the isolated m–DIB. Moreover, the analysis of the C–I bond lengths shows that the lower symmetry of the A5x* and B5x sites also breaks down the internal symmetry of the molecule (cfr. Figure 8.2 and Table 8.4). This does not apply to A5y, whose internal symmetry is preserved due to the fact that, in this orientation, the adsorbate and the adsorption site share the invariance under reflection about the [001] axis.

If we assume, like it is reasonable to expect, that electron–induced reaction by means of an STM tip would lead to site–specific imprinting of both I atoms on the surface, similarly to the case of p–DIB [13], then the topological differences between the various orientations may be reflected in a different separation between the atoms, *i.e.* a different caliper size, as the two Iodine atoms will end up in different positions for every considered initial state. Moreover, for those initial states affected by it, the observed adsorption–induced broken symmetry may alter the cooperativity of the reaction. The latter consideration is of particular importance because the two most stable arrangements constitute, in fact, a bistable symmetric–asymmetric system in which the two states have very prominent symmetry differences.

Coverage effects

So far we have not discussed possible effects of surface crowding. Calculations at a coverage of 1/48 adsorbates per Cu atom show that, for lower coverage, adsorption energies are slightly larger but the stability order remains essentially unchanged. Only A5x* is affected significantly more. Results for the four most stable configurations are shown in Table 8.5.

8.3.3 Simulated STM images

We simulated STM images of the four most stable configurations starting from STM files obtained with VASP 5.2.11 [9, 10], with tip height ranging from 0.5 Å to 5.8 Å above the adsorbate and $\Delta z = 0.1\ a_0$ where a_0 is the Bohr radius. Currents were then computed using the Tersoff–Hamann model as implemented in BSKAN 3.6 [30], using 111×104×101 grid points in order to achieve good resolution.

Several images, not shown here, were calculated at different bias voltages ranging from

–1.0 V to +1.0 V with intervals of 0.2 V; the best results in terms of contrast and clarity were obtained at –0.2 V. Figure 8.5 shows isosurface plots obtained using gnuplot [31]. Computed STM images at different voltages are given in Appendix C.
The physisorbed molecules appear as bright heart–shaped protrusions with the I atoms in evidence and a clear distinction between the different structures. The two most stable configurations, *i.e.* B3x and B5x, have roughly the same energy and the corresponding STM images appear very similar to each other. Nevertheless, the two configurations differ as the B5x position has, by definition, lower symmetry which accordingly breaks down the internal symmetry of the physisorbed molecule. Furthermore, while B3x is flat, B5x is slightly tilted with respect to the surface. The tilting of B5x can be highlighted by plotting linescans along the [001] direction and through the positions of the I atoms as shown in Figure 8.3.

8.3.4 Physisorption or chemisorption?

As mentioned in Section 8.3.2, the question whether m–DIB on Cu(110) is physisorbed or chemisorbed cannot be solved by energy arguments alone. The distance between, for example, I and Cu atoms is smaller than the sum of the van der Waals radii, which can generally be considered a marker for chemisorption. Overall energies are also very large and can be consistent with chemisorption as well. However, we already argued that, subtracting the van der Waals binding energy, the adsorption energies are consistent with physisorption. In order to unambiguously clarify the nature of the bonding, we have computed the Density of States of the four most stable arrangements and compared it to that of the clean surface and the isolated m–DIB in vacuum, summed. The result for the most stable configuration (that is, B5x) is shown in Figure 8.4; results for B3x, A5y and A5x* are analogous and will be fully given in Appendix C. Comparison between the interacting and non interacting system unveils that no significant variation in the electronic structure occurs upon adsorption; hence, chemisorption is unlikely.
Furthermore, we have analyzed the partial charge distribution using Bader's method [32] as implemented in VASP 5.2.11 by Henkelman's group [33–35]. Results, reported in Table 8.6 for the most stable structure (B5x), show that little or no significant charge transfer occurs between the surface and the adsorbate, but all of the charge rearrangement is internal to the molecule. Results for B3x, A5y and A5x* are analogous and will be fully given in Appendix C. Where present, small variations of the charge distribution in the surface are entirely ascribable to dipole effects induced by the close proximity of a polar molecule. This is applicable to charge transfer between Cu atoms on the same xy plane as well as between different Copper layers: it should be noted that even the flat (with respect to the surface) arrangements have a nonzero dipole moment in the z direction, as the adsorption–induced distortion pushes the I atoms out of the molecular plane.

Therefore, since there is little or no charge transfer between the adsorbate and the surface, we can conclusively rule out the possibility of chemisorption and we may conclude that m–DIB on Cu(110) is physisorbed.
On the other hand, partial charge analysis for B3x and B5x pointed out some interesting features on which we shall focus in detail in Section 8.3.5.

8.3.5 B5x vs B3x: a possible bistable system?

The calculations show that two configurations, namely B5x and B3x, have nearly the same energy within the accuracy of the method, though they are, as discussed above, well distinct. This raises the interesting possibility of a bistable system in which the two states can be converted into one another through a reaction path. The two configurations exhibit similarities and differences: they have the same stability and very close adsorption sites, but B3x is symmetric while B5x is not; we shall thus focus on them in more detail.

Electronic structure

We computed the Density of States of adsorbed B3x and B5x and that of the molecules in vacuum keeping all the degrees of freedom frozen as they were physisorbed. For the latter, we compared the Density of States to that of the isolated and relaxed m–DIB in vacuum. Figure 8.6 shows that there is no significant difference between B5x and B3x (upper panel) and also that there is no significant change in the electronic structure of m–DIB upon adsorption (lower panel). Hence, the only substantial difference lies in the symmetry.
Partial charge analysis shows that the asymmetric structure has a very different charge distribution from that of the symmetric one. Table 8.7 shows that the charge distribution of B3x is perfectly symmetric while that of B5x is strongly polarized. If our hypothesis of the symmetric–asymmetric interconversion is correct, the transition from the symmetric state to the asymmetric state causes a dramatic internal charge rearrangement: besides the general rearrangement and symmetry breakdown in the benzene ring, charge is also transferred from the ring through C1 to one of the I atoms (I1, which is closer to the surface), which nearly recovers its original atomic charge; this translates, *de facto*, into weakening of the bond. This may clearly affect the reactivity and cooperativity of the imprinting reaction.
The considerations above open a whole new question; a thorough treatment of the properties of these two states, including Nudged Elastic Band studies of the conversion barrier between them and of the reactions with the surface starting from both the symmetric and the asymmetric reactant, to investigate the role of the symmetry in the reactivity, may shed some light on the features of this possible bistable system and will be the subject of a separate work.

8.4 Conclusions

We have computationally modelled the adsorption of 1,3–diiodobenzene on Cu(110) by means of Density Functional Theory including dispersion interaction using Grimme's method. We have compared the adsorption energies and structures of 23 possible configurations of the adsorbed molecule, concluding that all the orientations have roughly the same energy which leads the conclusion that the relative probabilities of observing them experimentally tends to the same order of magnitude at high temperatures while at low temperatures a strong preference for the two most stable arrangements is expected. The four most stable configurations are B5x, B3x, A5y and A5x* with adsorption energies larger than 2.15 eV, the asymmetric configurations are generally slightly favoured. The analysis of the electronic structure, namely Density of States and partial charge distribution, allows to rule out the possibility of chemisorption. For B5x and A5x* an adsorption–induced symmetry breakdown occurs which may affect their reactivity. Furthermore, we have simulated STM images for the four most stable configurations using the Tersoff–Hamann approach at different bias voltages. Focusing in particular on the two most stable configurations B3x and B5x, which are very close in energy and provide very similar STM images, we note that we are however able to distinguish the two by closely investigating both the computed structures and STM images; the difference can be highlighted by plotting linescans along the [001] direction of the lattice and through the positions of the I atoms. As it is been both theoretically and experimentally proven that halo–hydrocarbons easily react on metal and semiconductor surfaces and that the position of the resulting chemisorbed halogen atom can be controlled at the nanoscale, the present work is intended to be a preliminary approach to the more general question of whether the surface reactivity of Cu(110) can be locally changed by localized imprinting of a chemical object such as a single atom. Furthermore, there is evidence that the most stable arrangement is actually a bistable system (B5x/B3x, or asymmetric/symmetric).

8.5 Figures and tables

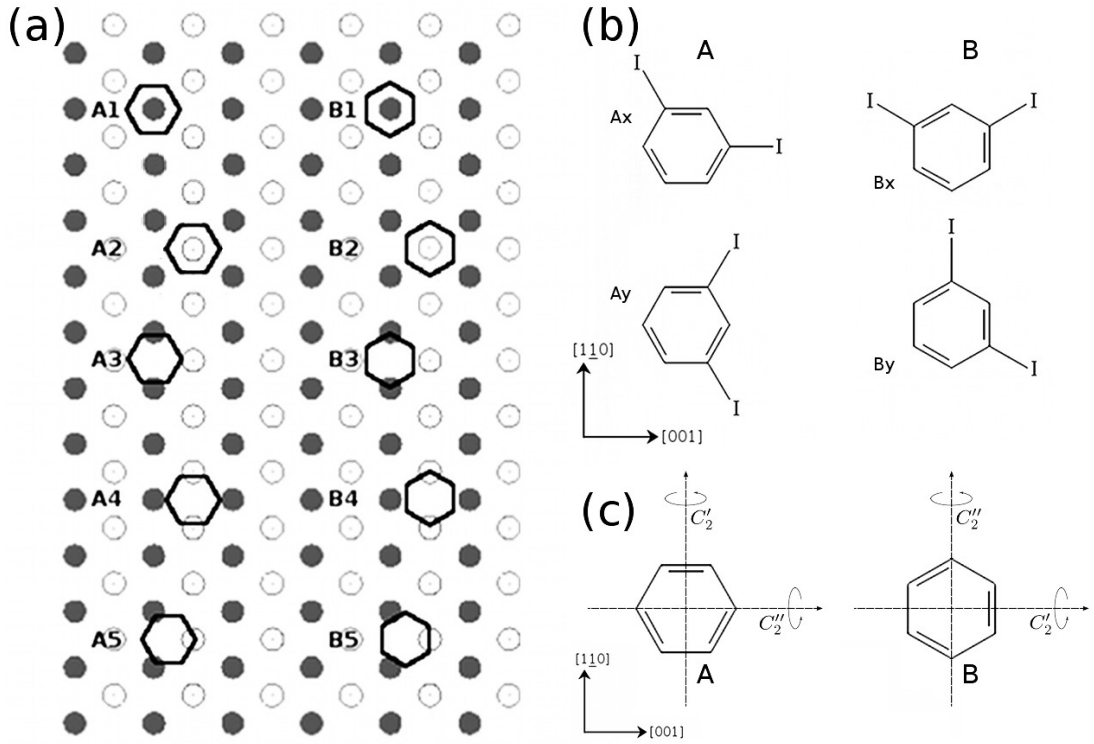

Figure 8.1: Panel (a): Base configurations classified by adsorption site. Full circles represent uppermost Cu atoms; empty circles represent the second layer. These configurations correspond to the adsorption configurations of unsubstituted benzene and each of them exists in both x and y orientations (see Panel (b)). Panel (b): Orientations of meta–diiodobenzene with respect to the [001] surface axis: Ax (top left), Ay (bottom left), Bx (top right), By (bottom right). Panel (c): A and B orientations of unsubstituted benzene classified by the position of C_2' and C_2'' rotational axes with respect to the surface.

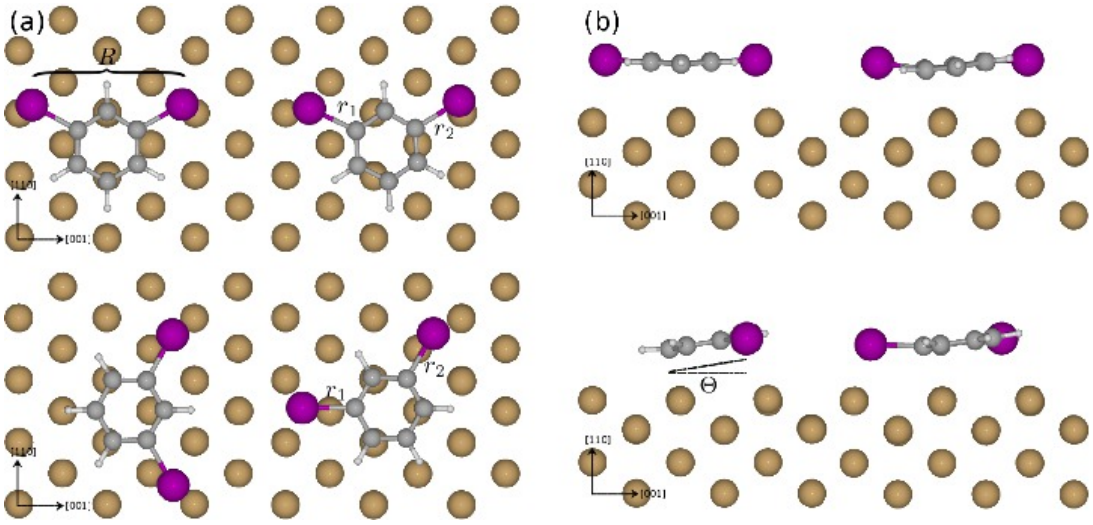

Figure 8.2: Panel (a): top view of the four most stable orientations of physisorbed m–DIB on Cu(110): B3x (top left), B5x (top right), A5y (bottom left), A5x* (bottom right). Internal coordinates are evidenced: R represents the I–I separation, while r_1 and r_2 represent the C–I bond lengths. Note that, while for B3x and A5y $r_1 = r_2 = r$, for B5x and A5x* the internal symmetry is broken and $r_1 \neq r_2$. Numerical details are given in Table 8.4. Panel (b): side view of the four most stable orientations of physisorbed m–DIB on Cu(110): B3x (top left), B5x (top right), A5y (bottom left), A5x* (bottom right). Dihedral angle Θ between the molecule and the surface is evidenced. Numerical details are given in Table 8.4.

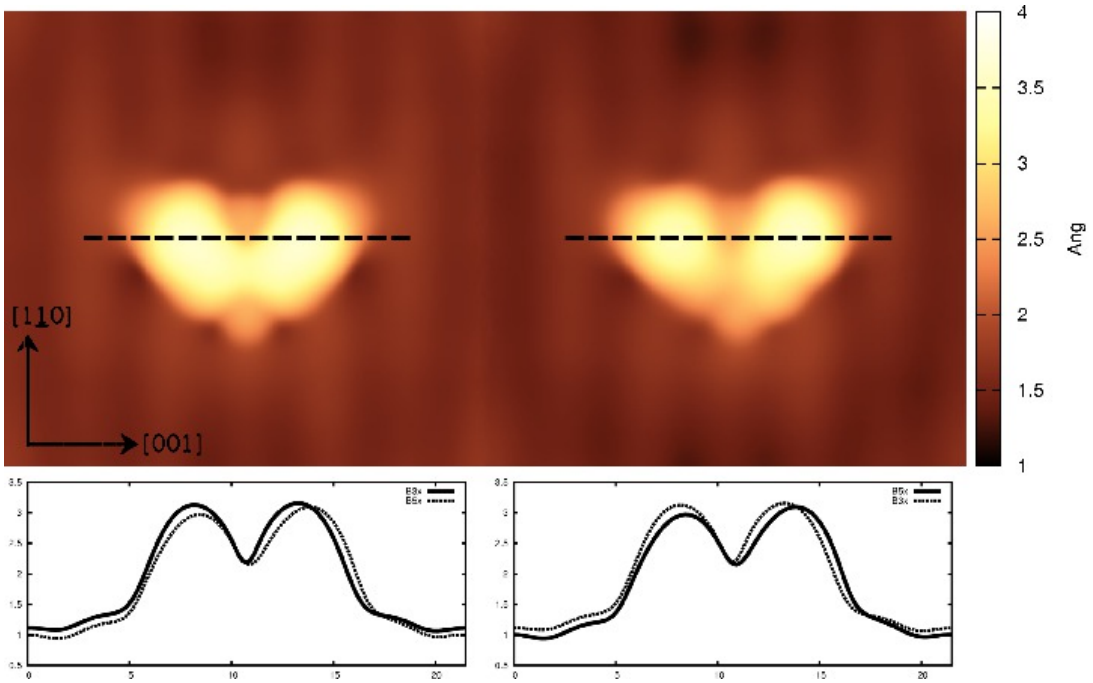

Figure 8.3: Simulated STM images and linescans for B3x (left) and B5x (right) along the direction marked by the dashed line. The comparison shows that the linescan is symmetric for B3x and asymmetric for B5x, in agreement with the computed structures. The images were taken at a bias voltage of –0.2 V and plotted as isocurrent surfaces at 0.001 pA.

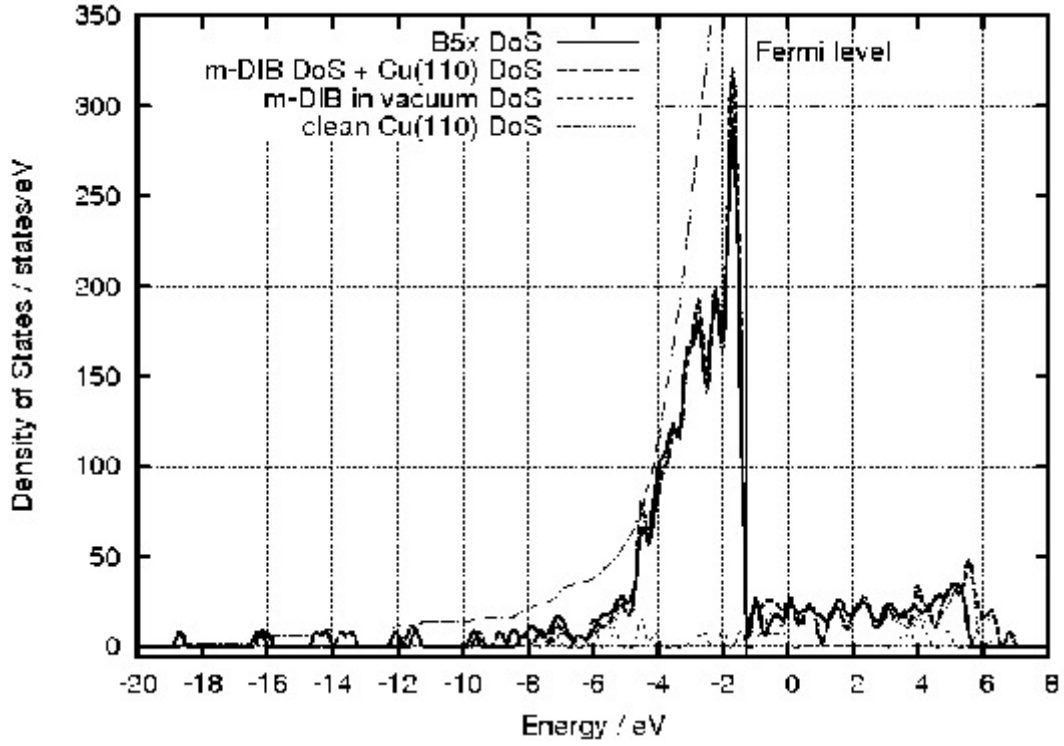

Figure 8.4: Density of States of the most stable arrangement (B5x) and its integral, compared it to that of the clean surface and the isolated m–DIB in vacuum, summed. Comparison between the interacting and non interacting system shows that no significant variation in the electronic structure occurs upon adsorption; hence, chemisorption is unlikely.

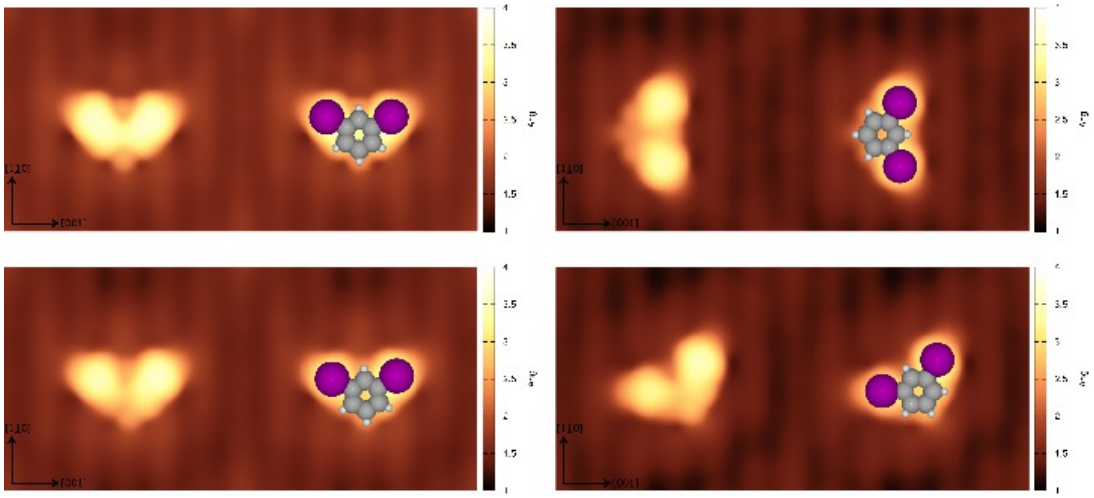

Figure 8.5: Simulated STM images of the four most stable configurations of m–DIB on Cu(110): B3x (top left), B5x (bottom left), A5y (top right), A5x* (bottom right). An overlay of the corresponding structure is shown on the right side of each panel. The images were taken at a bias voltage of –0.2 V and plotted as isocurrent surfaces at 0.001 pA.

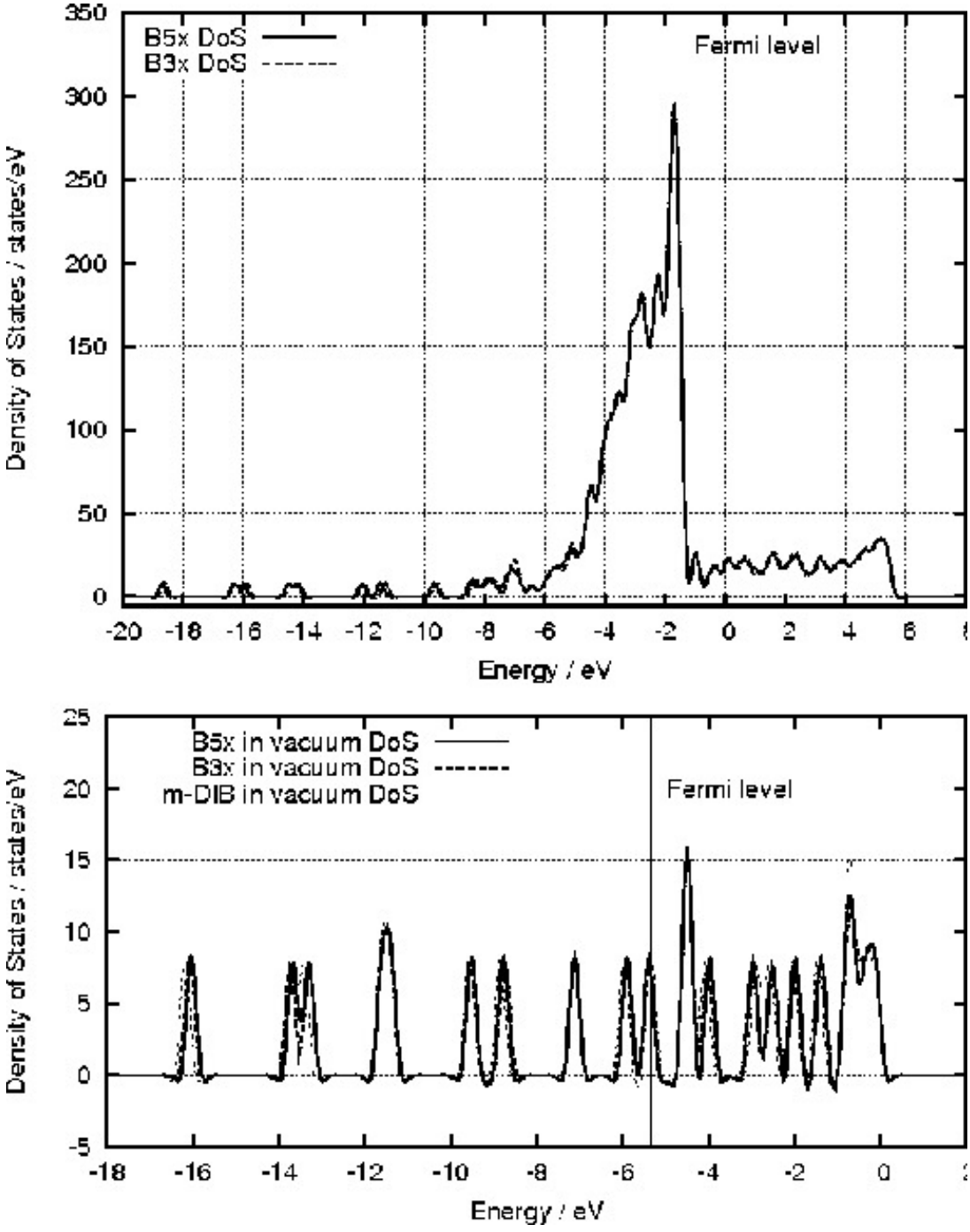

Figure 8.6: Upper panel: Computed Density of States of adsorbed B5x and B3x. There is no significant difference between the electronic structures. Lower panel: Computed Density of States of the B5x and B3x in vacuum keeping all the degrees of freedom frozen as they were physisorbed, compared the Density of States to that of the isolated and relaxed m–DIB in vacuum. The densities of states are almost identical, hence there is no significant change in the electronic structure of m–DIB upon adsorption.

State	E_{ads} /eV	E_{ads} /kJ·mol^{-1}	$\Theta/^\circ$	State	E_{ads} /eV	E_{ads} /kJ·mol^{-1}	$\Theta/^\circ$
A1x	1.968	190.0	4.35	B1x	1.961	189.2	Flat
A1y	1.901	183.4	5.00	B1y	1.964	189.5	Flat
A2x	1.824	176.0	Flat	B2x	1.835	177.1	Flat
A2y	2.010	193.9	Flat	B2y	2.110	203.6	5.12
A3x	2.126	205.2	Flat	**B3x**	**2.224**	**214.6**	**Flat**
A3y	2.217[†]	213.9	9.32	B3y	2.020	194.9	9.86
A4x	1.841	177.6	Flat	B4x	1.832	176.7	Flat
A4y	2.045	197.3	Flat	B4y	2.137	206.1	5.31
A5x	2.019	194.8	Flat	**B5x**	**2.230**	**215.1**	**6.85**
A5y	**2.217**	**213.9**	**9.32**	B5y	2.144	206.7	7.51
A5x*	**2.163**	**208.7**	**6.16**	B5x*[‡]	2.230	215.1	6.85
A5y*	1.957	188.9	6.39	B5y*	2.071	199.8	7.58

[†]shifted to A5y.

[‡]equivalent to B5x.

Table 8.1: Adsorption energies of pyhisisorbed m–DIB on Cu(110) and dihedral angles between the ring plane and the Copper surface. For the nomenclature of the structures cfr. Fig. 8.1. Angles less than 4° are approximated to flat. The values for the four most stable arrangements are reported in bold.

State.	E_{ads} (vdW)	E_{ads} (no vdW)	vdW binding energy
A1x	1.968 eV	0.365 eV	1.603 eV
A1y	1.901 eV	0.183 eV	1.718 eV
A2x	1.822 eV	0.263 eV	1.561 eV
A2y	2.010 eV	0.431 eV	1.579 eV
A3x	2.126 eV	0.334 eV	1.792 eV
A3y[†]	–	–	–
A4x	1.841 eV	0.255 eV	1.586 eV
A4y	2.045 eV	0.425 eV	1.620 eV
A5x	2.019 eV	0.422 eV	1.598 eV
A5y	2.217 eV	0.367 eV	1.850 eV
A5x*	2.163 eV	0.386 eV	1.777 eV
A5y*	1.957 eV	0.260 eV	1.698 eV
B1x	1.961 eV	0.421 eV	1.540 eV
B1y	1.964 eV	0.457 eV	1.507 eV
B2x	1.835 eV	0.220 eV	1.615 eV
B2y	2.110 eV	0.326 eV	1.785 eV
B3x	2.224 eV	0.479 eV	1.745 eV
B3y	2.020 eV	0.406 eV	1.614 eV
B4x	1.832 eV	0.227 eV	1.605 eV
B4y	2.137 eV	0.372 eV	1.765 eV
B5x	2.230 eV	0.396 eV	1.833 eV
B5y	2.144 eV	0.371 eV	1.773 eV
B5x*[‡]	–	–	–
B5y*	2.071 eV	0.158 eV	1.913 eV

[†]shifted to A5y.

[‡]equivalent to B5x.

Table 8.2: Approximated van der Waals binding energies of pyhisisorbed m–DIB on Cu(110). For the nomenclature of the structures cfr. Fig. 8.1. The average van der Waals binding energy is 1.685 eV.

State (α).	E_{ads}/eV	N_α/N_{ref} at liquid He T	N_α/N_{ref} at liquid N_2 T	N_α/N_{ref} at room T
B5x (ref.)	2.230	1	1	1
B3x	2.224	$1.56{\cdot}10^{-7}$	$4.24 \cdot 10^{-1}$	$8.01 \cdot 10^{-1}$
A5y	2.217	0	$1.53 \cdot 10^{-1}$	$6.16 \cdot 10^{-1}$
A5x*	2.163	0	$4.40 \cdot 10^{-5}$	$7.49 \cdot 10^{-2}$
A2x	1.824	0	0	$1.40 \cdot 10^{-7}$

Table 8.3: Population ratio of the four most stable configurations and the least stable configuration according to Boltzmann equation $N_\alpha/N_{\text{ref}} = \exp(-\Delta E_{\text{ads}}/kT)$ at three easily accessible experimental temperatures: liquid Helium (4.22 K), liquid N_2 (77.0 K) and room temperature (298.0 K). The reference population N_{ref} is that of the most stable adsorption arrangement (B5x). While at high temperatures relative populations of configurations with similar energy tend to the same order of magnitude, at low temperatures a strong preference for the two most stable adsorption arrangements is expected.

State	Height	Θ	R(I–I)	r(C–I)
B5x	2.36 Å	6.85 °	6.13 Å	$r_1 = 2.14$ Å; $r_2 = 2.12$ Å
B3x	2.44 Å	Flat	6.12 Å	$r_1 = r_2 = r = 2.12$ Å
A5y	2.34 Å	9.32 °	6.20 Å	$r_1 = r_2 = r = 2.17$ Å
A5x*	2.39 Å	6.15 °	6.14 Å	$r_1 = 2.16$ Å; $r_2 = 2.15$ Å
m–DIB$_{vac}$	-	-	6.05 Å	$r_1 = r_2 = 2.11$ Å

Table 8.4: Structural details of the four most stable orientations of physisorbed m–DIB on Cu(110) (B5x, B3x, A5y and A5x* in order of stability) compared to that of the m–DIB in vacuum. The height above surface was calculated as the difference between the z coordinate of the centre of mass of the adsorbate and the average z coordinate of the uppermost Cu layer. The adsorption process slightly increases both the I–I separation and the C–I bond lengths. Moreover, investigation of the C–I bond lengths shows that the asymmetry of the A5x* and B5x adsorption sites also breaks the internal symmetry of the molecule (cfr. Fig. 8.2).

State	E_{ads} at 1/12 adsorbates/Cu atom	E_{ads} at 1/48 adsorbates/Cu atom
B5x	2.230 eV	2.535 eV
B3x	2.224 eV	2.482 eV
A5y	2.217 eV	2.417 eV
A5x*	2.163 eV	2.464 eV

Table 8.5: Effect of surface crowding on the adsorption energies of the four most stable arrangements. Coverages of $1.53 \cdot 10^{-8}$ mol/cm^2 and $3.83 \cdot 10^{-9}$ mol/cm^2 are compared for the four most stable adsorption arrangements. For lower coverage, adsorption energies are slightly larger but the stability order remains essentially unchanged. Only A5x* is affected.

Atom(s)	Charge $/e^-$ (interacting)	Charge $/e^-$ (non interacting)	Difference
I1†	6.78	6.10	–0.68
I2‡	6.01	6.07	+0.06
C1†	4.46	5.24	+0.78
C2	3.97	3.84	–0.13
C3‡	5.14	5.01	–0.13
C4	3.99	4.12	+0.13
C5	4.02	3.87	–0.15
C6	4.10	4.00	–0.10
Cu I layer (avg)	11.00	10.99	–0.01
Cu II layer (avg)	11.03	10.98	–0.05
Cu internal layers (avg)	11.01	11.03	+0.02
Adsorbate (total)	38.47	38.25	–0.22
Surface (total)	528.56	528.22	–0.34

Table 8.6: Partial charge analysis for the most stable configuration B5x. Bonded atoms are marked with † and ‡. Partial charges for the interacting and non–interacting system are reported in columns 1 and 2 respectively. The charge rearrangement is entirely internal to the molecule; small deviations are ascribable to small errors intrinsic in the method, a good estimate of which is given by the electron count (last two rows). Since there is no charge transfer between the adsorbate and the surface, we can conclusively rule out the possibility of chemisorption.

Atom(s)	Charge $/e^-$ B5x	Charge $/e^-$ B3x	Difference
I1†	6.78	6.02	–0.76
I2‡	6.01	6.00	–0.01
C1†	4.46	3.84	–0.62
C2	3.97	4.17	+0.20
C3‡	5.14	3.85	–1.29
C4	3.99	5.27	+1.28
C5	4.02	3.97	–0.05
C6	4.10	5.27	+1.17
Adsorbate (total)	38.47	38.25	–0.08

Table 8.7: Comparison between the partial charge distributions of B5x (asymmetric) and B3x (asymmetric). The charge distribution of B3x is perfectly symmetric while that of B3x is strongly polarized. If our hypothesis of bistability is correct, the transition from the symmetric state to the asymmetric state causes a large charge transfer from the ring through C1 to I1, which nearly recovers its original atomic charge; this translates, *de facto*, into weakening of the bond.

REFERENCES

[1] R. A. Wolkow. Controlled molecular adsorption on silicon: Laying a foundation for molecular devices. *Annual Reviews of Physical Chemistry*, 50(1):413–441, 1999.

[2] I. R. McNab and J. C. Polanyi. Patterned atomic reaction at surfaces. *Chemical Reviews*, 106(10):4321–4354, 2006.

[3] J. V. Barth, G. Costantini, and K. Kern. Engineering atomic and molecular nanostructures at surfaces. *Nature*, 437(7059):671–679, 2005.

[4] P. Maksymovych and J. T. Yates. Propagation of conformation in the surface–aligned dissociation of single ch3ssch3 molecules on au(111). *Journal of the American Chemical Society*, 128(33):10642–10643, 2006.

[5] K. R. Harikumar, I. R. McNab, J. C. Polanyi, A. Zabet-Khosousi, and W. A. Hofer. Imprinting self–assembled patterns of lines at a semiconductor surface, using heat, light, or electrons. *Proceedings of the National Academy of Sciences*, 108(3):950–5, January 2011.

[6] K. R. Harikumar, I. R. McNab, J. C. Polanyi, A. Zabet-Khosousi, C. Panosetti, and W. A. Hofer. Stereo–isomerism controls surface reactivity: 1–chloropentane–pairs on Si(100)–2×1. *Chemical Communications*, 47(44):12101–3, November 2011.

[7] K. R. Harikumar, L. Leung, I. R. McNab, J. C. Polanyi, H. Lin, and W. A. Hofer. Cooperative molecular dynamics in surface reactions. *Nature Chemistry*, 1(9):716–721, 2009.

[8] K. R. Harikumar, T. Lim, I. R. McNab, J. C. Polanyi, L. A. Zotti, S. Ayissi, and W. A. Hofer. Dipole–directed assembly of lines of 1,5–dichloropentane on silicon substrates by displacement of surface charge. *Nature Nanotechnology*, 3(4):222–228, 2008.

[9] G. Kresse and J. Furthmüller. Efficiency of ab–initio total energy calculations for metals and semiconductors using a plane–wave basis set. *Computational Materials Science*, 6(1):15–50, 1996.

[10] G. Kresse and J. Furthmüller. Efficient iterative schemes for *ab initio* total–energy calculations using a plane–wave basis set. *Physical Review B*, 54:11169–11186, 1996.

[11] J. Tersoff and D. R. Hamann. Theory of the scanning tunneling microscope. *Physical Review B*, 31:805–813, 1985.

[12] J. Tersoff and D. R. Hamann. Theory and application for the scanning tunneling microscope. *Physical Review Letters*, 50:1998–2001, 1983.

[13] L. Leung, T. B. Lim, J. C. Polanyi, and W. A. Hofer. Molecular calipers control atomic separation at a metal surface. *Nano Letters*, 11(10):4113–4117, 2011.

[14] M. S. Chen and D. W. Goodman. The structure of catalytically active gold on titania. *Science*, 306(5694):252–255, 2004.

[15] P. H. Lu, J. C. Polanyi, and D. Rogers. Electron–induced localized atomic reaction (LAR): Chlorobenzene adsorbed on Si(111)–7×7. *Journal of Chemical Physics*, 111(22):9905–9907, 1999.

[16] S. Dobrin, K. R. Harikumar, and J. C. Polanyi. An STM study of the localized atomic reaction of 1,2– and 1,4–dibromobenzene at Si(111)–7×7. *Surface Science*, 561(1):11–24, 2004.

[17] S. Dobrin, K. R. Harikumar, C. F. Matta, and J. C. Polanyi. An STM study of the localized atomic reaction of 1,2– and 1,4–dibromoxylene with Si(111)–7×7. *Surface Science*, 580:39–50, 2005.

[18] P. Hohenberg and W. Kohn. Inhomogeneous electron gas. *Physical Review*, 136:B864–B871, 1964.

[19] W. Kohn and L. J. Sham. Self–consistent equations including exchange and correlation effects. *Physical Review*, 140:A1133–A1138, 1965.

[20] J. P. Perdew, K. Burke, and M. Ernzerhof. Generalized gradient approximation made simple. *Physical Review Letters*, 77:3865, 1996.

[21] J. P. Perdew, K. Burke, and M. Ernzerhof. Erratum: Generalized gradient approximation made simple. *Physical Review Letters*, 78:1396, 1997.

[22] P. E. Blöchl. Projector augmented–wave method. *Phys. Rev. B*, 50:17953–17979, 1994.

[23] G. Kresse and D. Joubert. From ultrasoft pseudopotentials to the projector augmented–wave method. *Physical Review B*, 59:1758–1775, 1999.

[24] P. Pulay. Convergence acceleration of iterative sequences. the case of scf iteration. *Chemical Physics Letters*, 73(2):393–398, 1980.

[25] S. Grimme. Semiempirical gga–type density functional constructed with a long–range dispersion correction. *Journal of Computational Chemistry*, 27(15):1787–1799, 2006.

[26] S. R. Bahn and K. W. Jacobsen. An object–oriented scripting interface to a legacy electronic structure code. *Computing in Science and Engineering*, 4(3):56–66, 2002.

[27] P. Haas, F. Tran, and P. Blaha. Calculation of the lattice constant of solids with semilocal functionals. *Physical Review B*, 79:085104, 2009.

[28] M. E. Straumanis and L. S. Yu. Lattice parameters, densities, expansion coefficients and perfection of structure of cu and of cu–in α phase. *Acta Crystallographica Section A*, 25(6):676–682, 1969.

[29] L. A. Zotti, G. Teobaldi, K. Palotás, W. Ji, H. J. Gao, and W. A. Hofer. Adsorption of benzene, fluorobenzene and meta–di–fluorobenzene on Cu(110): A computational study. *Journal of Computational Chemistry*, 29(10):1589–1595, 2008.

[30] W. A. Hofer, A. J. Fisher, G. P. Lopinski, and R. A. Wolkow. Adsorption of benzene on Si(100)–(2×1): Adsorption energies and STM image analysis by ab initio methods. *Physical Review B*, 63:085314, 2001.

[31] J. Racine. gnuplot 4.0: a portable interactive plotting utility. *Journal of Applied Econometrics*, 21(1):133–141, 2006.

[32] R. F. W. Bader. *Atoms in Molecules: A Quantum Theory (International Series of Monographs on Chemistry)*. Oxford University Press, USA, 1994.

[33] G. Henkelman, A. Arnaldsson, and H. Jonsson. A fast and robust algorithm for Bader decomposition of charge density. *Computational Materials Science*, 36(3):354–360, 2006.

[34] Edward Sanville, Steven D. Kenny, Roger Smith, and Graeme Henkelman. Improved grid–based algorithm for Bader charge allocation. *Journal of Computational Chemistry*, 28(5):899–908, 2007.

[35] W. Tang, E. Sanville, and G. Henkelman. A grid–based Bader analysis algorithm without lattice bias. *Journal of Physics: Condensed Matter*, 21(8):084204, 2009.

Chapter 9

Ground state reactivity of p– and m–diiodobenzene on Cu(110)

In Chapter 8, the stability of m–diiodobenzene on Cu(110) [1] was thoroughly analyzed. As aforementioned, molecules such as the latter drew interest as possible templates for Localized Atomic Reactions on smooth metal surface, as suggested by the work of L. Leung *et. al.* on p–diiodobenzene [2]. In the present Chapter we will thus investigate ground state reactive processes of both p– and m–diiodobenzene. It is known from both experimental and theoretical work on p–diiodobenzene [3] that the reaction mechanism involves the formation of a transient charged intermediate, and hence its accurate description would require a DFT–based Molecular Dynamics approach combining an *ab initio* ground state potential with a ionic pseudopotential for the I atoms as described and employed in Ref. [3].
Such description of the system requires a ground state calculation as a basis. Alternatively, ground state MEPs, which themselves describe how the reaction would occur if it were thermal, can also provide interesting insights on the electron–induced mechanism of reaction.
Before discussing the reactive processes, we will show in Section 9.2.1 that further investigation by means of CI–NEB removes the ambiguity raised in Chapter 8, that is, allows to determine which configuration of m–diiodobenzene is actually the ground adsorption state.

9.1 Theory

9.1.1 Theoretical setup

Throughout all the calculations, we employed essentially the same setup as in Chapter 8, that is, Density Functional Theory (DFT) [4, 5] as implemented in VASP 5.2.11 [6, 7] using the Generalized Gradient Approximation potentials developed by Perdew–Burke–Ernzerhof (GGA–PBE potentials) [8, 9] in conjunction with the projected augmented wave approach for core electrons [10, 11]. The Brillouin zone was sampled using a

3×3×1 K–point with a 4×3 supercell, while for the calculation of C–I bond cleavage of p– and m–diiodobenzene we employed a supercell of 5×4 which is large enough to sample the Brillouin zone using the Γ point only. The cutoff energy was set to 400 eV. The SCF convergence criterion was set to 10^{-4} eV.
Where needed, structural minimization was accomplished by means of the Quasi–Newton algorithm [12] including van der Waals dispersion correction using Grimme's method [13]. The structural minimization was carried out until the forces acting on each nucleus were < 0.02 eV/Å, relaxing the molecular degrees of freedom together with the two uppermost layers of the Cu slab, while the bottom Copper layers were kept frozen. The clean surface was generated using the python–based ASE package [14], as a slab of 4×3 or 6×4 Cu atoms and 4 layers with the same computationally optimized lattice constant employed in Chapter 8 and Ref. [1] and adding 16 Å of vacuum.

9.1.2 Climbing–image Nudged Elastic Band

The search for minimum energy paths was carried out using the Nudged Elastic Band (NEB) method [15] in its Climbing Image variant [16], as described in Chapter 6. The initial guess for the path was generated as a chain of 5 replicas obtained as linear interpolation of the coordinates of the initial and final states. The constrained optimization was carried out until the maximum force acting on each image were < 0.02 eV/Å.

9.2 Results

9.2.1 Ground adsorption state of m–diiodobenzene on Cu(110)

In Chapter 8, we found that the two most stable arrangements of m–diiodobenzene on Cu(110), that is, B3x and B5x, shown in Fig. 9.1, exhibit very close features differing only in their symmetry. Their computed energies are so close to each other that it is actually impossible, within the accuracy of the model and in the lack of experimental observations, to unambiguously determine which one is the real ground state.
We hence proposed that the two constitute a bistable system. If our ansatz were to be true, then there would exist a conversion barrier between the two states. Therefore, we performed a Nudged Elastic Band calculation choosing B3x as the initial state and B5x, which is slightly more stable, as the final state.
Such calculation converges to a barrierless minimum energy path, that is, the symmetry of B3x is broken and its conversion into B5x is barrierless, in line with the general result that asymmetric arrangements are favoured. The computed minimum energy path is shown in Fig. 9.2.
From the theoretical and methodological point of view, such a result means that, when a potential energy hypersurface is particularly smooth, such as the case of Cu(110), the flatness of minima and maxima can lead to the artefact that, during structure

optimization, a saddle point is mistaken for a local minimum, as the criterion for convergence is a force threshold. While, in principle, an analysis of the Hessian matrix could avoid this artefact by identifying the imaginary mode, its diagonalization does not make sense in the neighborhood of a very flat stationary point, as the harmonic approximation breaks down.

In the light of this, we may conclude that the ground state of m–diiodobenzene is indeed a bistable system, but constituted by B5x and B5x*, that is, its reflection with respect to the [1$\underline{1}$0] surface axis, in lieu of the B3x/B5x couple proposed in Chapter 8. In this picture, B3x becomes the transition state of the interconversion process between B5x and B5x*. The activation barrier will then be equal to the computed energy difference between B3x and B5x as calculated in Chapter 8, that is, about 6 meV. In order to confirm this, we performed a Nudged Elastic Band calculation between B5x and B5x* and we find a barrier of 13.0 meV. The discrepancy is due to the fact that, in the latter calculations, we made the convergence criterion stricter by lowering the threshold to 0.01 eV/Å in order to enhance the barrier. This led to further optimization of the initial state, thus lowering its energy and increasing the conversion barrier. The computed minimum energy path is reported in Fig. 9.3.

9.2.2 Ground state MEPs for single I–C bond cleavage of p–DIB on Cu(110).

We carried out three separate CI–NEB calculations using the same initial state and three final states as shown in Figure 9.4. The initial state is the physisorbed p–diiodobenzene with its phenyl ring lying flat on the surface. The centre of the molecule and the two I atoms are aligned across the [001] direction occupying three adjacent short bridge positions. The three final states present the IPh group tilted and chemically attached to closest available Cu atom, while the imprinted I atom is chemisorbed in the first 4–fold hollow, first short bridge and second 4–fold hollow positions.

We find that all three processes present the same barrier of 640 meV, indicating that the three mechanisms share the first stage of the reaction, that is, the I atom reacts locally in the first 4–fold hollow position, and subsequently diffuses to the adjacent available sites.

This result is in agreement with the fact that the reaction is not thermal. In fact, if the reaction occured via a thermal, ground–state mechanism, the probability of the three outcomes would be equal or at least governed by the rate of diffusion of a single I atom along the [001] surface axis, leading to an uniform, or only slightly peaked, distribution of the position of the imprinted I atom along the [001] axis. However, for the purpose of this Chapter we are not interested in reproducing the actual reaction mechanism, as it was already cleared in Ref. [3], but our aim is to point out the effect of molecular symmetry on reactivity by comparing the ground–state reaction paths of

p–diiodobenzene (symmetric) and m–diiodobenzene (asymmetric).
The Ground–state reaction paths for p–diiodobenzene are shown in Fig. 9.5.

9.2.3 Ground state MEP for single I–C bond cleavage of m–DIB on Cu(110).

For m–diiodobenzene, we carried out a single CI–NEB run using the ground adsorption arrangement B5x as the initial state, while the final state was chosen, similarly to p–diiodobenzene, as a tilted chemically attached IPh and a chemisorbed I atom in the next available long bridge position. In Chapter 8 and Ref [1], we had shown by means of Bader's charge analysis [17] that the broken symmetry of this adsorption configuration induces an internal partial charge rearrangement such that the I atom closer to the surface nearly recovers all its charge. We thus modelled the cleavage of this polarized and weakened C–I bond, expecting to find it greatly facilitated. The obtained results confirm this hypothesis. The reaction path, presenting a barrier of 117 meV, much smaller than the 640 meV barrier for the reaction of the p– isomer, are shown in Fig. 9.6. Of note, analyzing the reaction coordinate in detail, we find that the reaction can be considered complete when the I atom is in the first available short bridge position. Similarly to p–diiodobenzene, the ground state process governing the reaction is that such as the I atom reacts and occupies the closest available site and subsequently diffuses to adjacent positions.
A summary of all the transition barriers calculated in the present Chapter is reported in Table 9.1.

9.3 Conclusions

By attempting to compute the conversion barrier of the B3x/B5x bistable system hypothesized in Chapter 8 and finding a barrierless transition, we have unambiguously determined that the ground adsorption configuration of m–diiodobenzene on Cu(110) is the asymmetric B5x arrangement. More precisely, since B5x and its reflection B5x* with respect to the [1$\underline{1}$0] surface axis have, by symmetry considerations, identical energy and probability of experimental observation, we may conclude that the latter B5x/B5x* constitute a bistable ground adsorption with an interconversion barrier of 13.0 meV where the transition state is the state we had defined as the symmetric B3x. In the light of this, we compared electronic ground state reaction paths for p– and m–diiodobenzene on Cu(110) in order to investigate the effect of the symmetry of the initial state on the surface reactivity. We find that, while the first C–I bond cleavage of p–diiodobenzene presents a barrier of 640 meV, is asymmetric counterpart m–diiodobenzene, possessing one C–I bond that is already strongly polarized due to internal partial charge rearrangement upon adsorption, presents a barrier of only 117

meV. Therefore, for m–diiodobenzene, in a ground state picture, the reactivity is remarkably influenced by the broken symmetry of the initial state. This may lead to the fact that, on one hand, the reaction may lose cooperativity, or even occur for only one C–I bond, thus imprinting one single I atom on the surface in lieu of two, but on the other hand the facility of the bond cleavage is strongly enhanced with respect to the symmetric template. This implies that it is possible, in principle, not only to tune the I–I separation at the surface by choosing the appropriate length of the initial chain of p–diiodobenzene molecule, but also to choose whether to imprint two or one I atoms on the surface by selecting the desired molecular template. This fact could open promising routes toward the tailored functionalization of smooth metal surfaces similarly to the already well assessed patterning techniques of Silicon.

9.4 Figures and tables

Transition	B3x $\rightarrow$ B5x	B5x $\rightleftharpoons$ B5x*	m-DIB 1^{st} C–I	p–DIB 1^{st} C–I
Barrier / meV	0	13.0	117	640

Table 9.1: Summary of transition barriers of ground state reactive processes of diiodobenzenes on Cu(110): conformational change from B3x (symmetric) to B5x (asymmetric) arrangement of m–diiodobenzene; conformational change between the two ground arrangement B5x and B5x* of m–diiodobenzene; first I–C bond cleavage of m–diiodobenzene (asymmetric); first I–C bond cleavage of p–diiodobenzene (symmetric).

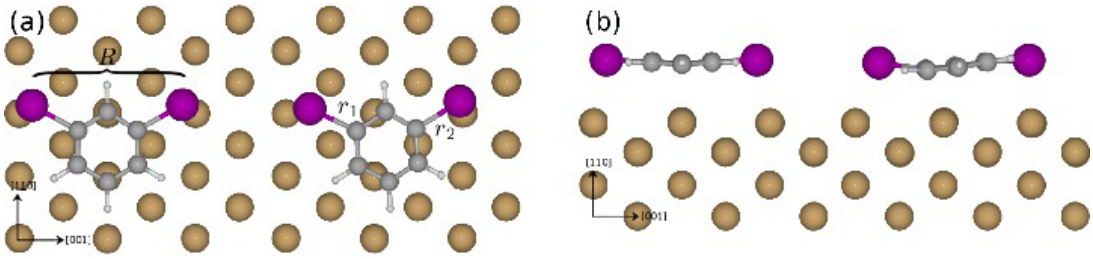

Figure 9.1: Top (a) and side (b) view of the B3x (left) and B5x (right) adsorption arrangements of physisorbed m–DIB on Cu(110). Internal coordinates are evidenced: R represents the I–I separation, while r_1 and r_2 represent the C–I bond lengths. It is worth remarking that, for B5x, $r_1 > r_2$ and the I atom closer to the surface bears a partial charge of almost 7, thus the bond is strongly polarized.

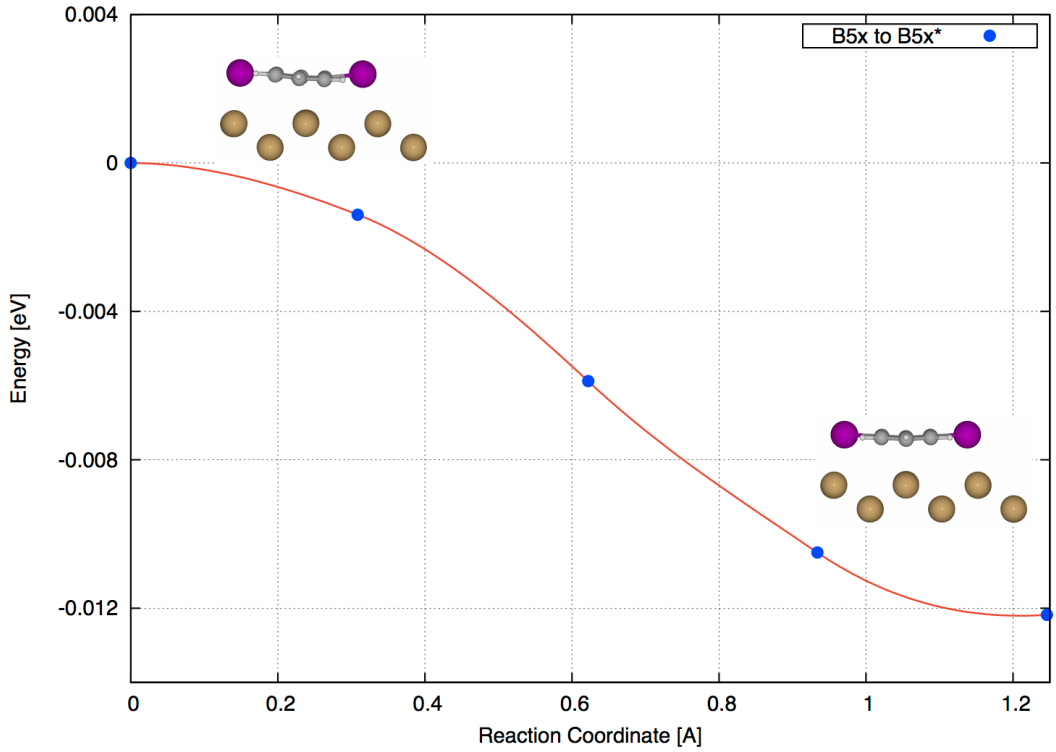

Figure 9.2: CI–NEB calculation showing that the transition from the symmetric B3x state to the asymmetric B5x state is barrierless.

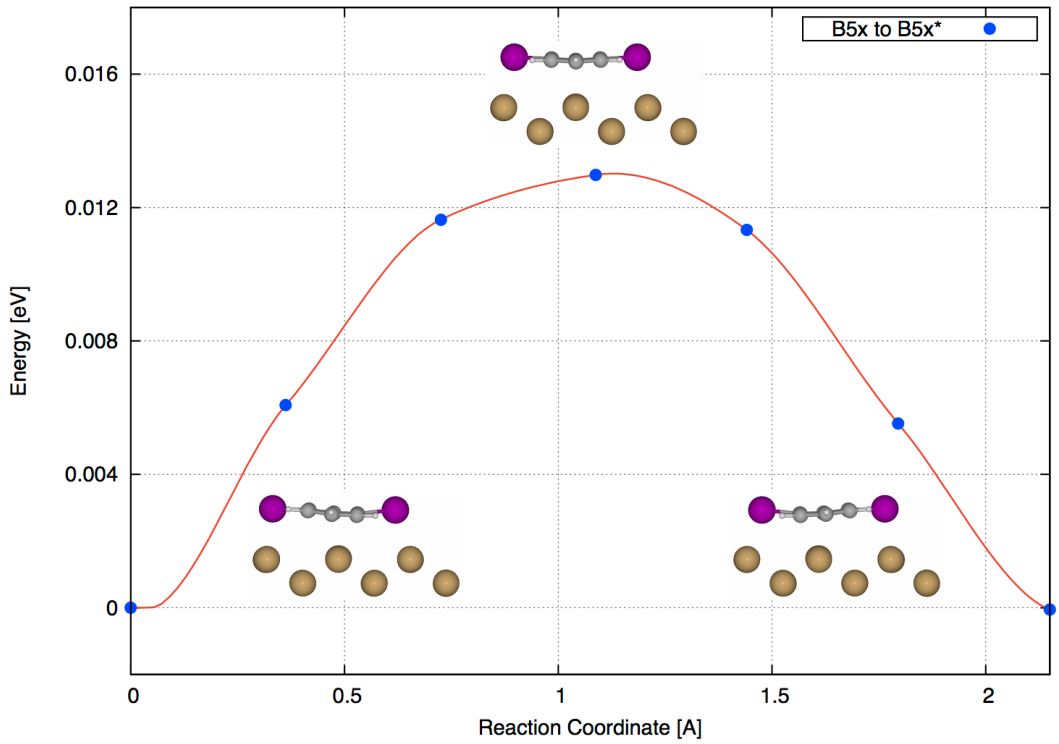

Figure 9.3: Computed minimum energy path for the interconverstion between the ground adsorption state B5x of m–diiodobenzene on Cu(110) and its reflection B5x* with respect to the [1$\underline{1}$0] surface axis. The (enhanced) barrier is 13.0 meV

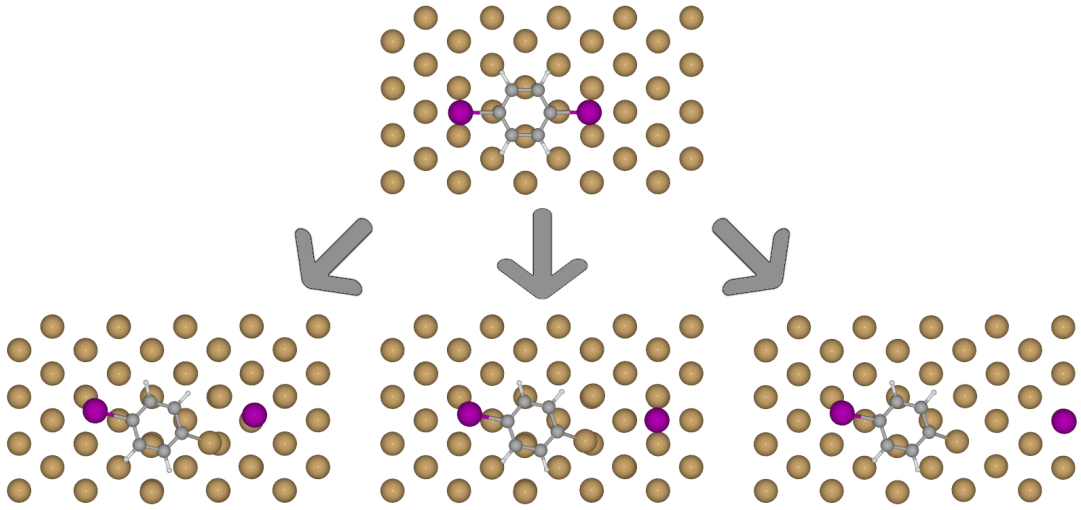

Figure 9.4: Initial (top) and three possible final states for the reaction of p–diiodobenzene on Cu(110). The three final states taken into account present the IPh group tilted and chemically attached to closest available Cu atom, while the imprinted I atom is chemisorbed in the first 4–fold hollow (bottom left), first short bridge (bottom centre) and second 4–fold hollow (bottom right) positions.

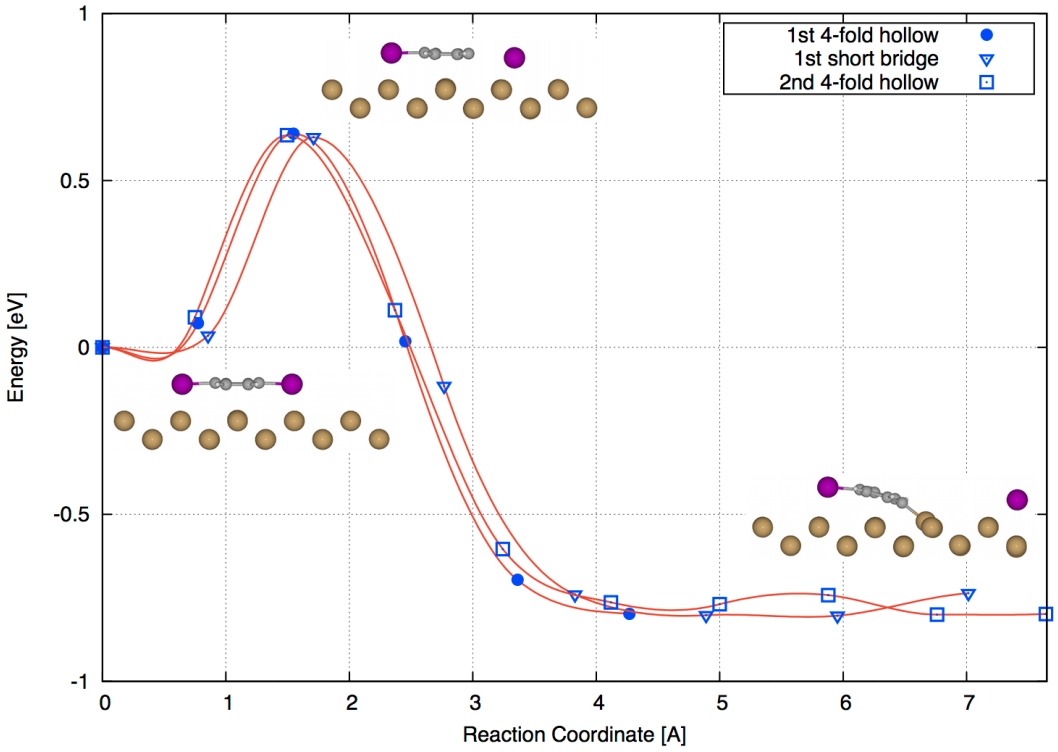

Figure 9.5: Computed CI–NEB minimum energy paths for the first C–I bond cleavage of p–diiodobenzene on Cu(110). The three final states correspond to the imprinted I atom chemisorbed in the first 4–fold hollow, first short bridge and second 4–fold hollow positions. All three processes present the same barrier of 640 meV.

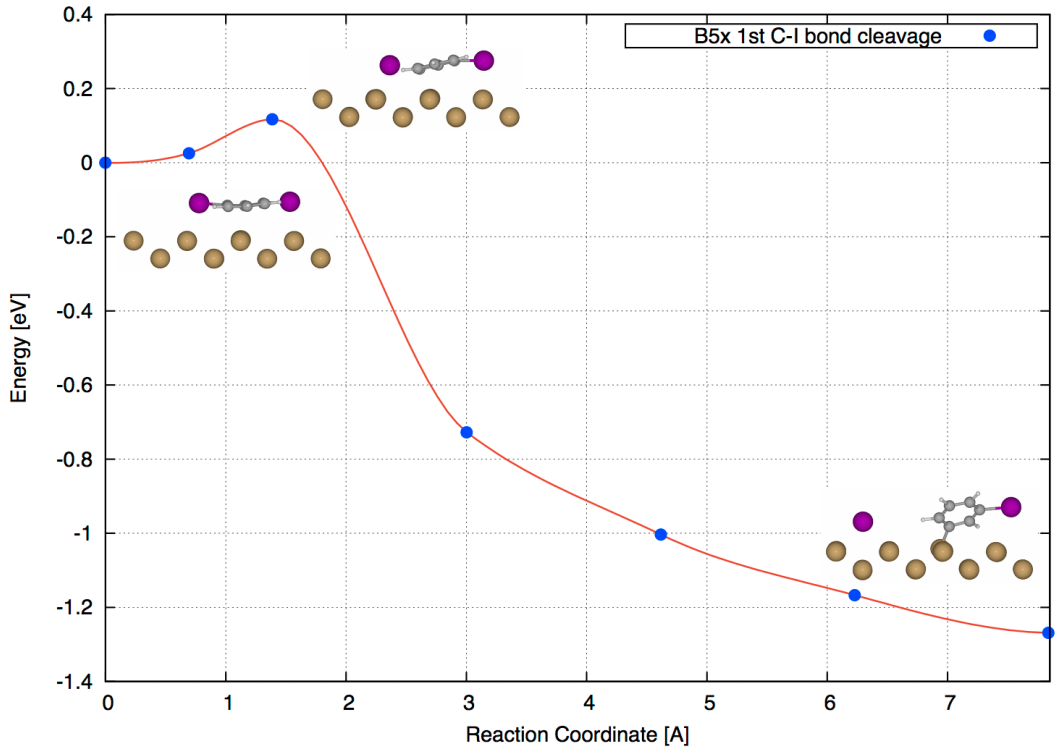

Figure 9.6: Computed CI–NEB minimum energy paths for the first C–I bond cleavage of m–diiodobenzene on Cu(110). The final state correspond to the imprinted I atom chemisorbed in the first available long bridge positions. The barrier equals 117 eV, hence, the asymmetry of the initial state facilitates the rupture of the first C–I bind with respect to the symmetric p– isomer.

REFERENCES

[1] C. Panosetti and W. A. Hofer. Adsorption of metadiiodobenzene on Cu(110): a theoretical study. *Journal of Computational Chemistry*, 33(19):1623–31, July 2012.

[2] L. Leung, T. B. Lim, J. C. Polanyi, and W. A. Hofer. Molecular calipers control atomic separation at a metal surface. *Nano Letters*, 11(10):4113–4117, 2011.

[3] L. Leung, T. Lim, Z. Ning, and J. C. Polanyi. Localized reaction at a smooth metal surface: p–diiodobenzene at Cu(110). *Journal of the American Chemical Society*, 134(22):9320–6, June 2012.

[4] P. Hohenberg and W. Kohn. Inhomogeneous electron gas. *Physical Review*, 136:B864–B871, 1964.

[5] W. Kohn and L. J. Sham. Self–consistent equations including exchange and correlation effects. *Physical Review*, 140:A1133–A1138, 1965.

[6] G. Kresse and J. Furthmüller. Efficiency of ab–initio total energy calculations for metals and semiconductors using a plane–wave basis set. *Computational Materials Science*, 6(1):15–50, 1996.

[7] G. Kresse and J. Furthmüller. Efficient iterative schemes for *ab initio* total–energy calculations using a plane–wave basis set. *Physical Review B*, 54:11169–11186, 1996.

[8] J. P. Perdew, K. Burke, and M. Ernzerhof. Generalized gradient approximation made simple. *Physical Review Letters*, 77:3865, 1996.

[9] J. P. Perdew, K. Burke, and M. Ernzerhof. Erratum: Generalized gradient approximation made simple. *Physical Review Letters*, 78:1396, 1997.

[10] P. E. Blöchl. Projector augmented–wave method. *Phys. Rev. B*, 50:17953–17979, 1994.

[11] G. Kresse and D. Joubert. From ultrasoft pseudopotentials to the projector augmented–wave method. *Physical Review B*, 59:1758–1775, 1999.

[12] P. Pulay. Convergence acceleration of iterative sequences. the case of scf iteration. *Chemical Physics Letters*, 73(2):393–398, 1980.

[13] S. Grimme. Semiempirical gga–type density functional constructed with a long–range dispersion correction. *Journal of Computational Chemistry*, 27(15):1787–1799, 2006.

[14] S. R. Bahn and K. W. Jacobsen. An object–oriented scripting interface to a legacy electronic structure code. *Comput. Sci. Eng.*, 4(3):56–66, 2002.

[15] D. Sheppard, R. Terrell, and G. Henkelman. Optimization methods for finding minimum energy paths. *The Journal of Chemical Physics*, 128(13):134106, April 2008.

[16] G. Henkelman, B. P. Uberuaga, and H. Jönsson. A climbing image nudged elastic band method for finding saddle points and minimum energy paths. *The Journal of Chemical Physics*, 113(22):9901, 2000.

[17] R. F. W. Bader. *Atoms in Molecules: A Quantum Theory (International Series of Monographs on Chemistry)*. Oxford University Press, USA, 1994.

Chapter 10

Supported Cu nanoclusters on Cu(110)

10.1 Introduction

As reviewed in Chapter 2 and reported throughout the present Thesis, Localized Atomic Reactions (LARs) have been a subject of growing interest in recent years. Halogenated hydrocarbons have been reported to easily react on silicon surfaces in a large number of studies [1–8], generally starting from a physisorbed template constituted by single molecules, pairs, or simple self–assembled structures such as lines. Providing energy in the form of heat, light, or electrons, the templates have been observed to react, efficiently and often cooperatively, resulting in chemisorbed halogen single atoms or patterns on the surface. The location of the chemisorbed products is invariably determined by the position and structure of the template molecule, thus defining such reactions as localized.

While this class of reactions has been widely reported, investigated and characterized on silicon surfaces, recently it has been found that they can occur also on Cu(110). The possibility of localized reaction on such a smooth surface represents a novelty that opens new routes to surface functionalization.

In 2011, L. Leung *et al.* show that 1,4–diiodobenzene on Cu(110) acts as a molecular caliper [9], that is, the linear size of the physisorbed template determines the separation of the two chemisorbed I atoms on the surface, once an imprinting reaction is electron–induced by means of the STM tip. At liquid Helium temperature (4.22 K), 1,4–diiodobenzene physisorbs on Cu(110) as a single molecule or chain polymers constituted by two or more units. If electrons are dropped onto the physisorbed template with the STM tip, only the teminal I atoms end up imprinted on the surface, with a narrow spatial distribution. Hence, the reaction is localized. This results has created interest on di–halobenzenes on Cu(110): 1,4–dichlorobenzene has been reported to show a similar behaviour, though with less marked localization ability [10], while the theoretical study of the adsorption geometries of 1,3–diiodobenzene carried out in

our group (see Chapter 8 and Ref. [11]) has shown that its most stable arrangement is asymmetric and may react with a different mechanism and outcome, as further investigated in Chapter 9. Generally speaking, however, halogenated hydrocarbons on Cu(110) or other smooth metal surfaces, being able to undergo Localized Atomic Reactions thanks to the facility of C–X bond cleavage, represent a class of systems with great potential and the endless possibilities are yet to be explored.

Starting from this novel findings, we make the ansatz that single atoms imprinted on a Cu(110) surface via Localized Atomic Reaction may be used to support more complex structures, such as metal nanoclusters, on smooth metal surfaces.

Metal nanoclusters supported on metal oxides are widely established and well characterized due to their extensive employment in catalysis (see, for instance, Ref. [12]), while the decoration of metal electrodes with metal structures has also been achieved with the aid of a Scanning Tunneling Microscope [13–16]. However, to the best of our knowledge, no copper–on–copper structures supported by atoms of different species have been reported, neither experimentally nor theoretically.

In the present work, the existence of three–dimensional Cu nanostructures on Cu(100) is theoretically predicted. The aim of the present work is to evaluate the thermodynamic effect of one or two S (or Cl) adatoms in supporting and stabilizing those structures.

Sulphur is already commonly employed as an anchor for Self–Assembled Monolayers (SAMs) on copper or gold electrodes for the fabrication of biosensors (see, for example, Ref. [17]).

Sulphur can be layered on a Cu(110) surface, for instance, by depositing methanethiol or hydrogen sulphide which then decompose at room temperature leaving S atoms on the surface [18–22]. The chemisorption of sulphur on copper has been extensively studied (see, for example, the work by Carley *et al* [20, 21, 23]) due to the fact that, being one of the most common impurities of copper, sulphur poisoning causes deactivation of copper–based catalysts [24].

At low coverage, sulphur adatoms are mobile at room temperature, forming c(2×2) structures only above a surface concentration of approximately $3.8 \cdot 10^{14}$ cm^{-2} or below in presence of oxygen. At higher coverages, or under the presence of oxygen, different reconstructions have been observed depending on the coverage [20].

In the light of this, one can imagine a process such that sulphur precursors are deposited on a Cu(110) surface at very low coverage at room temperature, which then spontaneously decompose leaving isolated adatoms. Since single sulphur atoms would diffuse at room temperature, in order to achieve a sparse and local patterning of the surface, the sample may be cooled down at liquid helium temperature.

10.2 Theory

10.2.1 Theoretical setup

All calculations were performed using DFT [25, 26] as implemented in VASP 5.2.11 [27, 28]. Projected Augmented Wave [29, 30] and PBE functionals [31, 32] were employed. All structures were pre–converged using a cutoff of 280 eV and subsequently refined with a cutoff of 400 eV in order to obtain accurate energies. Van der Waals interactions were included using Grimme's DFT–D method [33].
Structural relaxation was carried out with a Conjugate Gradient (see, for instance, Ref. [34]) minimization algorithm until the forces acting on each atom were smaller than 0.02 Å.
A supercell of 5×5 atoms and 4 layers was chosen. The two uppermost layers were allowed to relax together with the adsorbates,, while the two bottom layers were kept frozen. The clean surface was generated with the ASE package employing a lattice constant optimized in a previous work [11] (see Chapter 8).
Due to the sufficiently large size of the supercell, and in order to save computational time, the Brillouin zone was sampled using the Γ point only. The supercell was chosen large enough to rule out the effect of self–interaction due to boundary conditions, since in a high–coverage regime three–dimensional structures may be stabilized merely by surface crowding.

10.2.2 Stability and stabilization

In order to understand the role of adatoms in the structures of interest, an important distinction between stability and stabilization must be made. The stability of the 3D structure is defined as its adsorption energy, that is, the difference between the electronic energy of the structure with respect to the reference substrate, which is, in this case, a Cu(110) surface functionalized with a S atom adsorbed in the four–fold hollow position. The adsorption energy is hence calculated as

$$E_{\mathrm{ads,anchored}} = (E_{\mathrm{SCu_n/surf}} - E_{\mathrm{S/surf}} - E_{\mathrm{Cu_n,vac}})/n \ , \tag{10.1}$$

where $E_{\mathrm{SCu_n/surf}}$ and $E_{\mathrm{S/surf}}$ are the output VASP energies of, respectively, the structure and the substrate. $E_{\mathrm{Cu_n,vac}}$ is the energy of a $\mathrm{Cu_n}$ cluster in vacuum. For the sake of comparison, the value is normalized with respect to the size n of the cluster.
Accordingly, the stability of the corresponding unanchored structure is calculated with respect to its respective substrate, constituted by a clean Cu(100) surface, and is hence given by

$$E_{\mathrm{ads,unanchored}} = (E_{\mathrm{Cu_n/surf}} - E_{\mathrm{surf}} - E_{\mathrm{Cu_n,vac}})/n \tag{10.2}$$

On the other hand, the quantity of major interest to the purpose of this paper is the stabilization, that is, the actual effect of the adatom in stabilizing the structure. We may define the latter as the difference between 10.1 and 10.2, that is:

$$E_{\mathrm{stab}} = E_{\mathrm{ads,anchored}} - E_{\mathrm{ads,unanchored}} = \tag{10.3}$$

$$= (E_{\mathrm{SCu_n/surf}} - E_{\mathrm{Cu_n/surf}} - E_{\mathrm{S/surf}} + E_{\mathrm{surf}})/n \ . \tag{10.4}$$

All the energy values are obtained from VASP. Since we are comparing systems of different compositions, particular care must be taken in order to minimize computational errors.
In the calculation of adsorption energies, two strategies are possible:

- calculate (a) the electronic energy of the substrate/adsorbate complex, (b) the electronic energy of the isolated adsorbate in vacuum using the same supercell and the same cutoff, (c) the electronic energy of the clean substrate using the same supercell and the same cutoff. With this method, $E_{\mathrm{ads}} = (a) - (b) - (c)$. This method tends to *overestimate* the true adsorption energy.

- desorption method: calculate (a) the electronic energy of the substrate/adsorbate complex, (b) the electronic energy of the surface with, in the same supercell, the adsorbate placed at a distance sufficiently large to assume the interaction has vanished. This is best achieved performing several single–point calculations with the adsorbate fixed at increasing heights, until a plateau is reached, giving (b). Within this method, $E_{\mathrm{ads}} = (a)-(b)$. This method tends to slightly *underestimate* the true adsorption energy, as residual interaction may still be present.

Throughout the present work, we have employed the desorption method. Hence, we computed the quantity $(E_{\mathrm{S/surf}} + E_{\mathrm{Cu_n,vac}})$, and, accordingly, $(E_{\mathrm{surf}} + E_{\mathrm{Cu_n,vac}})$, in a single run. This implies that, in the Equation 10.4, cancelling out $E_{\mathrm{Cu_n,vac}}$ is in principle exact, but it introduces a small error on the difference $(E_{\mathrm{S/surf}} - E_{\mathrm{surf}})/n$, even assuming that every output VASP energy is accurate enough to be considered exact. This small error is solely ascribable to the approximation of the adsorption energy and it cannot be estimated.
However, bearing in mind that, by definition:

$$-E_{\mathrm{S/surf}} + E_{\mathrm{surf}} = -E_{\mathrm{ads,S}} \ , \tag{10.5}$$

we may now work out Eqn. 10.4 to obtain:

$$E_{\mathrm{stab}} = (E_{\mathrm{SCu_n/surf}} - E_{\mathrm{Cu_n/surf}} - E_{\mathrm{ads,S}})/n \ , \tag{10.6}$$

where, still assuming that the output VASP energies $E_{\mathrm{SCu_n/surf}}$ and $E_{\mathrm{Cu_n/surf}}$ are exact, we may now conclude that, calculating $E_{\mathrm{ads,S}}$ with the desorption method, our stabilization energies are subject to a small error of the order of $(E^{\mathrm{CALC}}_{\mathrm{ads,S}} - E^{\mathrm{TRUE}}_{\mathrm{ads,S}})/n$, which is negative, from which it follows that the computed stabilization energies are slightly overestimated.

10.3 Results and discussion

We have considered the adsorption energies of 3–dimensional nanostructures ranging from 2 to 7 Cu atoms in size, divided in two classes which we shall from now one define as "anchored", that is, presenting a sulphur adatom placed in the centre of the structure, and "confined", that is, presenting two sulphur adatoms placed on each side of the structure, along the [001] surface axis. Clearly, the chosen structures are only few of the possible $\mathrm{Cu_n}$–$\mathrm{S_m}$/Cu(110) arrangements, as, for instance, S adatoms may be placed along different directions, or increased in number in order to form corrals.
We have placed the S adatoms in the four–fold hollow positions, due to the fact that sulphur adatoms on Cu(110) preferentially chemisorb on that site [35]. The choice of the initial guesses was dictated by chemical intuition and symmetry arguments, that is, for the S–centred structures the Cu atoms forming the 3–dimensional cage were placed around the anchor symmetrically in order to limit distortions of the substrate, while for the confined structures the 3–dimensional structures were built atom–by–atom such as the resulting structures were more compact than the corresponding anchored ones. Additional details are reported in Appendix D.
For each structure, we compared the computed ground energies of the supported and non–supported three–dimensional structures, that is, after the supported structure was converged, we removed the anchor(s) and let the system relax.
The obtained results are illustrated and discussed in the following Sections. The choice of sulphur over chlorine or iodine will be clarified in Appendix D.

10.3.1 Gas–phase clusters

The structures of the gas–phase $\mathrm{Cu_n}$ clusters employed as a reference are reported in Figure 10.1. For sizes for which more than one structure is possible, that is, for $n > 3$, we have chosen the structure which is, in the gas–phase, most similar to the geometry of the on–surface aggregate, that is, the planar or capped structures for singly–anchored aggregates, and the diamond–like structures for the doubly–anchored aggregates, in order to minimize the effect of atomic rearrangement. Of course, this choice is somewhat arbitrary, but in most cases the computed energy difference between any of the most stable structures and their corresponding second stable structure is small enough to safely disregard the geometry of the gas–phase reference cluster (see Appendix D).

10.3.2 Anchored clusters

We have investigated structures supported by a single sulphur atom, chemisorbed in the four–fold hollow position of the Cu(110) surface, by placing from 2 to 7 additional copper atoms around the core sulphur.

Structure

The optimized structures for 3D Cu aggregates around one single S atom, centred in the four–fold hollow position, are shown in Figure 10.2. It appears evident that such aggregates do present 3–dimensional features, especially the odd–number sized ones, but are, undesirably, rather "sparse", to the extent that they may be not be defined as clusters. In other words, it is not possible to accommodate a central adatom inside a small cluster. This is due to the fact that such small copper clusters, also in the gas phase, do not stabilize in the form of cage–like structures large enough to endohedrally host additional atoms, similarly to, for example, the fullerene–like stuctures formed by tetragens, which are known to do so (see, for example, Refs. [36–40]. Further scrutiny may be appropriate in order to determine whether larger copper structures, which are certainly able to form cage–like structures (see, for example, Ref. [41]), are also able to be endohedrally doped.
In general, the construction of singly–anchored Cu–on–Cu structures is not trivial; further details will be given in Appendix D.

Energetics

The adsorption and stabilization energies of the structures of the structures shown in Figure 10.2 are reported in Table 10.1 and plotted in Figure 10.3.
Regardless of the size of the clusters, the formation energies are fairly large, of the order of ∼1–2 eV per Cu atom. Stabilization energies, on the other hand, are mostly negative, indicating that the anchored structures are not thermodynamically[1] favoured with respect to the unanchored ones. However, since both anchored and unanchored structures have a large thermodynamic stability, here, the central adatom may still play a role in stabilizing the structures by increasing the diffusion barrier of copper atoms away from the centre of the cluster. This hypothesis provides grounds for further investigation.
Further, the plot with respect to the cluster size n shows an oscillating feature, due to the fact that structures corresponding to odd values of n present an apical Cu atom

[1] We are here neglecting the effect of entropy. This approximation is justified by the fact that these systems are intended to be designed at low temperature, since the Localized Atomic Reaction experiments on smooth metal surface were carried out at liquid helium temperature. Of note, at low temperatures, the system is dominated by kinetics rather than energetics, which may rise the argument that energetic calculations are unsubstantial. However, before performing a kinetic characterization of the system, such as the investigation of how long–lived the superatomic structures are if subject to diffusion, it is desirable to determine whether the proposed structures exist at all.

which, if unanchored, pops into the gap upon structural relaxation, resulting in a more stable arrangement (see Figure 10.4). This is yet another indication that "hollow" structures capable of hosting additional atoms are unlikely for the sizes at issue.
As expected, the stabilization energy vanishes rapidly with increasing size of the clusters, as the interaction is short ranged.

10.3.3 Confined clusters

In addition to structures supported by a single sulphur adatom, we have investigated structures supported by two sulphur atoms, chemisorbed in four–fold hollow sites of the Cu(110) surface to each side of the clusters along the [001] direction.

Structures

The optimized structures are shown in Figure 10.5. As opposite to the aggregates around a single adatom, this kind of design lacks the steric impediment constituted by the need to accommodate an endohedral dopant, as it is specifically tailored to be of the corraling type. Here, the existence of compact 3D structures on the surface is possible still retaining the "cluster" definition.
Structures from Cu_5 onward show indeed marked 3D features, being prominent over the surface by 3.91, 3.52 and 5.84 Å for $n = 5, 6, 7$ respectively.

Energetics

The adsorption and stabilization energies are reported in Table 10.2 and shown in Figure 10.3.
Similarly to the anchored clusters, formation energies of the confined clusters are large and of the same order as anchored clusters, with little variation with respect to the cluster size. As opposed to the rather discouraging results for anchored clusters, confined clusters are "well behaved", that is, the effect of the single adatoms is indeed that of stabilizing the final structure.
In the case of the Cu_2 structure, the stabilization energy is negative due to the fact that the corresponding unanchored structure is unstable, that is, starting from a guess constituted by the already converged anchored structure with subsequent removal of the anchors, upon relaxation the two Cu atoms forming the structure "diffuse" to adjacent four–fold hollow position, resulting in a much more stable arrangement. An upper estimate of what would be the stabilization energy was obtained by means of a single–point calculation of the initial guess structure.
In this case, further, probably due to the removal of the geometric issue implicitly related to the anchored clusters. the stabilization is positive for both even and odd values of n. Moreover, the stabilization still decreases with increasing size of the clusters, but vanishes less rapidly than in the anchored case. It is reasonable to infer, by

extrapolation, that the normalized stabilization energy actually converges to a nonzero value.

Therefore, in pursuing the idea of creating 3D metal structures on a smooth metal surface, this second approach appears more viable. Of course, one can imagine to tailor the features of the superatomic aggregates by, for example, varying the number of confining atoms, or their arrangement, or both, from two to an arbitrarily large corral.

10.4 Conclusions

We have modelled copper nanoclusters on Cu(110), stabilized by one or two sulphur adatoms chemisorbed on the surface.The present study addresses solely the geometry and energetics of the proposed systems; however, once established that such structures exist, their kinetic stability is to be investigated.

We find that, constructing copper aggregates in size ranging from 2 to 7 copper atoms around a single chemisorbed sulphur atom, it is not trivially possible to achieve "compact" structures that can be properly defined as clusters. However, said structures do exist within the chosen theoretical framework, even though the role of the central atom is not relevant in energetically stabilizing the superatomic structure.

Conversely, copper aggregates of the same size range confined by two sulphur atoms placed along the [001] surface direction form compact 3D structures which retain the properties of clusters. Here, the stabilization due to the presence of the adatoms is positive for any investigated size and vanishes slowly with increasing size of the cluster.

We may conclude that, in the perspective of the bottom–up design of tailored functionalized metal surfaces, the "confining" approach appears thus more viable. One can imagine to adjust the geometry and stability of the superatomic aggregates by, for example, varying the number and/or the arrangement of the confining atoms, from two to an arbitrarily large corral.

10.5 Figures and tables

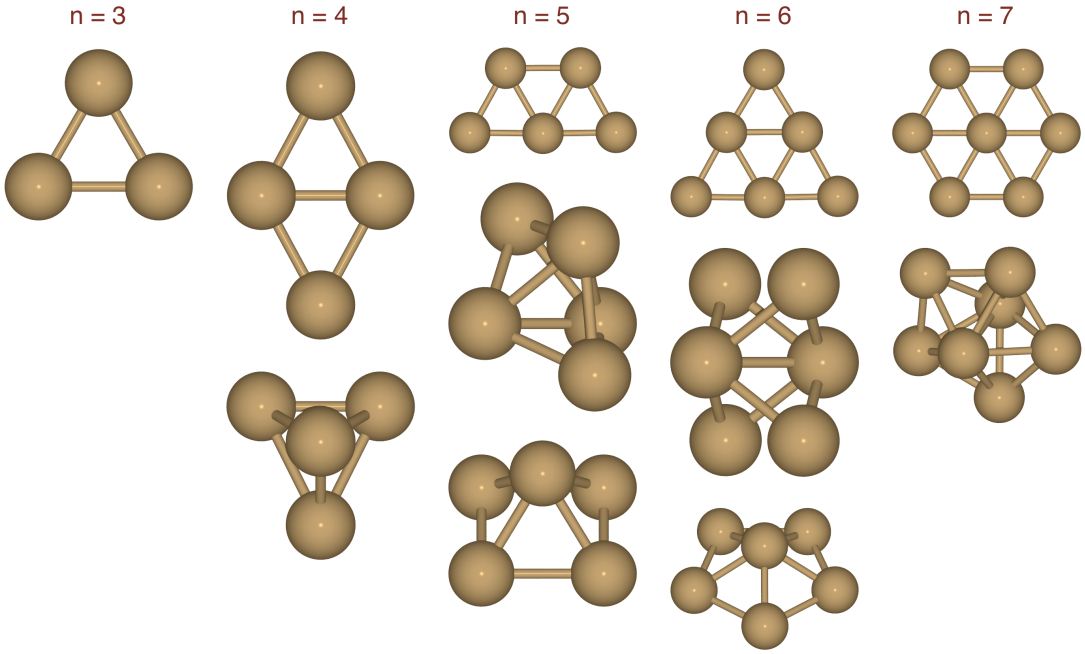

Figure 10.1: Structures of gas–phase Cu clusters ranging from 3 to 7 Cu atoms in size. For $n = 4$: planar (top) and tetrahedral (bottom). For $n = 5$: planar (top), diamond (middle) and capped (bottom). For $n = 6$: planar† (top), diamond‡ (middle) and capped (bottom). For $n = 6$: planar† (top), diamond‡ (middle) and capped (bottom). For $n = 7$: planar† (top) and diamond‡ (bottom). The superscripts † and ‡ mark structures taken as a reference for singly– and doubly–supported aggregates respectively.

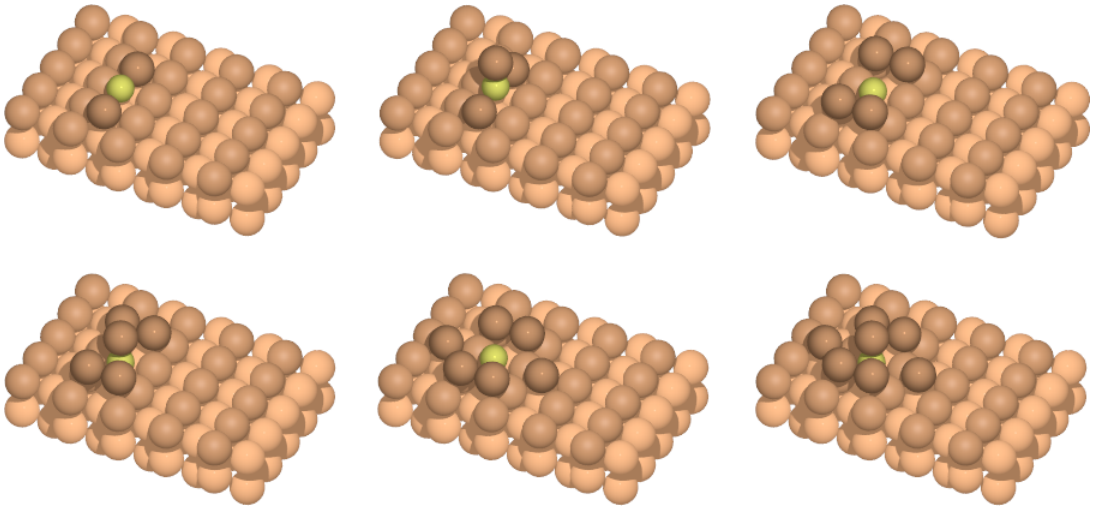

Figure 10.2: Optimized structures of Cu nanoclusters on Cu(110) anchored by a single S adatom chemisorbed in the 4–fold–hollow position. Cluster size ranges from 2 to 7 Cu atoms. For clarity, the S atom is coloured in yellow. The surface slab is rendered in semi–transparent copper colour, with the copper rows along the [1$\underline{1}$0] direction evidenced in a darker shade. The copper and sulphur atoms forming the 3D structure are rendered in full colour. The structures are, undesirably, rather sparse.

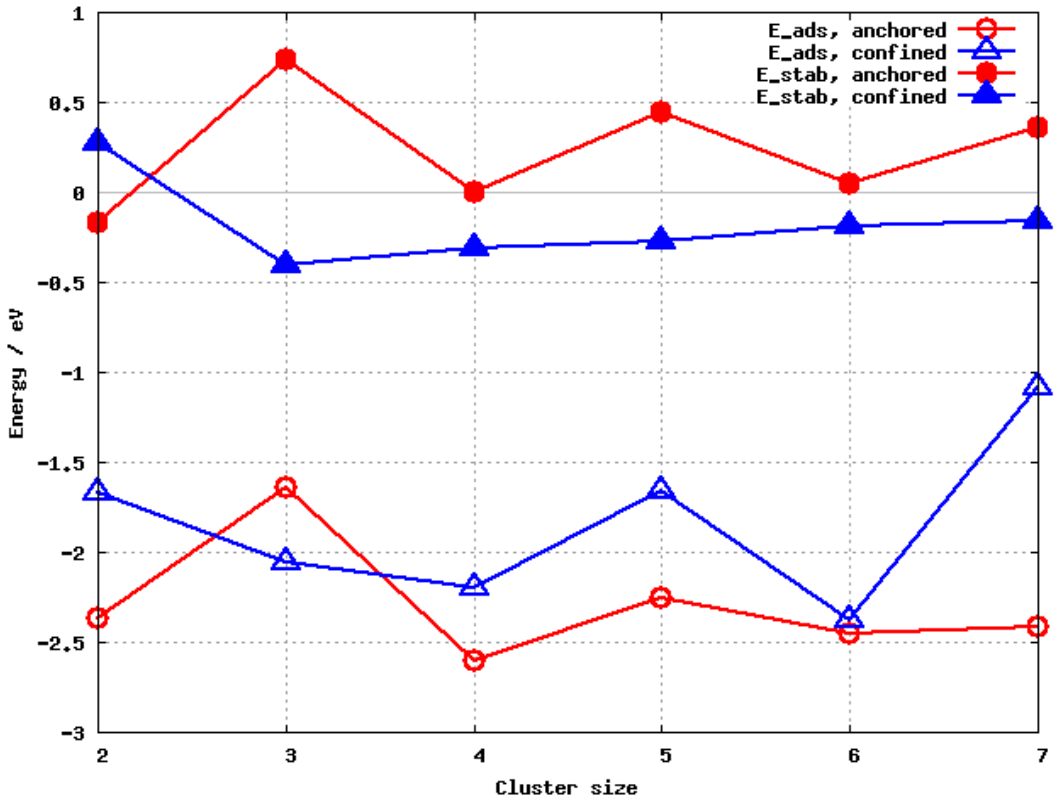

Figure 10.3: Adsorption and stabilization energies of singly– and doubly–anchored Cu clusters on Cu(110) with respect to the cluster size ranging from 2 to 7. All the energies are normalized to the cluster size.

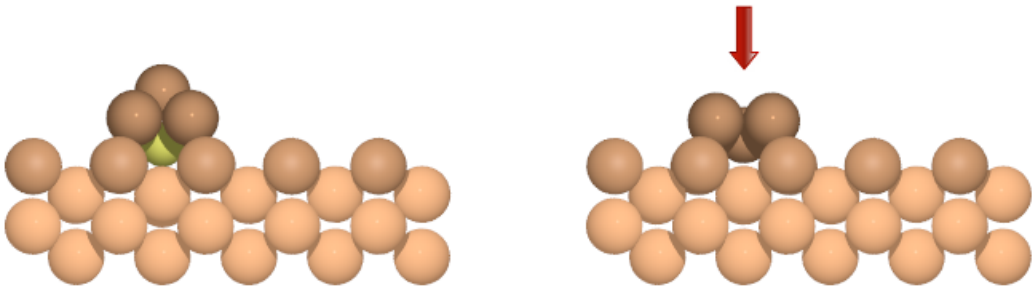

Figure 10.4: Schematic showing that, for odd values of the size of the singly anchored clusters, once removed the anchor the apical Cu atom fills the subsequent gap, resulting in a more stable structure.

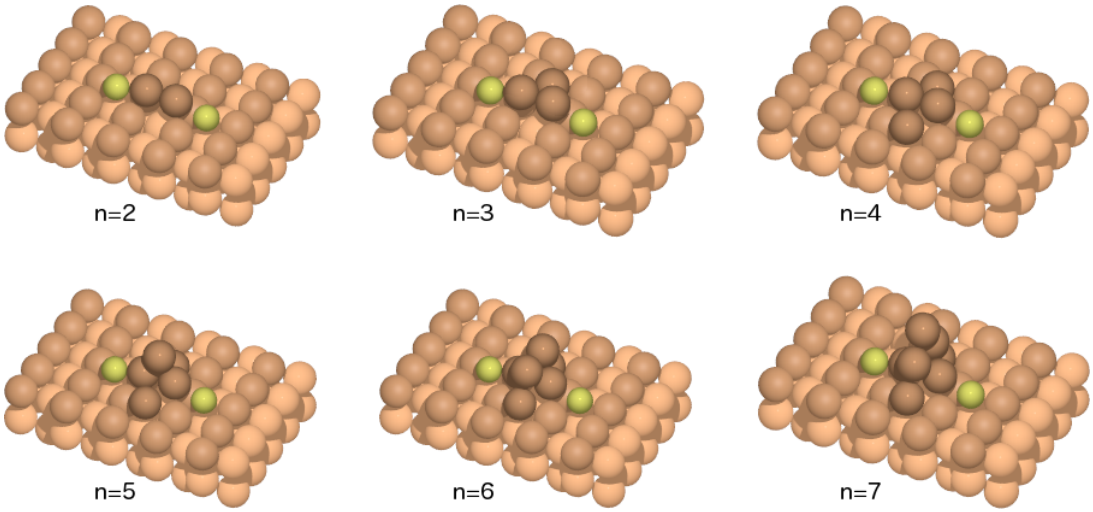

Figure 10.5: Optimized structures of Cu nanoclusters on Cu(110) confined between two S adatoms chemisorbed in the adjacent 4–fold–hollow positions. Cluster size ranges from 2 to 7 Cu atoms. For clarity, the S atom is coloured in yellow. The surface slab is rendered in semi–transparent copper colour, with the copper rows along the [1$\underline{1}$0] direction evidenced in a darker shade. The copper and sulphur atoms forming the 3D structure are rendered in full colour. The structures from 5 to 7 Cu atoms show marked 3D features.

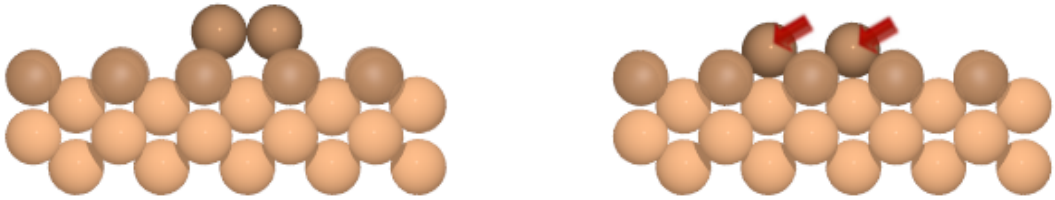

Figure 10.6: Schematics showing that, for the "confined" Cu_2 cluster, the corresponding unanchored structure is unstable, as upon relaxation it evolves in a structure such that the two atoms are no longer bound but rather sitting in adjacent four–fold hollow surface sites.

n	2	3	4	5	6	7
E_{ads} / eV	–2.369	–1.642	–2.603	–2.252	–2.452	–2.419
E_{stab} / eV	–0.166	0.733	0.003	0.445	0.044	0.361

Table 10.1: Formation energies and stabilization energies of singly–anchored Cu aggregates.

n	2	3	4	5	6	7
E_{ads} / eV	–1.668	–2.052	–2.194	–1.660	–2.377	–1.085
E_{stab} / eV	0.270	–0.405	–0.309	–0.275	–0.192	–0.160

Table 10.2: Formation energies and stabilization energies of doubly–anchored (or "confined") Cu aggregates.

REFERENCES

[1] I. R. McNab and J. C. Polanyi. Patterned atomic reaction at surfaces. *Chemical Reviews*, 106(10):4321–4354, 2006.

[2] K. R. Harikumar, I. R. McNab, J. C. Polanyi, A. Zabet-Khosousi, and W. A. Hofer. Imprinting self–assembled patterns of lines at a semiconductor surface, using heat, light, or electrons. *Proceedings of the National Academy of Science*, 108(3):950–955, 2010.

[3] K. R. Harikumar, I. R. McNab, J. C. Polanyi, A. Zabet-Khosousi, C. Panosetti, and W. A. Hofer. Stereo–isomerism controls surface reactivity: 1–chloropentane–pairs on Si(100)–2×1. *Chemical Communications*, 47:12101–12103, 2011.

[4] K. R. Harikumar, L. Leung, I. R. McNab, J. C. Polanyi, H. Lin, and W. A. Hofer. Cooperative molecular dynamics in surface reactions. *Nature Chemistry*, 1(9):716–21, 2009.

[5] K. R. Harikumar, T. Lim, I. R. McNab, J. C. Polanyi, L. Zotti, S. Ayissi, and W. A. Hofer. Dipole–directed assembly of lines of 1,5–dichloropentane on silicon substrates by displacement of surface charge. *Nature Nanotechnology*, 3(4):222–8, 2008.

[6] P. H. Lu, J. C. Polanyi, and D. Rogers. Electron–induced 'Localized Atomic Reaction' (LAR): Chlorobenzene adsorbed on Si(111)–7×7. *The Journal of Chemical Physics*, 111(22):9905, 1999.

[7] S. Dobrin, K. R. Harikumar, and J. C. Polanyi. An STM study of the localized atomic reaction of 1,2– and 1,4–dibromobenzene at Si(111)–7×7. *Surface Science*, 561(1):11–24, 2004.

[8] S. Dobrin, K. R. Harikumar, C. F. Matta, and J. C. Polanyi. An STM study of the localized atomic reaction of 1,2– and 1,4–dibromoxylene with Si(111)–7×7. *Surface Science*, 580:39–50, 2005.

[9] L. Leung, T. Lim, J. C. Polanyi, and W. A. Hofer. Molecular calipers control atomic separation at a metal surface. *Nano Letters*, 11(10):4113–4117, 2011.

[10] A. Eisenstein, L. Leung, T. Lim, Z. Ning, and J. C. Polanyi. Reaction dynamics at a metal surface; halogenation of Cu(110). *Faraday Discussions*, 157(110):337, 2012.

[11] C. Panosetti and W. A. Hofer. Adsorption of metadiiodobenzene on Cu(110): a theoretical study. *Journal of Computational Chemistry*, 33(19):1623–31, 2012.

[12] B. C. Gates. Supported metal clusters: Synthesis, structure, and catalysis. *Chemical Reviews*, 95(3):511–522, 1995.

[13] R. Ullmann, T. Will, and D. M. Kolb. Nanoscale decoration of Au(111) electrodes with Cu clusters by an STM. *Chemical Physics Letters*, 209(3):238–242, 1993.

[14] D. M. Kolb. Nanofabrication of Small Copper Clusters on Gold(111) Electrodes by a Scanning Tunneling Microscope. *Science*, 275(5303):1097–1099, 1997.

[15] D Kolb. Nanoscale decoration of electrode surfaces with an STM. *Solid State Ionics*, 131(1-2):69–78, 2000.

[16] D. M. Kolb and F. C. Simeone. Electrochemical nanostructuring with an STM: a status report. *Electrochimica Acta*, 50(15):2989–2996, 2005.

[17] J. C. Love, L. A. Estroff, J. K. Kriebel, R. G. Nuzzo, and G. M. Whitesides. Self-assembled monolayers of thiolates on metals as a form of nanotechnology. *Chemical Reviews*, 105(4):1103–1170, 2005.

[18] J. L. Domange and J. Oudar. Structure et conditions de formation de la couche d'adsorption du soufre sur le cuivre. *Surface Science*, 11(1):124–142, 1968.

[19] M. Kostelitz and J. Oudar. Éude thermodynamique et structurale de l'adsorption dans le système or–soufre. *Surface Science*, 27(1):176–190, 1971.

[20] A. F. Carley, P. R. Davies, R. V. Jones, K. R. Harikumar, G. U. Kulkarni, and M. W. Roberts. The structure of sulfur adlayers at Cu(110) surfaces: an STM and XPS study. *Surface Science*, 447(1-3):39–50, 2000.

[21] A. F. Carley, P. R. Davies, R. V. Jones, K. R. Harikumar, and M. W. Roberts. An STM and XPS study of the chemisorption of methyl mercaptan at a Cu(110) surface. *Surface Science*, 490(1-2):L585–L591, 2001.

[22] J. G. Lee and J. T. Yates. Methanethiol chemisorption on Cu(110): chemical and geometrical issues related to self–assembly. *The Journal of Physical Chemistry B*, 107(38):10540–10545, 2003.

[23] A. F. Carley, P. R. Davies, R. V. Jones, K. R. Harikumar, G. U. Kulkarni, and M. W. Roberts. Structural aspects of chemisorption at Cu(110) revealed at the atomic level. *Topics in Catalysis*, 12:299–306, 2000.

[24] M. V. Twigg and M. S. Spencer. Deactivation of supported copper metal catalysts for hydrogenation reactions. *Applied Catalysis A: General*, 212(1-2):161–174, 2001.

[25] P. Hohenberg and W. Kohn. Inhomogeneous electron gas. *Physical Review*, 136(3B):B864–B871, 1964.

[26] W. Kohn and L. J. Sham. Self–consistent equations including exchange and correlation effects. *Physical Review*, 140(4A):A1133–A1138, 1965.

[27] G. Kresse and J. Furthmüller. Efficiency of ab–initio total energy calculations for metals and semiconductors using a plane–wave basis set. *Computational Materials Science*, 6(1):15–50, 1996.

[28] G. Kresse and J. Furthmüller. Efficient iterative schemes for *ab initio* total–energy calculations using a plane–wave basis set. *Physical Review B*, 54:11169–11186, 1996.

[29] P. E. Blöchl. Projector augmented–wave method. *Physical Review B*, 50:17953–17979, 1994.

[30] G. Kresse and D. Joubert. From ultrasoft pseudopotentials to the projector augmented–wave method. *Physical Review B*, 59:1758–1775, 1999.

[31] J. P. Perdew, K. Burke, and M. Ernzerhof. Generalized gradient approximation made simple. *Physical Review Letters*, 77:3865, 1996.

[32] J. P. Perdew, K. Burke, and M. Ernzerhof. Erratum: Generalized gradient approximation made simple. *Physical Review Letters*, 78:1396, 1997.

[33] S. Grimme. Semiempirical GGA–type density functional constructed with a long–range dispersion correction. *Journal of Computational Chemistry*, 27(15):1787–1799, 2006.

[34] W. H. Press, S. A. Teukolsky, W. T. Vetterling, and B. P. Flannery. *Numerical Recipes 3rd Edition: The Art of Scientific Computing*. Cambridge University Press, New York, NY, USA, 3 edition, 2007.

[35] X. Y. Pang, L. Q. Xue, and G. C. Wang. Adsorption of atoms on Cu surfaces: a density functional theory study. *Langmuir*, 23(9):4910–7, 2007.

[36] H. Shinohara. Endohedral metallofullerenes. *Reports on Progress in Physics*, 63(6):843, 2000.

[37] C. L. Lieber and C. C. Chen. Preparation of fullerenes and fullerene–based materials. volume 48 of *Solid State Physics*, pages 109–148. Academic Press, 1994.

[38] K. Jackson and B. Nellermoe. $Zr@Si_{20}$: a strongly bound Si endohedral system. *Chemical Physics Letters*, 254(3-4):249–256, 1996.

[39] H. Hiura, T. Miyazaki, and T. Kanayama. Formation of metal–encapsulating Si cage clusters. *Physical Review Letters*, 86(9):1733–1736, 2001.

[40] V. Kumar and Y. Kawazoe. Metal–encapsulated fullerenelike and cubic caged clusters of silicon. *Physical Review Letters*, 87(4):045503, 2001.

[41] M. Kabir, A. Mookerjee, and A. Bhattacharya. Structure and stability of copper clusters: A tight–binding molecular dynamics study. *Physical Review A*, 69(4):1–10, 2004.

Chapter 11

Summary and conclusions

We have investigated the adsorption and reactivity of substituted hydrocarbons on silicon and copper surfaces using Grimme's vdW–corrected DFT, CI–NEB and STM simulations. Halogenated hydrocarbons drew great interest in the field of on–surface Single Molecule Chemistry due to their ability to adsorb and self–assembly at surfaces and subsequently undergo Localized Atomic Reactions (LARs). In other words, they easily react after being energized by means of heat, light, or electrons dropped with an STM tip, resulting in single, or patterns of, chemisorbed atoms at specific and controllable sites.

In Chapter 7, we focused on 1–chloropentane on Si(001)–2×1, which was experimentally found to form asymmetric (A) and symmetric (S) pairs. A and S pairs show different reactivity in both the thermal and electron–induced chlorination of the silicon surface, the reactivity of the asymmetric pair being about 15 times larger than the symmetric in the thermal case. We have employed DFT and Nudged Elastic Band tools to explain the features of this system and we simulated STM images in agreement with the experiments. A and S are observed on the surface in equal proportion, suggesting that they have the same adsorption energy. The pairs have been observed to interconvert with an activation barrier of ~ 0.8 eV. Furthermore, A locally pins the surface in a c–(4×2) reconstruction, while S locally pins it in a p–(2×2) reconstruction. We found that, consistently with the experimental observation, the choice of the correct local pinning of the silicon surface correctly yields equal adsorption energies. We also calculated the interconversion barrier, which we find underestimated due to the fact that we did not include the dimer flipping in the calculations. However, accounting for the additional energy required to switch between c–(4×2) and p–(2×2) reconstruction for five silicon dimers adjacent to the adsorbates, we are able to recover an upper estimate of the activation energy in agreement with the experimental observations.

In Chapter 8, we focused on the theoretical modelling of the adsorption of 1,3–, or m–diiodobenzene on Cu(110) by means of Density Functional Theory including dispersion interaction using Grimme's method. Diiodobenzenes were shown in experimental works

by Prof. J. Polanyi's group at University of Toronto to be able to undergo Localized Atomic Reaction on smooth metal surface similarly to the well known class of halogenated hydrocarbons on silicon surfaces. We have compared the adsorption energies and structures of 23 possible configurations of the adsorbed molecule, finding that all the orientations have comparable energies, which leads the prediction that the relative probabilities of observing them experimentally tend to the same order of magnitude at high temperatures, while at low temperatures a strong preference for the two most stable arrangements is expected. We find that the asymmetric configurations are generally favoured. The analysis of the electronic structure allows to rule out the possibility of chemisorption. For B5x and A5x* an adsorption–induced symmetry breakdown occurs which may affect their reactivity, as we further investigated in Chapter 9. Furthermore, we have simulated STM images for the four most stable configurations using the Tersoff–Hamann approach at different bias voltages. Focusing in particular on the two most stable configurations B3x and B5x, which are very close in energy and provide very similar STM images, we noted that we are however able to distinguish the two by closely investigating both the computed structures and STM images, highlighted by plotting linescans along the [001] direction of the lattice and through the positions of the I atoms. Furthermore, there is evidence that the most stable arrangement is actually a bistable system (B5x/B3x, or asymmetric/symmetric).

In Chapter 9, we unambiguously clarified that the real ground adsorption configuration of m–diiodobenzene on Cu(110) is actually the one we labelled B5x, that is, asymmetric, as by attempting to compute the conversion barrier of the B3x/B5x bistable system hypothesized in Chapter 8, we find a barrierless transition from the symmetric arrangement to the asymmetric one, indicating that the latter is stable. In the light of this, we have compared the electronic ground–state reaction paths of the first C–I bond cleavage for m– and p–diiodobenzene on Cu(110), in order to investigate the effect of symmetry on the on–surface reactivity of the two isomers. Namely, while 1,4–, or p–diiodobenzene physisorbs on Cu(110) in a symmetric configuration, its meta isomer was found by our simulations to physisorb preferentially in an asymmetric arrangement. We find that, while the first C–I bond cleavage of p–diiodobenzene presents a barrier of 640 meV, is asymmetric counterpart m–diiodobenzene, possessing one C–I bond that is already strongly polarized due to internal partial charge rearrangement upon adsorption, presents a barrier of only 117 meV. Therefore, for m–diiodobenzene, in a ground state picture, the reactivity is remarkably influenced by the broken symmetry of the initial state. This may lead to the fact that, on the one hand, the reaction may lose cooperativity, or even occur for only one C–I bond, thus imprinting one single I atom on the surface in lieu of two, but on the other hand the facility of the bond cleavage is strongly enhanced with respect to the symmetric template. This implies that it is possible, in principle, not only to tune the I–I separation at the surface by choosing the

appropriate length of the initial chain of p–diiodobenzene molecule, but also to choose whether to imprint two or one I atoms on the surface by selecting the desired molecular template.

Finally, since the studied systems provide a means to surface functionalization via site–specific imprinting of single atoms, in Chapter 10, we predict the existence of three–dimensional metal aggregates at a smooth metal surface, in the form of copper nanoclusters on Cu(110) stabilized by one or two sulphur, or halogen adatoms preventively chemisorbed on the surface. By preliminary calculations, we determined that sulphur is the most promising candidate "anchor", among the the considered Cl, I, S. We find that copper aggregates in size ranging from 2 to 7 copper atoms around a single chemisorbed sulphur atom do not trivially yield "compact" structures that can be properly defined as clusters. However, said structures do exist within the chosen theoretical framework, even though the role of the central atom is not relevant in energetically stabilizing the superatomic structure. Conversely, we find copper aggregates of the same size range confined by two sulphur atoms to form compact cluster–like structures with marked three–dimensional features. Here, the stabilization due to the presence of the adatoms is positive for any cluster size at issue. We may conclude that, in the perspective of the bottom–up design of tailored functionalized metal surfaces, the "confining" approach appears thus more viable. One can imagine to adjust the geometry and stability of the superatomic aggregates by, for example, varying the number and/or the arrangement of the confining atoms, from two to an arbitrarily large corral.

To sum up, a large number of studies, both experimental and theoretical, show that the class of substituted hydrocarbons is greatly promising due to their ability to allow control of on–surface reactivity at the very molecular level. Therefore, molecules of this kind offer a remarkably versatile toolbox for the local and patterned functionalization of both metal and semiconductor surfaces, with evident technological implications. In particular, the bottom–up tailoring of surface features at the nanoscale appears to be within grasp, offering endless possibilities, most of which are yet to be explored.

Appendix A

Complements of theory

A.1 Solution of the Schrödinger's equation for a periodic system.

Let us consider the Schrödinger equation for a free particle, that is, $V(\mathbf{r}) = 0$.

$$-\frac{\hbar^2}{2m}\nabla^2\psi_{\mathbf{k}}(\mathbf{r}) = \epsilon_{\mathbf{k}}\psi_{\mathbf{k}}(\mathbf{r}) \ , \tag{A.1}$$

whose eigenvectors are a set of plane waves

$$\psi_{\mathbf{k}}(\mathbf{r}) = \frac{1}{\sqrt{V}}e^{i\mathbf{kr}} \ , \tag{A.2}$$

where V is the volume of the system, with eigenvalues

$$\epsilon_{\mathbf{k}} = \frac{\hbar^2\mathbf{k}^2}{2m} \tag{A.3}$$

where $\mathbf{k}$ is the wavevector of the particle.
If electrons are subject to a periodic potential, *e.g.* when belonging to a crystal, periodic boundary condition can be defined. Let $\mathbf{A}_i = N_i\mathbf{a}_i$, with $i = 1 \div 3$, be translational vectors which leave the system unchanged, $\mathbf{a}_i$ being the lattice vectors of the crystal. Then, by definition of boundary conditions, the wave function will be invariant under translation by each one of them:

$$\psi_{\mathbf{k}}(\mathbf{r} + \mathbf{A}_i) = \psi_{\mathbf{k}}(\mathbf{r} + N_i\mathbf{a}_i) = \psi_{\mathbf{k}}(\mathbf{r}) \tag{A.4}$$

from which it follows that the exponentials $e^{i\mathbf{kA}_i}$ must be equal to unity, that is, the possible values which can be assumed by $\mathbf{k}$ are restricted (quantized) by the following relation:

$$\mathbf{kA}_i = N_i\mathbf{ka}_i = g_i 2\pi \quad \Rightarrow \mathbf{ka}_i = \frac{2\pi}{N_i}g_i \ ; g_i = 0, \pm1, \pm2, \dots \ . \tag{A.5}$$

Let us now define the reciprocal lattice vectors as

$$\mathbf{b}_1 = 2\pi \frac{\mathbf{a}_2 \times \mathbf{a}_3}{\mathbf{a}_1 \cdot (\mathbf{a}_2 \times \mathbf{a}_3)} = \frac{2\pi}{v_c} \mathbf{a}_2 \times \mathbf{a}_3 \tag{A.6}$$

and so on, which allows to rewrite the wavevector as

$$\mathbf{k} = \frac{g_1}{N_1}\mathbf{b}_1 + \frac{g_2}{N_2}\mathbf{b}_2 + \frac{g_3}{N_3}\mathbf{b}_3 \; . \tag{A.7}$$

In other words, from periodic boundary conditions follows the existence of a discrete mesh of allowed $\mathbf{k}$–points, uniformly distributed in reciprocal space. Each of these $\mathbf{k}$–points is associated with a small parallelepiped whose volume, for a small increment $\Delta\mathbf{k}_i = \gamma_i \mathbf{b}_i$, is

$$\Delta k = \Delta\mathbf{k}_1 \cdot (\Delta\mathbf{k}_2 \times \Delta\mathbf{k}_3) = \gamma_1\gamma_2\gamma_3(\mathbf{b}_1 \cdot \mathbf{b}_2 \times \mathbf{b}_3) = \gamma_1\gamma_2\gamma_3 v_r \; . \tag{A.8}$$

Using the properties of the reciprocal lattice, that is, the fact that the reciprocal lattice of the reciprocal lattice is the direct lattice, it can be shown that

$$v_r = \frac{(2\pi)^3}{v_c} \tag{A.9}$$

where v_c is the volume of the direct unit cell.
Keeping in mind that

$$\Delta\mathbf{k}_1\mathbf{a}_1 = \gamma_1\mathbf{b}_1\mathbf{a}_1 = \gamma_1 2\pi \frac{(\mathbf{a}_2 \times \mathbf{a}_3) \cdot \mathbf{a}_1}{v_c} = \gamma_1 2\pi = \frac{2\pi}{N_1}\Delta g_1 \tag{A.10}$$

$$\Rightarrow \gamma_1 = \frac{1}{N_1} \;\; \text{for} \Delta g_1 = 1 \; , \tag{A.11}$$

it follows that

$$\Delta k = \frac{(2\pi)^3}{N_1 N_2 N_3 v_c} = \frac{(2\pi)^3}{V} \; , \tag{A.12}$$

that is, the volume around one discrete mesh point is inversely proportional to the volume of the periodic supercell.

A.2 Density of States

The Density of States (DOS) is the number of states per energy interval, that is, the differential of states $d\nu$ in the energy interval between ϵ and $\epsilon + d\epsilon$:

$$D(\epsilon) = \frac{d\nu}{d\epsilon} \; . \tag{A.13}$$

The differential $d\nu$ is given by the surface of a sphere of radius k_ϵ multiplied by the differential volume in reciprocal space and divided by the volume around one $\mathbf{k}$–point:

$$d\nu = 2\frac{4\pi k_\epsilon^2 dk}{\Delta k} \; . \tag{A.14}$$

Bearing in mind that $k_\epsilon = (2m\epsilon/\hbar^2)^{1/2}$, from which it follows that $dk_\epsilon = (m/2\hbar^2\epsilon)^{1/2}d\epsilon$, we may rewrite

$$d\nu = 2\frac{4\pi k_\epsilon^2 dk}{\Delta k} = 2\frac{V}{(2\pi)^3}\frac{4\pi\cdot 2m\epsilon}{\hbar 2}\left(\frac{m}{2\hbar^2\epsilon}\right)^{1/2}d\epsilon = \frac{V}{2\pi^2}\left(\frac{2m}{\hbar^2}\right)^{3/2}\sqrt{\epsilon}d\epsilon \tag{A.15}$$

which means that the density of states of a free electron gas increases with the square root of the energy.

A.3 Hellmann-Feynman Theorem

Let us consider a system whose Hamiltonian $\hat{\mathcal{H}}_\lambda$ depends on a parameter λ. Let $|\psi(\lambda)\rangle$ be one of its normalized eigenvectors with eigenvalue $E(\lambda)$. Then:

Theorem V (Hellmann–Feynman Theorem)**.**

$$\frac{dE(\lambda)}{d\lambda} = \left\langle \psi(\lambda)\middle|\frac{d\hat{\mathcal{H}}_\lambda}{d\lambda}\middle|\psi(\lambda)\right\rangle . \tag{A.16}$$

Proof. We begin with the fact that, by definition:

$$E(\lambda) = \langle\psi(\lambda)|\hat{\mathcal{H}}_\lambda|\psi(\lambda)\rangle . \tag{A.17}$$

Differentiating both sides yields

$$\frac{dE(\lambda)}{d\lambda} = \left\langle \psi(\lambda)\middle|\frac{d\hat{\mathcal{H}}_\lambda}{d\lambda}\middle|\psi(\lambda)\right\rangle + \left\langle \frac{d\psi(\lambda)}{d\lambda}\middle|\hat{\mathcal{H}}_\lambda\middle|\psi(\lambda)\right\rangle + \left\langle \psi(\lambda)\middle|\hat{\mathcal{H}}_\lambda\middle|\frac{d\psi(\lambda)}{d\lambda}\right\rangle . \tag{A.18}$$

Since $|\psi(\lambda)\rangle$ is an eigenvector of $\hat{\mathcal{H}}_\lambda$, Equation. A.18 can be rewritten as

$$\frac{dE(\lambda)}{d\lambda} = \left\langle \psi(\lambda)\middle|\frac{d\hat{\mathcal{H}}_\lambda}{d\lambda}\middle|\psi(\lambda)\right\rangle + E(\lambda)\left\langle \frac{d\psi(\lambda)}{d\lambda}\middle|\psi(\lambda)\right\rangle + E(\lambda)\left\langle \psi(\lambda)\middle|\frac{d\psi(\lambda)}{d\lambda}\right\rangle = \tag{A.19}$$

$$= E(\lambda)\left(\left\langle \frac{d\psi(\lambda)}{d\lambda}\middle|\psi(\lambda)\right\rangle + \left\langle \psi(\lambda)\middle|\frac{d\psi(\lambda)}{d\lambda}\right\rangle\right) , \tag{A.20}$$

but from the normalisation condition follows that

$$\left\langle \frac{d\psi(\lambda)}{d\lambda}\middle|\psi(\lambda)\right\rangle + \left\langle \psi(\lambda)\middle|\frac{d\psi(\lambda)}{d\lambda}\right\rangle = 0 . \tag{A.21}$$

Hence, the term in brackets vanishes, which proves the Hellmann–Feynman Theorem. □

If the parameter λ is regarded as the coordinates of the nuclei, the Hellmann–Feynman theorem allows to calculate the intramolecular forces in molecules using classical electrostatics once the electron density has been determined.

A.4 Corrections for van der Waals forces

DFT does not natively include dispersion forces. A common workaround consists in adding a semi–empirical dispersion potential to the conventional DFT energy. In Grimme's model, the dispersion interaction is mimicked by a pair potential and the energy correction assumes the form

$$E_{\text{disp}} = -s_6 \sum_{i=1}^{N-1} \sum_{j=i+1}^{N} \frac{C_6^{ij}}{R_{ij}^6} f_{\text{dmp}}(R_{ij}) \tag{A.22}$$

where N is the number of atoms in the system, C_6^{ij} is the dispersion coefficient for atom pair ij, s_6 is a scaling factor that depends on the functional used, R_{ij} is the interatomic distance, and $f_{\text{dmp}}(R_{ij})$ is a damping function used to avoid short–distance singularities, given by

$$f_{\text{dmp}}(R_{ij}) = \frac{1}{1 + e^{-d(R_{ij}/R_r - 1)}} \tag{A.23}$$

where R_r is the sum of atomic van der Waals radii.

Appendix B

Supplementary information / CP on Si(001)

B.1 Measurement of the rate of thermal reaction

Figure B.1 shows a comparison of rates of reaction of A both in isolation and at the two ends of a line. A schematic shows the three positions of A referred to. The measured rates of reaction are identical within experimental uncertainties for A in isolation, and for A within a line close to the end–of–line buckled dimer (the data set shown is different from that given in the main text, and was obtained at 308 K). Although the rate of reaction is distinguishably different for A within a line, far from the buckled dimer, the derived activation energies cannot be distinguished within their uncertainties, and we therefore chose to treat all three species together in our analysis.

Relative uncertainties arise between measurements of E_a and are due only to uncertainties of the slopes of the straight line fits, which give the first order rate constants. Conversion of the first order rate constants to activation energies requires that a value of pre–exponential factor be assumed. As the reactions studied are for identical molecules on the same surface in slightly different configurations it should be an excellent assumption that the pre–exponential factors for the reactions are identical. The relative uncertainties were calculated assuming a pre–exponential factor of 10^{13} and arise only from the difference in the measured first order rate constants. The relative uncertainties in the activation energies are of order 3 meV.

Absolute uncertainties in the activation energies derive from the uncertainty in the value of the pre–exponential factor to be used. A usual approximation for the pre–exponential factor and its uncertainty is 10^{11} to 10^{15}, and recent work on halogenated molecules on a silicon surface showed that this is an excellent approximation. Using this range of pre–exponential factors gives an absolute uncertainty of ± 0.13 eV which must be applied to all derived activation energies in the same sense.

B.2 Line profiles

Line profiles of A and S pairs in a line were measured along the axes shown in Figure B.2. The calculated configurations for A and S have different geometries of the alkyl tails. This difference shows up in the line profiles, where the line profile of S is symmetric about the centre point, while that of A is not.

B.3 Electron–induced reaction

For electron–induced reactions, the reaction yield as a function of positive bias voltage was measured for both A and S configurations as shown in Figure B.3. The electron–induced reaction of isolated A occurs directly. It was therefore possible to check that the threshold energy for A was identical in a line and in isolation. However, the electron–induced reaction of isolated S cannot be observed because electron impact causes it to switch to A before reaction occurs. Assuming a linear threshold law we determine the electron–induced reaction thresholds for the two stereoisomers to be $E_0(A) = 1.18 \pm 0.04$ eV and $E_0(S) = 2.2 \pm 0.3$ eV. Calculated energy spacings (DOS), shown in Figure B.3, are essentially identical for the two stereoisomers. The initial state of the transition is a silicon state, but using the DOS of the CP pair we can ascribe the energy difference of 1.0 eV between the two energy thresholds to excitation to either LUMO+1 or LUMO+2. For A, the electronic excitation that causes reaction is ascribed to initial→LUMO+1, while for S excitation is from the initial→LUMO+2. The measured difference in reaction thresholds indicates that the excitation process initial→LUMO+1 is two orders of magnitude weaker for the S configuration than for the A configuration. Accurate calculation of activation energies will require mixing of the ground state PES in the transition state region with a strongly coupled low–lying electronically excited state. In the present case the activation energy for surface chlorination by A is measured to be 1.1 eV, a value to be compared with the energy of an electronically excited state that we identify as LUMO+1, which we find also to lie at about 1.1 eV above the initial state and to be strongly coupled to that initial state. Accordingly, the energy of this LUMO+1 excited state may be low enough above the transition state for A (only 70 meV higher), and sufficiently coupled to the transition state, to account for the small stabilisation in the transition state. In the case of S the low–lying LUMO+1 state has been shown here to be poorly coupled to the initial ground electronic state. If the same applies in the transition state, this lack of stabilisation in the case of S might account for the higher activation energy for its thermal reaction. This argument makes a tentative link between the lower activation energy for thermal reaction and the lower threshold energy for electron–induced reaction.

B.4 Figures

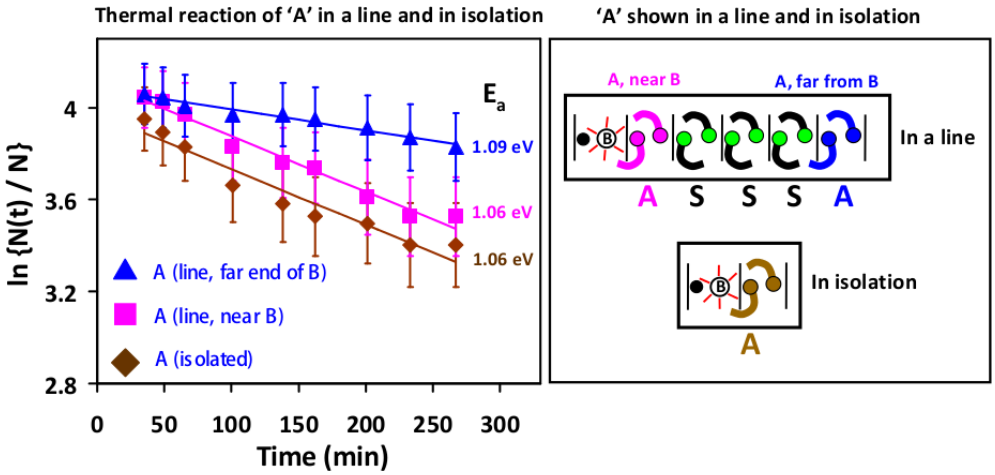

Figure B.1: Thermal reaction of A in various environments. (Left) Rates of thermal reaction obtained by plotting the natural logarithm of survival $N(t)/N$ against time, where N is a normalizing constant of magnitude 1, and the same dimensions as $N(t)$. Blue line (triangles): A pair far from the buckled dimer, B. Pink line (squares): A pair close to the buckled dimer, B. Brown line (diamonds): A pair in isolation. The error bars are derived from the standard error (1/square root of the count). (Right) Schematic: the positions of the three types of A pairs, measured at left, are indicated – the length of the line of CP pairs was not important in these measurements.

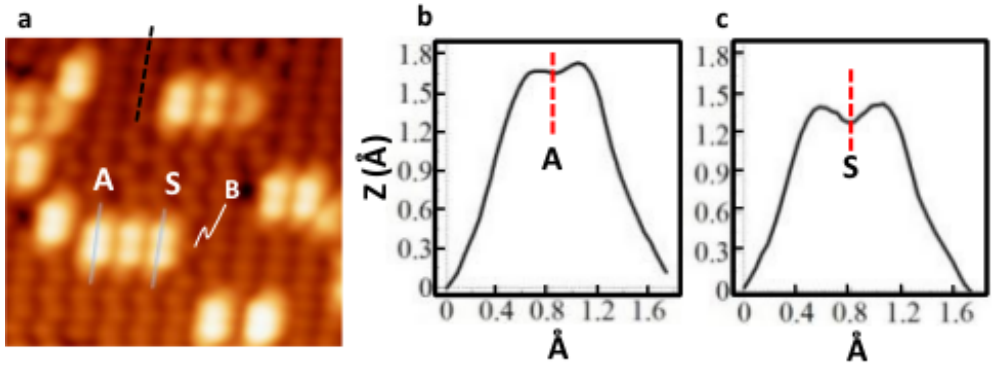

Figure B.2: Height profiles of symmetric and asymmetric CP pairs. (a) STM image ($V_surf = –1.5$ V, 0.2 nA, 75×75 Å^2) after dosing with 0.3 L chloropentane (1×10^{-9} torr, 30 s). (b),(c) Height profiles taken along feature A and feature S in the line of three CP pairs shown in (a). The asymmetric and symmetric shapes are evident in the line profile at its highest point. The A pair is asymmetric about the centre line shown in (b) as a red dashed line. The S pair is symmetric about the centre line shown in (c) as a red dashed line. The average height of the feature A and S compared to bare Si are 1.6 Å and 1.3 Å respectively at this imaging bias. 4.

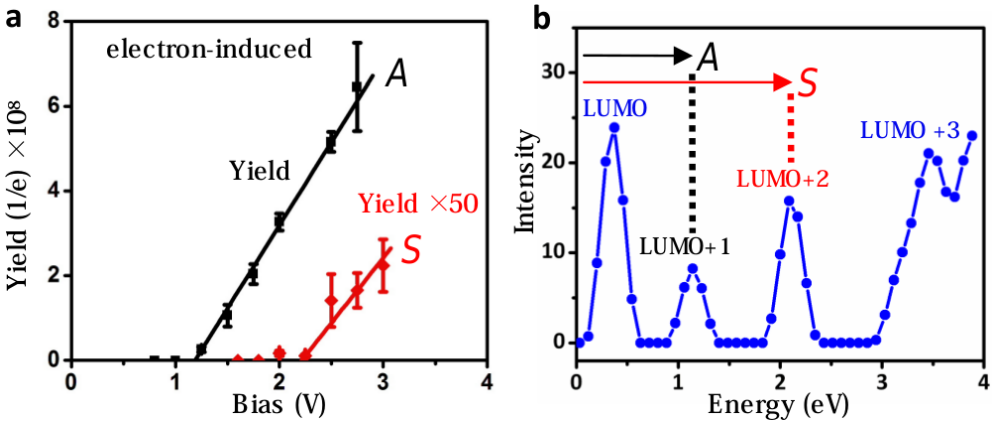

Figure B.3: Electron–induced reaction of CP pairs. (a) The electron–induced reaction threshold, E_0, assuming a linear threshold law measured for positive surface bias for the middle members of the CP line, S,($E_0 = 2.2 \pm 0.3$ eV) and for the end members of the line, A ($E_0 = 1.18 \pm 0.03$ eV). The error bars represent the standard error (square root of the count). Yields for S have been multiplied by 50. (b) Densities of states (DOS) for a CP pair.

Appendix C

Supplementary information / mDIB on Cu(110)

C.1 Structural details of the four most stable adsorption arrangements.

Fractional coordinates of the relaxed degrees of freedom are given here. Coordinates of the frozen internal layers are given separately. The lattice constant is 3.615 Å (see Section 8.3.1).

C.1.1 B5x: fractional coordinates

```
Cu 0.1666742767407406  0.1240545196718742  0.1303680673102462
Cu 0.4999591211163314  0.1245286350933267  0.1299679190253177
Cu 0.8333989825598342  0.1245145707714974  0.1308775734145020
Cu 0.1691988024558123  0.3748436155869043  0.1287490641586866
Cu 0.4997828053746464  0.3752750512833862  0.1288228962482822
Cu 0.8343939671145398  0.3744816726470756  0.1292247685447225
Cu 0.1675221663727460  0.6253511764418769  0.1289057868226105
Cu 0.5004293724041879  0.6252117086673814  0.1295277701831237
Cu 0.8352560837607488  0.6265300430482642  0.1287721769254125
Cu 0.1662124902292577  0.8748519774740123  0.1308571494149615
Cu 0.5012251717154570  0.8751011919382033  0.1304242290979016
Cu 0.8333368042303695  0.8763604254738689  0.1311273619692315
Cu 0.0003932996974450  0.0006691588241792  0.1901107389195976
Cu 0.3340511444122518  0.9966580414712730  0.1885631237618005
Cu 0.6663132839491004  0.0012282415568137  0.1900835802177305
Cu 0.0005875760815982  0.2489698182560221  0.1881272096893818
Cu 0.3339003484350266  0.2449999331618504  0.1909960110546988
Cu 0.6669401804119569  0.2496527229205972  0.1879664012580956
Cu 0.9993450098082044  0.4999167001924747  0.1891139512411964
Cu 0.3361189900673583  0.5035665812807376  0.1916652994651990
Cu 0.6711624696247473  0.5010344872572644  0.1876127813284431
Cu 0.9990509998134219  0.7521922351855654  0.1888863656947353
Cu 0.3343732255853605  0.7508172987027931  0.1885886603330241
Cu 0.6679911928648956  0.7529345047334459  0.1888180396229925
I  0.6569616174577145  0.5493178395463033  0.3160320790179482
I  0.0867293725564596  0.5189972210866345  0.3109351104237508
C  0.2710386801818786  0.2893412660050991  0.2960431912546259
```

```
C  0.3881524850829650  0.2260378354842828  0.3021990851968825
C  0.4974874489518086  0.3018743451745781  0.3124519927060526
C  0.4891334657648763  0.4384872680409738  0.3134372884783753
C  0.3749125444142872  0.5074875406438384  0.3041637607440268
C  0.2658642906078816  0.4294019934267129  0.2987582198899574
H  0.3926492065199610  0.1183612129281694  0.3062597027030370
H  0.5868447756856354  0.2518629110326340  0.3192105469066596
H  0.3695141062539189  0.6141076888176187  0.3118852207743865
H  0.1852530305539267  0.2312741957408561  0.2958959223693137
```

C.1.2 B3x: fractional coordinates

```
Cu 0.1668740763085159  0.1249370694973496  0.1303594508280981
Cu 0.4997867062254110  0.1249495456374506  0.1303634418059265
Cu 0.8333451742172373  0.1249732971040939  0.1308015602913256
Cu 0.1692073080383401  0.3754401414815129  0.1296793791805106
Cu 0.4974479493209981  0.3754571143402566  0.1297064138325437
Cu 0.8333288213736484  0.3750177061453354  0.1292477039735029
Cu 0.1665624627015367  0.6257933101014007  0.1293083980793691
Cu 0.5001192803370222  0.6257726594081807  0.1293009935347487
Cu 0.8333538277610040  0.6265051483220292  0.1290095997627385
Cu 0.1662354914217400  0.8754259686883434  0.1306205552482166
Cu 0.5004273065921505  0.8754324245572720  0.1306072297758357
Cu 0.8333583445763604  0.8767088383401276  0.1311547287523479
Cu 0.0005549901245077  0.0014269062393767  0.1900446824687890
Cu 0.3333392471289562  0.9978299079589985  0.1889302293665922
Cu 0.6661387428085986  0.0014588085520852  0.1900252725998383
Cu 0.0000941404501921  0.2498509708670714  0.1880759032911177
Cu 0.3332702020482343  0.2448171700848021  0.1919919197861393
Cu 0.6665979414203564  0.2498934516376742  0.1880669522583444
Cu 0.9977909913005367  0.5006224962634426  0.1887722504014925
Cu 0.3333140778923570  0.5064192872083374  0.1913422007966645
Cu 0.6689625521396528  0.5006564178837396  0.1888221654518015
Cu 0.9989980605400157  0.7531547186514668  0.1887382121121762
Cu 0.3333413885007724  0.7514239132159997  0.1890523509375301
Cu 0.6676963018331866  0.7532211607706099  0.1887099510252327
I  0.6183264150060616  0.5345355743578664  0.3153295357541332
I  0.0482554753804193  0.5323804334161363  0.3153710928066031
C  0.2199568809673847  0.2944820533371687  0.3100042283697595
C  0.3343911160527956  0.2251497229035848  0.3062001439418057
C  0.4483174026580347  0.2953619901949479  0.3101530512881486
C  0.4460029174892641  0.4326804745589109  0.3126592138984940
C  0.3333939358601046  0.5061315618254869  0.3085530901966670
C  0.2212742368637838  0.4318586208363456  0.3125645122906168
H  0.3347589943823480  0.1173870800702576  0.3102155410443103
H  0.5363018618907579  0.2411280876992928  0.3106152004976365
H  0.3330348384709932  0.6130468872816138  0.3154404185285573
H  0.1323579635040913  0.2395568343518113  0.3104189871284879
```

C.1.3 A5y: fractional coordinates

```
Cu 0.1658276922466043  0.1249205078437849  0.1308237659912731
Cu 0.4997495257158669  0.1255120603767717  0.1281246614226351
Cu 0.8339610551179694  0.1244001455049432  0.1295472162872894
Cu 0.1655450622416852  0.3750994781036046  0.1288806133537166
```

```
Cu 0.4996363134726092  0.3748478048442351  0.1274612075192504
Cu 0.8359789315991162  0.3748910141443471  0.1302626580732818
Cu 0.1657293863941056  0.6254515914076222  0.1308278461745692
Cu 0.4998880399545105  0.6242686918663860  0.1281107554957710
Cu 0.8338005081859337  0.6255050460151813  0.1296854934785755
Cu 0.1651162581289115  0.8749777982193535  0.1313826647733404
Cu 0.5011692781373228  0.8749714879395076  0.1288829973082465
Cu 0.8311272820220775  0.8748641981150227  0.1318622442965140
Cu 0.9989665431268137  0.0001957958407194  0.1897787086688192
Cu 0.3334717656448293  0.9993618636816866  0.1880513526619750
Cu 0.6663584770812816  0.0007388021619960  0.1914436259417094
Cu 0.0000012946528378  0.2498642557938673  0.1896367998097509
Cu 0.3326940981643515  0.2496974645904220  0.1896571334897514
Cu 0.6684937980497432  0.2521468000587145  0.1868487190492784
Cu 0.9999436114489322  0.5001700242426533  0.1895927840405667
Cu 0.3325819172954359  0.5005703174988928  0.1895841044632591
Cu 0.6683590411258726  0.4974968750785942  0.1868113378526627
Cu 0.9988443025898869  0.7498796994689699  0.1898392563717519
Cu 0.3335506191020239  0.7509037062700957  0.1879116717631552
Cu 0.6664814638569013  0.7491702153977663  0.1916922667828428
I  0.5868442676132142  0.0723490571487213  0.3119240624438745
I  0.5840861488736276  0.6852116066277937  0.3120200215194837
C  0.3573083930655178  0.4998164412473309  0.2990828533855586
C  0.2924258592340533  0.3774920485582894  0.2930773298031835
C  0.3581439767981903  0.2555743671445979  0.2991310402697596
C  0.4876294936006173  0.2596835965697499  0.3104772741697305
C  0.5543024427325236  0.3785194709006715  0.3150423996647937
C  0.4868385209179725  0.4968323870024572  0.3105333383906094
H  0.1904958077263322  0.3770837658844753  0.2912891242587921
H  0.3061166968048294  0.1633439870873346  0.3052090325841467
H  0.6545703348205809  0.3788893651358131  0.3242797685159465
H  0.3046589692077748  0.5917021087457612  0.3049802171862765
```

C.1.4 A5x*: fractional coordinates

```
Cu 0.1668913409674013  0.1247922470849405  0.1305108532582047
Cu 0.5009117547171811  0.1238154841763242  0.1299686825401993
Cu 0.8336260915584461  0.1243407387956974  0.1312629289704994
Cu 0.1683750459040728  0.3743476245822904  0.1265221652112501
Cu 0.4991548154182196  0.3746067714333327  0.1285685297273476
Cu 0.8345844026382778  0.3730759976098021  0.1302728775763501
Cu 0.1655486452008853  0.6259209741677682  0.1294117404717256
Cu 0.4999838009181843  0.6239313512984331  0.1284251795763827
Cu 0.8336909522359842  0.6249493827663891  0.1301108822870922
Cu 0.1657395917972851  0.8754809064211936  0.1303181520079218
Cu 0.5007881996492346  0.8742696860204815  0.1301464156395400
Cu 0.8315732629599839  0.8739350498329482  0.1317333234246834
Cu 0.0000465216659709  0.9992749574271397  0.1893780044894296
Cu 0.3335623909008599  0.9988196806692790  0.1885998657847916
Cu 0.6659710389076428  0.9985547163238281  0.1905097053280682
Cu 0.0018555231494391  0.2480751322458414  0.1899634949373692
Cu 0.3350162055968340  0.2470902357874992  0.1903303148693494
Cu 0.6661383404916534  0.2484227443800167  0.1891022401097467
Cu 0.0000982042221323  0.5021358579222169  0.1888581789030708
Cu 0.3311871987543606  0.5035608202564708  0.1893955983407192
```

```
Cu 0.6689938275573539  0.4956293720653988  0.1871522091073327
Cu 0.0000347857250116  0.7509447227448927  0.1894126116901989
Cu 0.3312894625665400  0.7515796699401737  0.1879211464974170
Cu 0.6665398158797006  0.7472619011550246  0.1918155987590626
I  0.0637718471626630  0.3884195961305361  0.3028326541706851
I  0.5600937870949632  0.6903767343180714  0.3126671940035673
C  0.5241355530254762  0.3876566345694974  0.3155641155425168
C  0.4585414422040168  0.2679288881747809  0.3106725367310350
C  0.3275631045914262  0.2667265458869610  0.3025329783894690
C  0.2645846256295767  0.3893479330163236  0.2992206616275125
C  0.3288686529648319  0.5120302547719676  0.3001221964420390
C  0.4594862687545222  0.5071305454303214  0.3109967528300029
H  0.5084116868266721  0.1739838631779104  0.3140517363206331
H  0.2752566921294327  0.1745853950116526  0.3078195155786359
H  0.2775284063230082  0.6049080424175560  0.3046942039158869
H  0.6247801013902331  0.3866675861375238  0.3234146811347766
```

C.1.5 Bottom (frozen) Cu layers: fractional coordinates

```
Cu 0.1666666666666643  0.1250000000000000  0.0000000000000000
Cu 0.5000000000000000  0.1250000000000000  0.0000000000000000
Cu 0.8333333333333357  0.1250000000000000  0.0000000000000000
Cu 0.1666666666666643  0.3750000000000000  0.0000000000000000
Cu 0.5000000000000000  0.3750000000000000  0.0000000000000000
Cu 0.8333333333333357  0.3750000000000000  0.0000000000000000
Cu 0.1666666666666643  0.6250000000000000  0.0000000000000000
Cu 0.5000000000000000  0.6250000000000000  0.0000000000000000
Cu 0.8333333333333357  0.6250000000000000  0.0000000000000000
Cu 0.1666666666666643  0.8750000000000000  0.0000000000000000
Cu 0.5000000000000000  0.8750000000000000  0.0000000000000000
Cu 0.8333333333333357  0.8750000000000000  0.0000000000000000
Cu 0.0000000000000000  0.0000000000000000  0.0632153462380813
Cu 0.3333333333333357  0.0000000000000000  0.0632153462380813
Cu 0.6666666666666643  0.0000000000000000  0.0632153462380813
Cu 0.0000000000000000  0.2500000000000000  0.0632153462380813
Cu 0.3333333333333357  0.2500000000000000  0.0632153462380813
Cu 0.6666666666666643  0.2500000000000000  0.0632153462380813
Cu 0.0000000000000000  0.5000000000000000  0.0632153462380813
Cu 0.3333333333333357  0.5000000000000000  0.0632153462380813
Cu 0.6666666666666643  0.5000000000000000  0.0632153462380813
Cu 0.0000000000000000  0.7500000000000000  0.0632153462380813
Cu 0.3333333333333357  0.7500000000000000  0.0632153462380813
Cu 0.6666666666666643  0.7500000000000000  0.0632153462380813
```

C.2 Density of states of the four most stable adsorption arrangements.

Computed Density of States of the four most stable arrangements compared to that of the clean surface and the isolated m–DIB in vacuum, summed, are given here. Results for the most stable configuration is also given in the main document. Comparison between the interacting and non interacting system unveils that no significant variation in the electronic structure occurs upon adsorption; hence, chemisorption is unlikely.

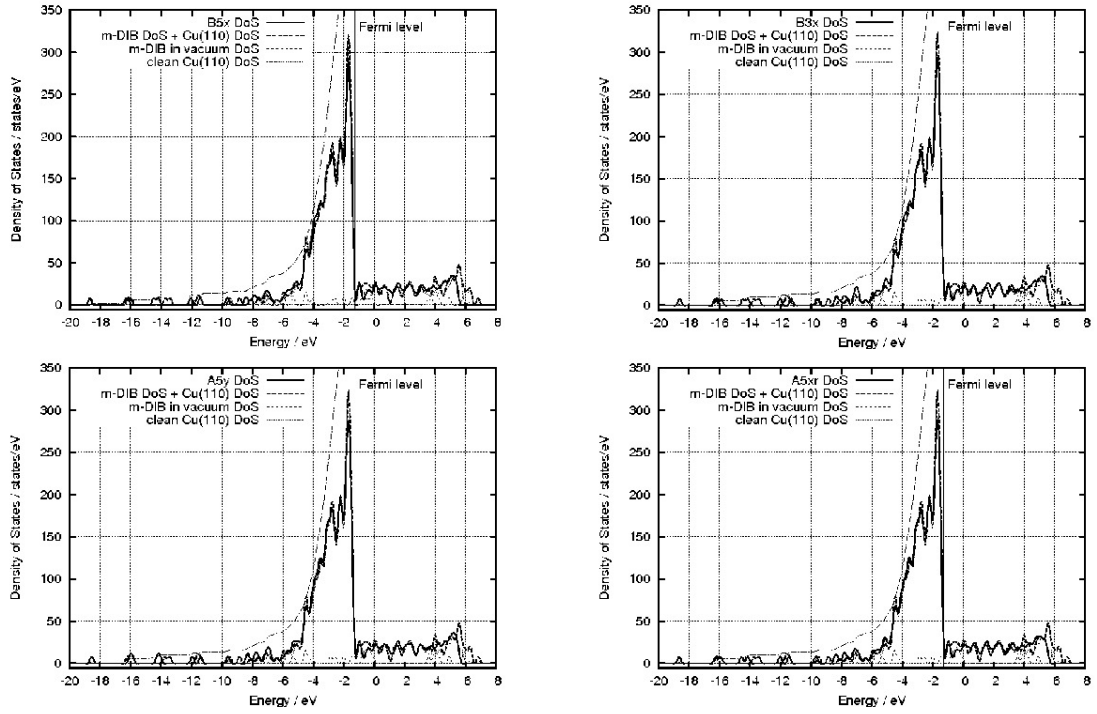

Figure C.1: Density of States of the four most stable arrangements and their integrals, compared to that of the clean surface and the isolated m–DIB in vacuum, summed. Comparison between the interacting and non interacting system shows that no significant variation in the electronic structure occurs upon adsorption; hence, chemisorption is unlikely.

C.3 Partial charge analysis of the four most stable arrangements.

Partial charges computed with Bader's method for the four most stable arrangements are given below. Results for the most stable configuration is also given in the main document. Little or no significant charge transfer occurs between the surface and the adsorbate, but all of the charge rearrangement is internal to the molecule; hence, we shall definitely conclude that m–DIB on Cu(110) is physisorbed.

Atom(s)	Charge $/e^-$ (interacting)	Charge $/e^-$ (non interacting)	Difference
I1†	6.78	6.10	–0.68
I2‡	6.01	6.07	+0.06
C1†	4.46	5.24	+0.78
C2	3.97	3.84	–0.13
C3‡	5.14	5.01	–0.13
C4	3.99	4.12	+0.13
C5	4.02	3.87	–0.15
C6	4.10	4.00	–0.10
Cu I layer (avg)	11.00	10.99	–0.01
Cu II layer (avg)	11.03	10.98	–0.05
Cu internal layers (avg)	11.01	11.03	+0.02
Adsorbate (total)	38.47	38.25	–0.22
Surface (total)	528.56	528.22	–0.34
B3x: Atom(s)	Charge $/e^-$ (interacting)	Charge $/e^-$ (non interacting)	Difference
I1†	6.02	6.10	+0.08
I2‡	6.00	6.07	+0.07
C1†	3.84	5.24	+1.40
C2	4.17	3.84	–0.33
C3‡	3.85	5.01	+1.16
C4	5.27	4.12	–1.15
C5	3.97	3.87	–0.10
C6	5.27	4.00	–1.27
Cu I layer (avg)	10.99	10.99	0.00.
Cu II layer (avg)	11.02	10.98	–0.04
Cu internal layers (avg)	11.00	11.03	+0.03
Adsorbate (total)	38.39	38.25	–0.14
Surface (total)	528.16	528.22	+0.04

Table C.1: Partial charge analysis for B5x and B3x. Bonded atoms are marked with † and ‡. Partial charges for the interacting and non–interacting system are reported in columns 1 and 2 respectively. The charge rearrangement is entirely internal to the molecule; small deviations are ascribable to small errors intrinsic in the method, a good estimate of which is given by the electron count (last two rows). Since there is no charge transfer between the adsorbate and the surface, we can conclusively rule out the possibility of chemisorption.

A5y: Atom(s)	Charge $/e^-$ (interacting)	Charge $/e^-$ (non interacting)	Difference
I1†	6.87	6.10	–0.77
I2‡	6.87	6.07	–0.80
C1†	4.29	5.24	+0.95
C2	3.91	3.84	–0.07
C3‡	4.31	5.01	+0.70
C4	4.16	4.12	–0.04
C5	4.16	3.87	–0.29
C6	4.11	4.00	–0.11
Cu I layer (avg)	11.00	10.99	–0.01
Cu II layer (avg)	11.02	10.98	–0.04
Cu internal layers (avg)	11.00	11.03	+0.03
Adsorbate (total)	38.68	38.25	–0.43
Surface (total)	528.17	528.22	+0.05
A5x*: Atom(s)	Charge $/e^-$ (interacting)	Charge $/e^-$ (non interacting)	Difference
I1†	6.78	6.10	–0.68
I2‡	6.80	6.07	–0.73
C1†	4.37	5.24	+0.87
C2	4.11	3.84	–0.27
C3‡	4.49	5.01	+0.52
C4	4.04	4.12	+0.08
C5	4.14	3.87	–0.27
C6	3.87	4.00	+0.13
Cu I layer (avg)	11.00	10.99	–0.01
Cu II layer (avg)	11.03	10.98	–0.05
Cu internal layers (avg)	11.01	11.03	+0.02
Adsorbate (total)	38.59	38.25	–0.34
Surface (total)	528.69	528.22	–0.47

Table C.2: Partial charge analysis for A5y and A5x*. Bonded atoms are marked with † and ‡. Partial charges for the interacting and non–interacting system are reported in columns 1 and 2 respectively. The charge rearrangement is entirely internal to the molecule; small deviations are ascribable to small errors intrinsic in the method, a good estimate of which is given by the electron count (last two rows). Since there is no charge transfer between the adsorbate and the surface, we can conclusively rule out the possibility of chemisorption.

C.4 STM images

Computed STM images at bias voltages ranging from –1.0 V to +1.0 V with intervals of 0.2 V for the B3x configuration.

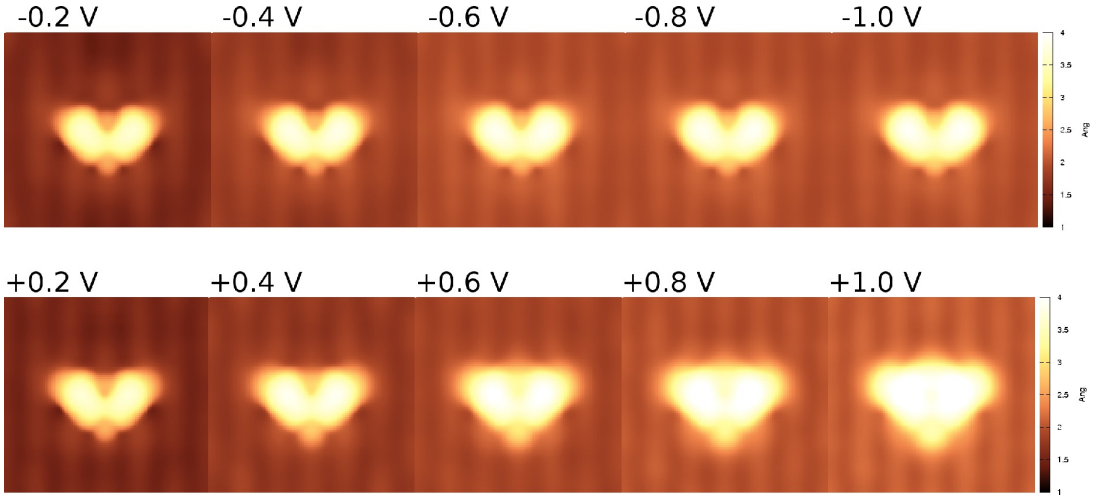

Figure C.2: Simulated STM images of B3x at bias voltages ranging from –1.0 V to +1.0 V and plotted as isocurrent surfaces at 0.001 pA. The best results in terms of contrast and clarity were obtained at –0.2 V.

Appendix D

Supplementary information / Supported Cu clusters

D.1 Preliminary calculations

We performed preliminary studies in order to identify the best candidate structures We compared structures generated as shown in Figure D.1 (top view). We considered Cu_3 and Cu_5 clusters anchored by single Cl, I and S atoms chemisorbed in the 4–fold hollow position and in the long bridge position. The latter structures are different from that investigated in Chapter 10, but their only purpose is to evaluate the effect of the chemical nature of the dopant and explore a very small subspace of the possible trial configurations. Moreover, the supercell size employed in the preliminary investigation was chosen as 3×4, which is much smaller than the one employed in Chapter 10.
The definitive structures actually employed in Chapter 10 were then chosen based upon chemical intuition and optimized. It has to be noted that there is no certainty that the chosen structures constitute the best set. In order to determine that, a more complex theoretical setup must be employed, such as Genetic Algorithms. However, we can assume that, for every size n, the stability does not change dramatically with the structure, that is, the weight of the cooperative effect of the binding between the anchor and the Cu atoms is larger than the individual differences between clusters of the same size. Moreover, for the purpose of the present Thesis, we are merely interested in proposing the existence and stability of such structures, and a more thorough characterization could be seen as a perspective future work.
The preliminary calculations show that the choice of sulphur as an anchor is preferable over both chlorine and iodine. Figure D.2 shows the converged trial structures for a Cu_5 cluster anchored by a single Cl, I or S adatom centred in the four–fold hollow position (bottom right trial structure in Figure D.1). The corresponding normalized formation energies are –0.298, 0.044 and –0.881 eV respectively. The S–centred structures are energetically favoured. Analogous results were obtained for all other trial structures (not shown here). Furthermore, the I–centred structure is also unfavourable due to

the large geometric distortion caused by the big central atom, to the extent that the presence of the anchor does not stabilize the structure at all, as the formation energy is positive.

D.2 Figures

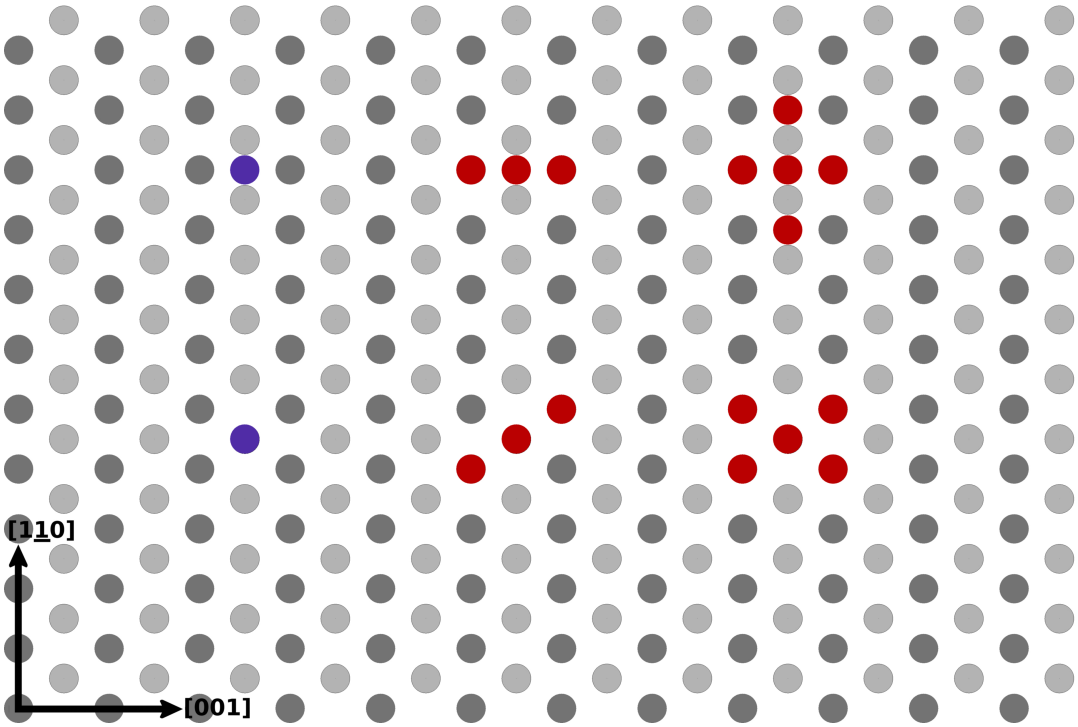

Figure D.1: Diagram showing the preliminary structures used to determine the best candidate structures for Cu aggregates on Cu(110) supported by a single Cl, I or S atom. Dark grey circles represent uppermost Cu atoms; light grey circles represent the second layer. Violet circles represent adatoms adsorbed in the long bridge position (top) and in the 4–fold hollow position (bottom). Red circles represent the Cu atoms forming some of the tentative cluster structures.

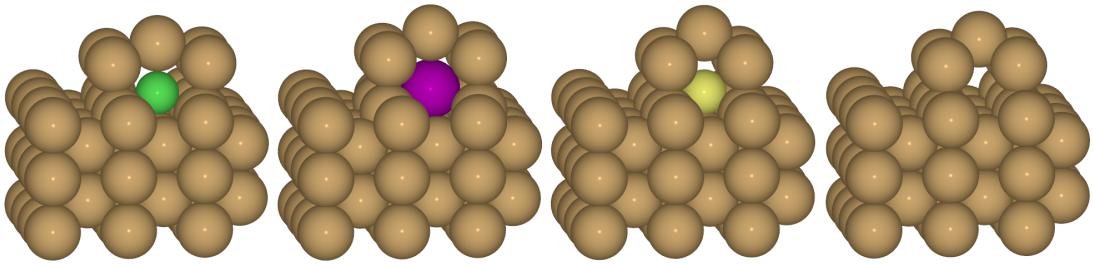

Figure D.2: Converged XCu_5/Cu(110) trial structures with X = Cl, I, S centred in the four–fold hollow position of the surface. The corresponding normalized formation energies are –0.298, 0.044 and –0.881 eV respectively.

List of Figures

List of Tables

Acknowledgements

I wish to thank Werner for being the perfect supervisor, a mentor rather than a boss, giving me support rather than pressure, truly treating me as a peer. Thank you for everything you gave me inside and outside the walls of SSRC, for the scientific and political chitchats, for the beers and the wine and the super expensive chinese liquors, Thank you Prof. Polanyi, Iain, Hari, Amir, Lydie and all the folks in Toronto for the opportunity to work with you, which was invaluable experience. I learned a lot, I almost got arrested, I saw a raccoon for the first time in my life. Had fun. Thank you my group, Haiping and Alejandro, Felix and Torsten, and above all Piotr, for sharing more of a life experience than just the time of a PhD.
Thanks to Nata, Adolfo, Jonas, Maija, Geoff, John, Fiona, Ivan, Scott, Josh and all the zoo folks, for all the barbecues, the mulled wine parties, the free cakes, the pub golfs. Thank you "seniors" Felix, Matthew, Gibo, for, well, helping me a hell of a lot. To your honour I shall raise my coffee mug to the heavens every time I'll win over a compiler's complaint. Thank you Italian gang, Sergio, Emiliano, Tommaso, Luigi, Ilaria, Enzo, I'll miss you all during my coffee breaks to come.

Thank you Liverpool for being so unconventionally beautiful. Thank you for having been more than a home, for the hidden treasures, for the waterfront freezing wind blasts the true Romantics shall appreciate, thank you for the occasional snow and the occasional sunshine, thank you for Matta's, for the MelloMello, for the signless Kazimier and the gigs like "Oh this must be the place, there's the band outside smoking", for Bold Street Coffee's mocha, thank you for the penguins and the lambananas and the now gone Banksy's cat–rat whose sight no one will enjoy from the window anymore. (Do you feel lonely? No.)
Thank you Claudio, Marco, Marco, Valentina, Mario, Filomena, Francesca, Angela, Megh, Mark, Obi and all the Derby and Rathbone fellas, for the endless Risk nights, the Rings of Fire, the snow fights, the freak shows (Oooouh you fell oooouva!), the bent teaspoons and the magic tricks, the sicilian sausages, the pizza, the pizza pollo, the pizza with or without pineapples on top, for the frozen pipes and that entire week without seeing the sun, for Bambola, for John Holmes the bike guy, for the dart games, for

climbing trees, for Simon's cat, for sharing cabs, for sharing flats, for sharing everything we shared, that is way more than I could ever squeeze into these words.
Thank you my web fellas, Spinoza and iFighi, it was a pleasure to have you online while waiting for VASP to converge. Specials: thank you Lele for being there when I got this job, thank you for MM and the gravitational capsule that kept me laughing through the first months. Thank you and Lia for making your home my home. Thank you Gas for the maneki neko, for the night chats, and for finally believing in the uncertainty principle. Thank you Tati for the gigs, the laughs, and your granma's olives. Thank you Riccardo for the Beatles tour and for confirming at least half of my five–year predictions.
Thank you chemists (and non–chemists) in Rome, for keeping up what we started –well, at least for a while, for the parties, for the graduations I have missed, for not forgetting me. Thank you Ivan, Ele, Brizio, for visiting, thank you Domenico for wandering across Europe in parallel with me (see you in Germany), for the deserted Coventry and the rainy Birmingham, thank you Francesco for reappearing after all, thank you Alessandro/Ignazio for being so nerd, thank yo Arianna and Davide for the last epic debate on googlegroups, thank you Giorgio for keeping in touch, for all the gossip, for the sgroppini in Marzamemi, and for Watchmen (I'll return it, promise). Thank you Anthony and Chiara for all the wine, thank you Via Anacapri flatmates for having me around all the time.
Thank you Federica, Mara, Nicol for being friends for a lifetime, because I'll never feel completely uprooted as long as you gals stick around.
Thanks to my parents, for driving all the way up to the Pool with 10 litres of proper olive oil, to make this place a little bit more like home, for believing in me, for being proud of me. Thank you Zia Nennella for overcoming the fear of flying to come see where the Beatles were born. Thank you Dadda for the Primark hauls, for helping me putting my whole life in boxes –again– while six months pregnant. Thank you Franz for letting me have someone to go to gigs to for a while. And, above all, thank you both for Nino.
Thank you Flavio for not hating me after what I've put you through.
And thank you Gianluca, for waiting a decade for me to come find you, for killing my teardrop, for letting me kill yours, for floating in space, and drifting in time. Thank you a hundred times for the hundred reasons you know better, for the sleepless nights, the good kind, the bad kind, and the Ryanair–flight–at–6am kind, for the unconditional surrender to the power of felinity, thank you for playing Leave Me Alone –twice– or was that me?
Thank you for being so patient, though you must admit that the wonderful view there is from here, at the right pole, was all worth it.